UNIVERSITÀ
DEGLI STUDI
DI MILANO

Dipartimento di Matematica Federigo Enriques

Scuola di Dottorato in Scienze Matematiche

Dottorato di Ricerca in Matematica e Statisctica per le Scienze

Computazionali – Ciclo XXVI

Isogeometric Overlapping Additive Schwarz Preconditioners in Computational Electrocardiology

Ph.D. Thesis

MAT/08

Advisor
Prof. Luca Franco Pavarino

Coordinator
Prof. Giovanni Naldi

Candidate
Lara Antonella Charawi

Academic Year 2012/2013

Contents

Introduction

The electrical activity of the heart is a complex phenomenon closely related to its physiology, fiber structure and anatomy. Its modelling must deals with micro and macroscales at the same time. Typically, phenomenological evidence refers to the macroscales, while their physical causes are found at the microscales. Accordingly, accurate cardiac models should include processes acting on different levels of biological organisation: cell, tissue and organ.

At the cellular level the cell membrane separates both the intra- and extra-cellular environments consisting of a dilute aqueous solution of dissolved salts dissociated into ions. Differences in ion concentrations on opposite sides of the membrane lead to a voltage called the *transmembrane potential*, v_M, defined as the difference between the intra- and extracellular potentials, (u_i and u_e). The bioelectric activity of a cardiac cell is described by the time course of v_M, the so called *action potential*. Starting from the sino-atrial node (SAN), which acts as a pacemaker, a front-like variation of v_m spread first in the atria and then to the ventricles; the fiber structure strongly affects this process and is the main factor of the anisotropic conductivity of cardiac tissue.

The whole process of action potential generation is due to specialized membrane-spanning proteins that control the movement of ions by passive electrodiffusion through transmembrane pores (*ion channels*). Membrane ion channels interact with dynamically changing ionic concentrations and varying transmembrane potential, and are subject to various regulatory processes. These interactions are nonlinear making the single cardiac cell a complex interactive system. Even though advances in electrophysiological techniques and molecular biology have allowed us to build models based on ion channels molecular structure, most of the mathematical models of the ionic currents are based on extensions of the formalism introduced by Hodgkin-Huxley, [37]. Using their formalism, a SAN AP model was thus developed based on available experimental data [69], with the aim to gain a deeper understanding of the cellular basis of cardiac pacemaking, which is

still debated. Recently, novel models incorporating a detailed calcium-handling dynamics have been proposed, but they fail to reproduce experimental effects of the *funny current* (I_f) reduction. Our model describes satisfactorily experimental data concerning autonomic stimulation, funny-channel blockade and inhibition of the Ca^{2+} -related system by specific drugs. Simulation results suggest that a detailed description of the intracellular calcium fluxes is fully compatible with the observation that I_f is a major component of pacemaking and rate modulation.

At the tissue level the most complete mathematical model of cardiac electrophysiology is the Bidomain model, consisting of a degenerate reaction-diffusion system of a parabolic and an elliptic partial differential equation modelling the intra- and extracellular electric potentials of the anisotropic cardiac tissue, coupled nonlinearly with a membrane model. A reduced cardiac tissue model is the anisotropic Monodomainn system, a parabolic reaction-diffusion equation describing the evolution of the transmembrane potential coupled with an elliptic problem for the extracellular potential.

The multiscale nature of both the Bidomain and Monodomain models yields very high computational costs for their numerical resolution. The starting point for a spatial discretization is a geometrical representation that encompasses the required anatomical and structural details, and that is also suitable for computational studies. Detailed models have been proposed based on structured grids with cubic Hermite interpolation functions, which enable a smooth representation of ventricular geometry with relatively few elements. In this study we used an alternative approach that overlays the former one using Isogeometric Ananlysis (IGA). This is a method for the discretization of partial differential equations, introduced in [39], and based on the same spline or Non-Uniform Rational B-spline (NURBS) basis functions used to design domain geometries in Computer Aided Design (CAD) to construct both trial and test spaces in the discrete variational formulation of differential problem, and provides a higher control on the regularity of the discrete space. The IGA discretization of the Bidomain model in space with semi-implicit (IMEX) finite differences in time requires the solution at each time step of a large very ill-conditioned linear system. Since the iteration matrix is symmetric positive definite for the Monodomain and semi-definite for the Bidomain, it is natural to solve them using the preconditioned conjugate gradient method.

In this thesis we develop and analyze an overlapping additive Schwarz preconditioner for the isogeometric discretization of the cardiac Bidomain model, first introduced in [9] for scalar elliptic problems and in [60] for Bidomain FEM discretization. We proved that the resulting solver is scalable and optimal in the ratio

of subdomain/element size. Several tests confirm the scalability and the optimality on both a cartesian slab and on NURBS domains in two and three dimensions.

The content of the thesis is organized as follows.

In Chapter 1, we introduce some basic notions of cardiac anatomy and electrophysiology.

In Chapter 2, we describe the modelling of a cardiac cellular electrical activity and introduce a sinoatrial node cell action potential model, developed in collaboration with Prof. Stefano Severi (Università di Bologna) and Prof. Dario DiFrancesco (Università degli studi di Milano).

In Chapter 3, we present the mathematical models of the electrical activity in the cardiac tissue, i.e., the Bidomain and the Monodomain models.

In Chapter 4, there is a brief introduction to the Isogeometric Analysis.

In Chapter 5, we describe numerical method to solve the models.

In Chapter 6, we construct and analyze a two level overlapping Schwarz preconditioner for the Bidomain system.

Finally in Chapter 7, we provide results from some numerical simulations based on the Bidomain and Monodomain models.

Chapter 1

Anatomy and cellular physiology of the heart

The derivation of mathematical models of the bioelectric activity in the heart is based on the organ's anatomy and principles of physiology. This chapter aims at providing some basic background on these topics. For further information, textbooks such as [11] could be profitably consulted.

1.1 Anatomy of the heart

The human heart is a hollow muscular organ of a approximately conical form; it is located between the lungs in the mediastinum, which is the central sub-division of the thoracic cavity. It is enclosed in a thin double-walled sac of about 20 μm called the pericardium.

The pericardium's outer wall is called the parietal pericardium and the inner one the visceral pericardium. Between them there is some pericardial fluid which permits the inner and outer walls to slide easily over one another with the heart movements. Outside the parietal pericardium is a fibrous layer called the fibrous pericardium which is attached to the mediastinal fascia. This sac protects the heart, anchors it to the surrounding structures, but has no effect on ventricular hemodynamics in a healthy person.

The heart is subdivided by *septa* into right and left halves, and a constriction subdivides each half of the organ into two cavities, the upper cavity being called the atrium, the lower the ventricle. The heart therefore consists of four chambers, i.e., the right and left atria, and the right and left ventricles. The atria are the

receiving chambers and the ventricles are the discharging chambers. During each cardiac cycle, the atria contract first, forcing blood that has entered them into their respective ventricles, then the ventricles contract, forcing blood out of the heart. Due to the force needed to pump blood to the body, ventricles have thicker walls than do atria.

The proper flow of blood through the heart is guaranteed by the valves. The valves are flap-like structures composed of endocardium, Section 1.2, and connective tissue, that allow blood to flow in only one direction. A heart has four valves subdivided in two kind: the atrioventricular, allowing blood to flow from atria to ventricles, and the semilunar valves, allowing blood to flow out of the heart. The heart valves open and close passively because of pressure differences across the valve.

The pathway of the blood consists of a pulmonary circuit and a systemic circuit which function simultaneously (see Fig. 1.1). Deoxygenated blood from the body flows via the venae cavae into the right atrium, which pumps it through the tricuspid valve into the right ventricle, whose subsequent contraction forces it out through the semilunar pulmonary valve into the pulmonary arteries leading to the lungs. Meanwhile, oxygenated blood returns from the lungs through the pulmonary veins into the left atrium, which pumps it through the bicuspid (or mitral) valve into the left ventricle, whose subsequent strong contraction forces it out through the semilunar aortic valve to the aorta leading to the systemic circulation.

The audible sounds that can be heard from the heart are results from the closing of the heart valves. These sounds are referred to as the "lub-dub" sounds. The "lub" sound, or first heart tone, is made by the systole (i.e. contraction) of the ventricles and the closing of the atrioventricular valves. The "dupp" sound, or second heart tone, is made by the semilunar valves closing at the beginning of the ventricular diastole (i.e. relax).

1.2   Cardiac tissue

The outer wall of the human heart is composed of three layers hystologically different: epicardium, myocardium and endocardium.

The outer layer is called the epicardium, or visceral pericardium since it is also the inner wall of the pericardium. It is composed of connective tissue that contains adipose tissue, nerves and the coronary arteries and veins.

The inner layer is called the endocardium and is in contact with the blood that the heart pumps. It helps blood flow smoothly and prevents clots from forming.
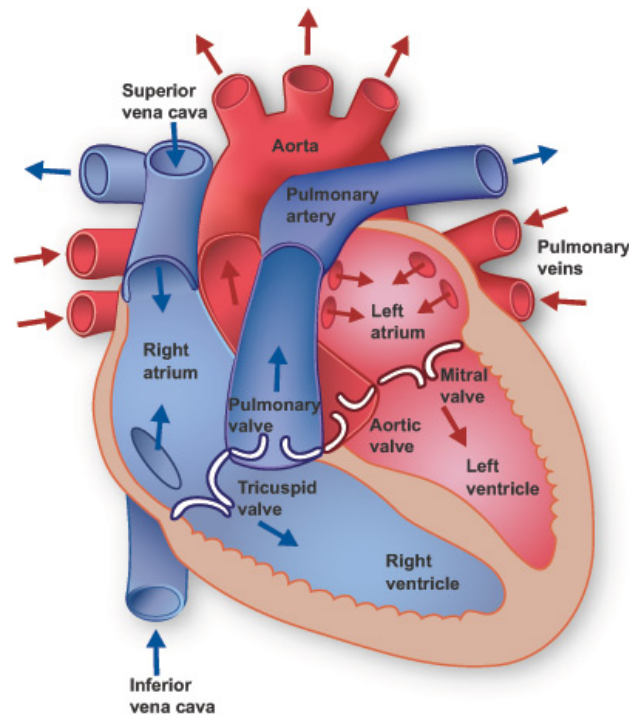
Figure 1.1: Frontal view of the opened human heart. Arrows indicate normal blood flow direction. From http://www.texasheartinstitute.org/

Outermost it is composed of connective tissue containing nerves vein and Purkinje fibers, then it merges with the inner lining (endothelium) of blood vessels.

The middle layer is called the myocardium and is composed of cardiac muscle which contracts. The cells that compose the cardiac muscle are called cardiomyocytes. They are one-nucleus cells, typically 30-100 μm long and 8-20 μm wide, with irregular staircase shape, arranged into fibrous bundles so that the longer axes of the cells are parallel. The cells are immersed in an aqueous interstitial fluid, that constitutes the extracellular space. The bounding membranes of adjacent cells are separated by narrow clefts of interstitial space, except at the point called the gap junctions or nexus, where the two membranes join. The nexus connects the intracellular compartments of the cells via connexon protein channels and nexa occur predominantly at the ends of cells and to a lesser extent along the length of cells. Approximately 70% of the gap junctions embedded in the cell membrane are at the intercalated disks in the longitudinal direction, the remaining 30% form the transverse connections.

The myocyte shape, cellular connections, and supporting structures give car-

diac tissue the appearance of being composed of fibers, se Fig. 1.2. It is possible to define an average myocyte direction at each point. This average direction can be interpreted as the local fiber orientation. The work of pioneering anatomists showed that the heart ventricle is an assembly of discrete muscle layers, arranged in nested layers or discrete fiber bundles. The first quantitative analysis of fiber orientation by Streeter and Bassett [77, 76] revealed that there is a smooth transmural variation in fiber angle and that the myocardium is well connected or syncytial throughout. In a more recent quantitative analysis, Le Grice et al. [47] shows that a true syncytial myocardium is not an accurate characterization. Rather, the heart is composed of discrete layers of fibers called sheets, see Fig. 1.3. Sheets are approximately four to five cells thick, with neighboring layers of sheets branching into each other. The sheets are surrounded by collagenous connective tissue and the arrangement varies as a function of position in the ventricle. Le Grice et al. found that the sheets lie radial to the ventricular surfaces, though they become almost tangential to the epicardial surface. In this discrete view, the edges formed by cutting the wall tangential to the epicardium define the fiber orientation. Across the ventricular wall, the fibers rotate 120° and the axis of preferred current flow is subject to a corresponding variation, see Section 1.4 and Chapter 3.

Figure 1.2: Cardiac muscle in longitudinal section.
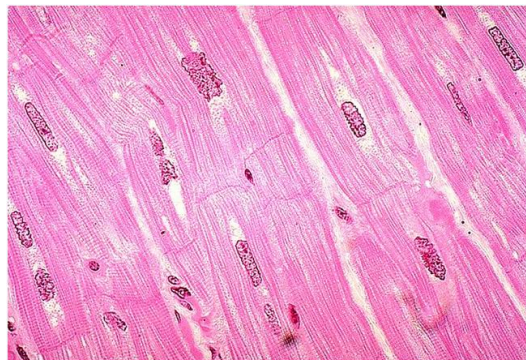
1.3   The conduction system

The heart is a pump that creates pressure that drives the flow of blood throughout the system. The pumping function of the heart is the result of a rhythmic cycle of contraction and relaxation of billions of muscle cells, a process that is controlled by a complex pattern of electrical activation. Electrical activity is essential for the

function of the heart, and many heart problems are closely linked to disturbance of it.

Although the heart is innervated by the autonomic nervous system, the heart does not require the nervous system to function. It is autorhythmic, meaning it generates its own rhythmic action potentials independent of the nervous system.

The cardiac conduction system is responsible for the organized transmission of electrical impulses in the heart. This system consists of a network of cells that transmits electrical potentials from the atria to the ventricles.

The sinoatrial node, which is located in the right atrium, is responsible for the generation of electrical impulses. These impulses are then transmitted through atrial conduction tissue to the atrioventricular node. The atrioventricular node causes a slight delay in transmission, and then allows the signals to travel to the cells of the interventricular septum. The conduction fibers in the interventricular septum are known as the *bundle of His* named after the Swiss cardiologist Wilhelm His, Jr., who discovered them in 1893. These fibers divide into the left and right bundle branches, which transmit electrical impulses to the left and right ventricles, respectively.

The ability of the conduction system to stimulate the heart to contract in an organized fashion stems from its intrinsic properties. The conductive tissue that has the fastest automaticity acts as the pacemaker of the heart. In a normal heart, the sinoatrial node has the highest automaticity and, thus, acts as the primary pacemaker of the heart. However, if one pacemaker in the heart fails to act, the conduction tissue with the next fastest rate will gain control of the pacing function. Each component of the conductive system has its own intrinsic rate of self-excitation, as follows: the sinoatrial node has an intrinsic rate of 60-100 beats per minute. The atrioventricular node has an intrinsic rate of 40-60 beats per minute. The ventricular conduction tracts have an intrinsic rate of 15-40 beats per minute.

The intracellular spaces of adjacent myocytes are interconnected by gap junctions. The gap junction distribution over the cell is heterogeneous with a higher density at the intercalated discs located at cell ends (along the long axis of the cell) and a lower density along the lateral boundaries. As a consequence of the elongated cellular geometry and the directionally varying gap junction density, current flows more readily along the cells than transverse to them. The extracellular matrix consists of networks of collagen fibers which determine the passive mechanical properties of the myocardium. It is assumed that the preferred current flow directions are co-aligned between the two spaces, but that the conductivity

ratios between the principal axes are unequal between the two domains. As a consequence, direction and speed of propagation is constantly modified by interactions with discontinuous spatial variations in material properties at various spatial scales.
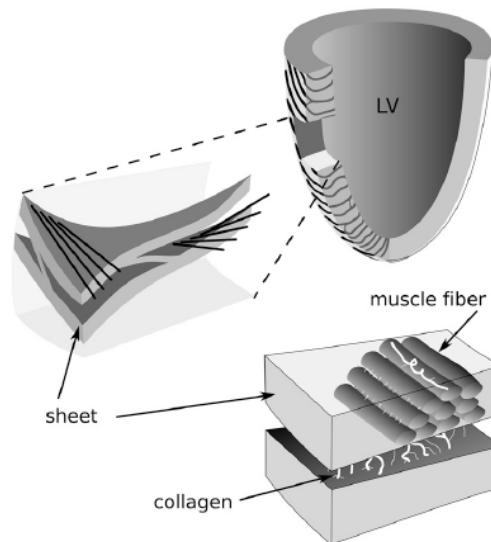
Figure 1.3: Fibers and sheets in the ventricles. Schematic representation of cardiac microstructure. Adapted from Le Grice et al. [47]

1.4 Electrophysiology of cardiac cells

In this section, a description of basic cardiac electrophysiology is included to provide a background. Each cardiac cell is encapsulated within a thin (5-7 nm) membrane. The cell membrane is a phospholipid bilayer acting as a separator between the extracellular and intracellular space. Both environments are made of aqueous solutions of salts dissociated in ions. Woven into this bilipid shell are membrane-spanning proteins that combine to form small pores in the cell membrane, see Fig. 1.4. Under most circumstances these pores may allow only specific ion to pass through the membrane and then only under certain conditions. These pores are often referred to as *ion channels*. The selective permeability property allows a potential difference to form between the inside and the outside of the cell. The main ions that are of interest in cardiac electrophysiology are Na^+, K^+ and Ca^{2+}, whose concentrations under resting conditions are given in Table 1.1.

Ion	$[ion]_I$ (mM)	$[ion]_E$ (mM)
Na^+	10	140
K^+	145	5.4
Ca^{2+}	0.00012	1.8

Table 1.1: intra- and extra-cellular principal ionic concentrations
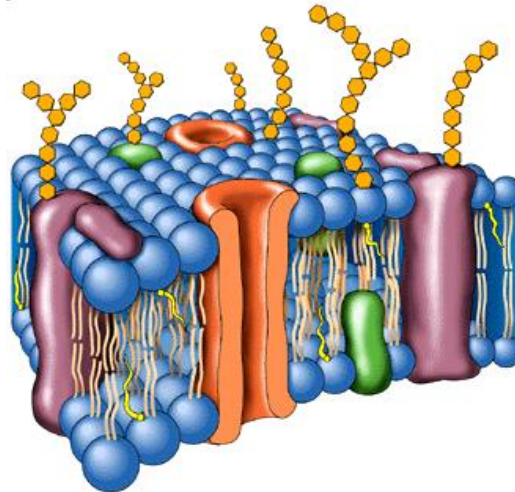
Figure 1.4: Schema rappresentativo della membrana cellulare.

The two forces acting on these ions to create the potential difference across the cell membrane are a chemical and an electrical force. When a concentration gradient of a particular ion species exists, the ions will naturally flow down this concentration gradient. This movement then causes an electrical gradient to be established that acts to oppose the chemical gradient. From Table1.1 it can be seen that, at rest, the intracellular and extracellular concentrations of each ion are substantially different. Therefore, an electrical gradient must exist that balances these concentration differences. The potential at which the chemical and electrical forces acting on a single ion species are in equilibrium (the electrochemical equilibrium) goes by two main names. In some circumstances this potential is called the *reversal potential* as it represents the potential at which the flux of the ion changes from one direction to the other. Mathematically this potential difference across the cell membrane can be calculated from the Nernst equation, (1.1), named after the German scientist Walther Hermann Nernst who developed the equation and therefore it is called *Nernst potential*. For a general ion x, the Nernst potential,

V_x, can be written as

$$V_x = \frac{RT}{z_x F} \ln \left(\frac{[x]_E}{[x]_I} \right), \tag{1.1}$$

where R is the universal gas constant (8.314 J mol^{-1} K^{-1}), T is the absolute temperature, z_x is the valence of the ion x and F is the Faraday's constant (96,485 C mol^{-1}). The Nernst equation (1.1) can be derived from thermodynamic considerations of the free energy changes involved, for more details we refer to [42]. According to Table 1.1 and (1.1) we have $V_{Na} = 70$ mV, $V_K = -88$ mV and $V_{Ca} = 128$ mV. The resting potential of a cell therefore depends on these Nernst potentials and the relative permeability of the membrane to each of these ions.

The potential difference set up across the cell membrane is known as the transmembrane potential (or membrane potential) and is given the symbol v_M. By convention it is computed as the difference between the intracellular potential, u_I, and the extracellular potential, u_E,

$$v_M = u_I - u_E.$$

The regulation of the membrane potential through the activity of the ion channels is at the basis of the description of the bioelectric activity of the heart.

1.5 Ion channels

Ion channels are pore forming membrane proteins whose function include establishing a resting membrane potential by gating the flow of ions across the membrane.

There are three distinctive features of ion channels:

- permeability: the ability of an ion to move through the channel. Ions pass through the channel down their electrochemical gradient, without the input of metabolic energy (e.g. ATP, co-transport or active transport mechanism);

- selectivity: the degree to which a channel allows a specific ion to pass while excluding others;

- *gating*: the process of conformational changes of an ion channel transforming between any of its conducting and non-conducting states.

A variety of cellular changes can trigger gating depending on the ion channel, including changes in voltage across the membrane (voltage-gated ion channels), drugs
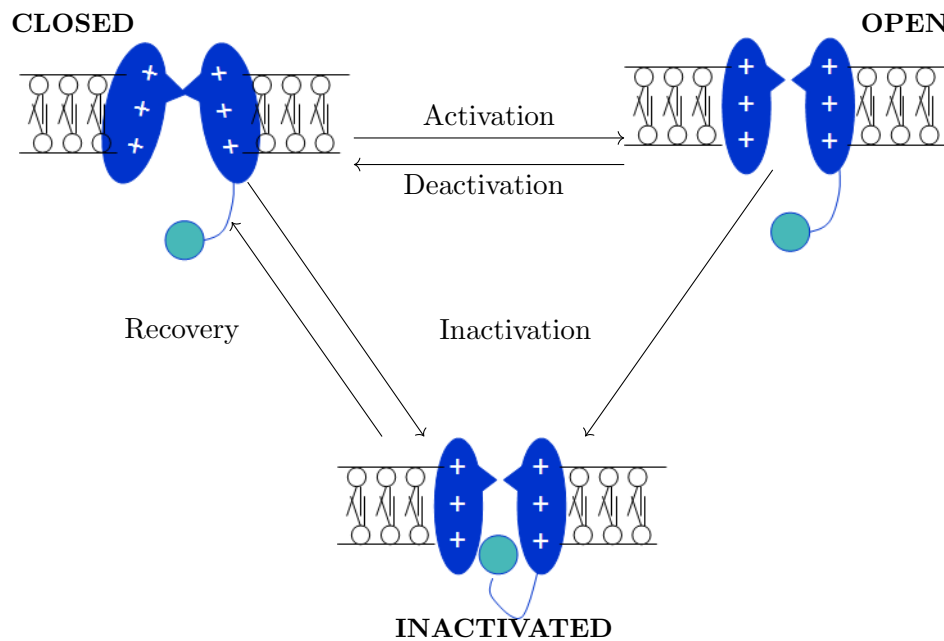
Figure 1.5: Schematic representation of voltage gated channel states.

or hormones interacting with ion channel (ligand-gated ion channels), stretching or deformation of the cell membrane. The rate at which any of these gating process occurs are known as the kinetics of gating.

The voltage-gated channels are often describe as having four gating process: *activation*, *deactivation*, *inactivation* and *recovery* from inactivation. Activation is the opening of a channel due to the presence of a gating signal; deactivation is the closing due to removal of the gating signal (i.e. the opposite of activation); inactivation is the closing of a channel in the continued presence of the gating signal, finally recovery is the opposite of inactivation. A depiction of this process is shown in Fig. 1.5. We now briefly describe the main channel involved in an action potential.

Sodium channels

Voltage-gated sodium channels can be activated by a slight depolarization and they produce an intense inward current of Na^+ ions (by convention negative, and denoted by I_{Na}).

Calcium channels

Two types of voltage-dependent calcium channels play a role in cardiac cells, the L-type (*long-lasting*) and T-type (*transient*) channels, whose names reflect their main features. L-type also have a lower threshold for activation than T-type and because T-type carry a smaller depolarizing current, T can also stands for "tiny". L-type Ca^{2+} channel are activated and inactivated by voltage and inactivated by high concentration of Ca^{2+} .

Potassium channels

The configuration of cardiac action potential varies considerably among species and different region of the heart, which is largely attributable to the diversity expression of the different types of time- and voltage-activated K^+ channels. Under physiological condition the current through these channel is always outward. The I_{to} (transient outward) has a fast activation and inactivation, it is important in the atria and subepicardial ventricle. The rapid and slow delayed rectifier potassium currents, I_{Kr} and I_{Ks} , respectively, are, together with the inward rectifier current I_{K1}, the primary currents responsible for repolarizing the myocyte membranes in the final part of the action potential and thereby terminating it (phase 3).

HCN channels

Hyperpolarization-activated cyclic nucleotide-gated (HCN) channels are sometimes referred as the pacemaker channel because they help to generate rhythmic activity within groups of heart cells, they are highly expressed in spontaneously active cardiac region, such as the sinoatral node and Purkinje fibers. The current flowing through the HCN channels is called *funny* current (I_f), described for the first time by DiFrancesco Nooble e Brown in 1979 [13]. The atypical features of this current justify its name. It is a mixed current potassium current that activates upon hyperpolarization at voltages in the diastolic range (normally from -60/-70 mV to -40 mV) and has a slow kinetics. When at the end of a sinoatrial action potential the membrane repolarizes below the I_f threshold (about -40/-50 mV), the funny current is activated and supplies inward current, which is responsible for starting the diastolic depolarization.

1.6   Cardiac action potential

From the perspective of electrical activity, the most important property of cardiac cells is that they are excitable, some autonomously as the sinoatrial node cells (SAN cells). In fact, cardiac muscle cells have an inbuilt protection whereby small perturbation in the membrane potential elicits only a passive response. From such perturbation the transmembrane potential move back towards the resting potential. If a sufficiently large stimulus is given, the membrane potential rises above a critical value (*threshold potential*) and an active response occurs. This response, which actually is the time course of the membrane potential, is called the *action potential*. The waveforms of the action potentials in different region of the heart are distinct, as shown in Figure 1.6.
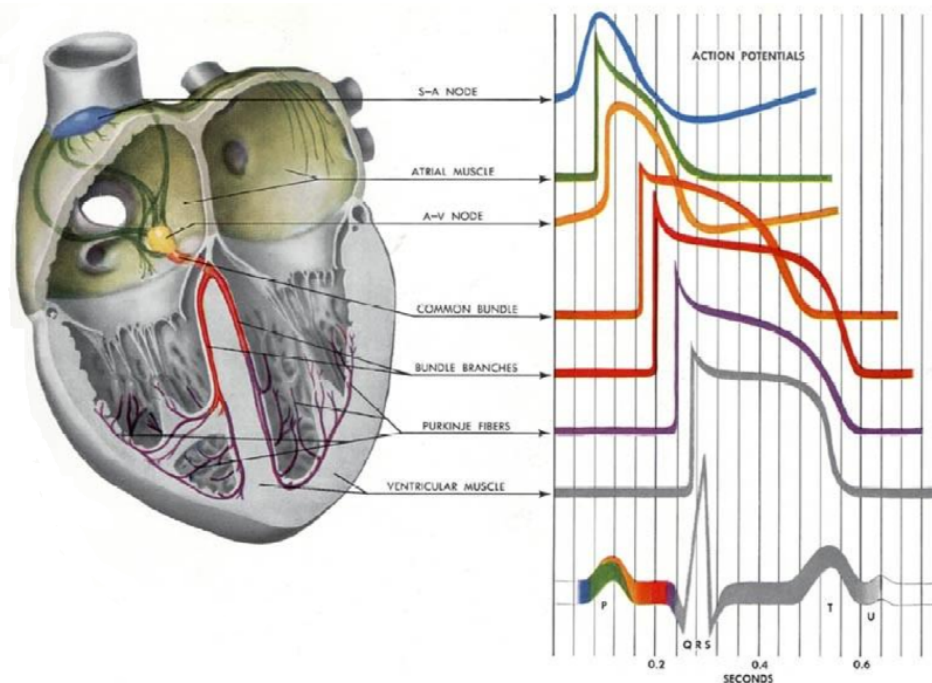
Figure 1.6: Pathways of electrical conduction in the heart and the corresponding action potentials.

Two main types of action potentials occur in the heart and are shown in Fig. 1.7. One type, the fast response, occurs in normal atrial and ventricular myocytes and in the specialized conducting fibers (Purkinje fibers of the heart) and is divided into five phases, as in Fig. 1.7(b).

Upstroke (Phase 0) Any stimulus that abruptly depolarizes the membrane po-

tential to a critical value (called the threshold) elicits an action potential. The rapid depolarization (phase 0) is related almost exclusively to the rapid influx of Na^+ into the myocyte as a result of sodium channels activation.

Early repolarization (Phase 1) This phase is due to the inactivation of Na^+ channels and outward flux of of K^+ (I_{to} current).

Plateau (Phase 2) This is the longest phase of the action potential. This phase is unique among excitable cells and is sustained by a balance between influx of Ca^{2+} through L-type Ca^{2+} channels ($I_{Ca,L}$) and efflux of K^+ through the slow-delayed rectifier K channels (I_{Ks}). The Na^+ -Ca^{2+} exchanger current (I_{NaCa}) and the Na^+ /K^+ also play minor roles during phase 2.

Rapid repolarization (Phase 3) the phase of rapid repolarization, restores the resting membrane potential. During this phase, the L-type Ca^{2+} channels close, while the slow-delayed rectifier (I_{Ks}) K^+ channels are still opened. This ensures a net outward current, corresponding to negative change in membrane potential, thus allowing more types of K^+ channels to open. These are primarily the rapid delayed rectifier K^+ channels, I_{Kr} , and the inwardly rectifying K current, I_{K1} . The delayed rectifier I_{Kr} channels close when the membrane potential is restored about -80 to -85 mV, while I_{K1} remains conducting throughout phase 4, contributing to set the resting membrane potential.

Resting (Phase 4) is the resting phase, during which the transmembrane potential remains at the resting value of about -84 mV until it is stimulated by an external electrical.

The slow response action potential occurs in the sinoatrial (SA) node, which is the natural pacemaker region of the heart, and in the atrioventricular (AV). nodeSA node cells fire spontaneously in a cycle defined by three phases, referred to as phase 4, phase 0, and phase 3, as shown in Fig. 1.7(a).

Diastolic depolarization (Phase 4) It consists of a slow, spontaneous depolarization that is caused by an inward pacemaker current I_f . This spontaneous depolarization accounts for the automaticity of the SA node. The channels that carry the I_f current are activated during the repolarization phase of the previous action potential.

Depolarization (Phase 0) is a more rapid depolarization mediated by highly selective voltage-gated Ca^{2+} channels that, upon opening, drive the membrane potential toward calcium resting potential V_{Ca}.

Repolarization (Phase 3). When the Ca^{2+} channels slowly close and K^+ -selective channels open, resulting in membrane repolarization. Once the mem-

brane potential repolarizes to approximately -60 mV, the opening of I_f channels is triggered and the cycle begins again.
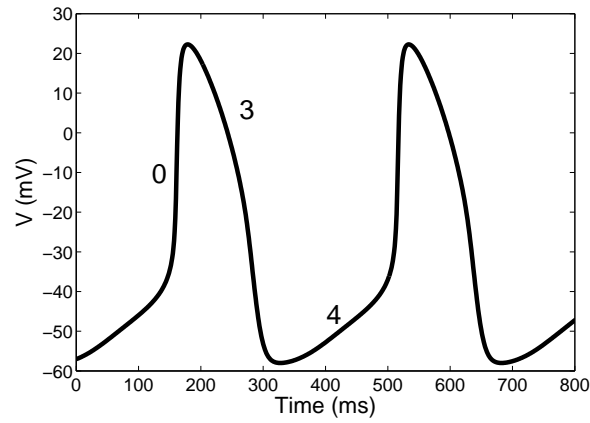
(a)
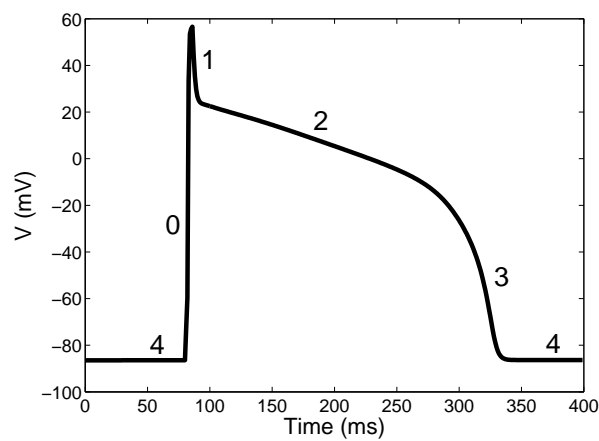
(b)

Figure 1.7: Phases of the sinoatrial node (a) and the ventricular myocardial cell (b) action potentials.

Chapter 2

Action Potential Modeling

At the molecular level, the electrical activity in the heart is generated by specialized membrane-spanning proteins that control the movement of ions either by passive electrodiffusion through transmembrane pores (channels) or translocation across the membrane by carrier proteins (pumps, exchangers, and transporters). As a first approximation, ion channels can be thought of as mediating the dynamic portions of the action potential, such as the upstroke and repolarization, and also providing the entry of trigger calcium to initiate excitationcontraction coupling. In contrast, pumps, exchangers, and transporters can be thought of as steadily working in the background to establish and maintain ionic gradients. Obviously, this is only an approximation: pumps, exchangers and transporters can and do contribute to the overall behaviour of the action potential too. Nonetheless, channels dominate depolarization and repolarization, and the process of repolarization is largely understood as the dynamic interaction of membrane ion channels. Consequently, in many situations the action potential can be approximated well using a model containing only channels. Membrane ion channels interact with dynamically changing ionic concentrations and varying transmembrane voltage, and are subject to various regulatory processes. These interactions are nonlinear, making the single cardiac cell a complex interactive system. In this chapter, we introduce mathematical approaches that provide a synthesis and an integration of this processes, in order to describe the electrical activity of a whole cell; the milestone work for quantitative modelling of ion channels is the one by Hodgkin-Huxley [37]. Their equations are purely empirical, since they were developed long before channel structure was known. However they introduced a formalism that is still adopted, even though advances in electrophysiological techniques and molecular biology have allowed us to build new models of the biophysical properties

of ion channels based on their molecular structure. At the end of the chapter a novel sinoatrial action potential model is introduced, which, adopting the Hodgkin-Huxley (HH) formalism integrated with a markovian model for calcium handling, tries to make a contribution to gain a deeper understanding of the cellular basis of cardiac pacemaking.

2.1 Ionic currents

Although the Nernst equation for the equilibrium potential can be derived from thermodynamic considerations (see [42]) and is thus universally applicable, there is no universal expression for the ionic current. The simplest model available for describing the uncoupled movement of a charged species though an open channel is given by the equation

$$I_x = \gamma_x(v_M - V_x), \tag{2.1}$$

where I_x and E_x are the current and the Nernst potential relative of ion x, respectively, while γ_x is defined as the conductance. In fact, this equation describes an ohmic conductor, as there is a linear relationship between current and voltage. Even though the Nernst equation can be used to calculate the correct reversal potential for an ion and the net driving force for an ion, the net flux is not always linearly related to the voltage difference as implied by this equation. An alternative model come out from the integration of the NernstPlanck equation, assuming a constant electric field, giving the Goldman Hodgkin Katz (GHK), or constant-field, current equation:

$$I_x = P_x \cdot z_x^2 \frac{v_M \cdot F^2}{RT} \frac{[x]_i - [x]_o \exp(-z_x \cdot v_M \cdot F/RT)}{1 - \exp(-z_x \cdot v_M \cdot F/RT)}. \tag{2.2}$$

where z_X is the valence of ion x, P_x is the permeability of the membrane for ion x, F the Faraday constant, R the gas constant, T the absolute temperature and $[x]_i$ and $[x]_o$ the internal and external concentration of ion x.

2.2 Electrical circuit model of the cellular membrane

Cole and Curtis, [24] measured cell membrane resistance and capacitance in nerve cells and showed that the electrical properties of the membrane are well
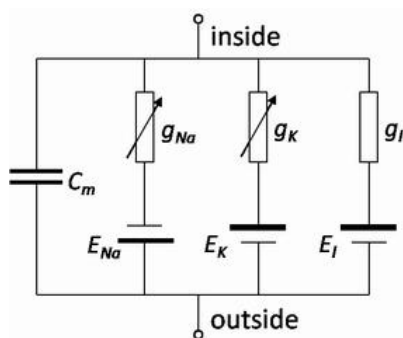
Figure 2.1: Electrical circuit model of the cellular membrane

represented by an RC circuit, as shown in Fig. 2.1. The capacitor represents the capacitance of the lipid bilayer that form the cell membrane, and the resistor represents the conductance of the ionic channels that are open at the resting potential.

The capacitance is defined as the ratio between the charge Q across the capacitor and the voltage potential v_M necessary to hold the charge

$$C_m = \frac{Q}{v_M}.$$

Since the capacitive current is $I_c = \mathrm{d}Q/\mathrm{d}t$, if C_m is constant, we have

$$I_c = \frac{\mathrm{d}Q}{\mathrm{d}t} = C_m \frac{\mathrm{d}v_M}{\mathrm{d}t}.$$

By the current conservation law, the transmembrane current given by the sum of the capacitative and ionic currents, must equal the applied current I_{app}

$$C_m \frac{\mathrm{d}v}{\mathrm{d}t} + I_{ion} = I_{app}. \tag{2.3}$$

The structure of the ionic current will be described by the specific ionic membrane model adopted. In order to discuss these models, we need to introduce the formalism for modelling ion channel gating.

2.3 Ion channel gating modelling

A channel pore conducts all-or-nothing according to whether its ion gates are open or closed. An open channel conducts with a single-pore conductance, the total

membrane conductance is the sum of the conductances of all the open channels. A transient channel has two ion gates, the activation gate and the inactivation gate. Accordingly, this channel is seen as having three states: (1) deactivated (activation gate closed, inactivation gate open); (2) activated (both gates open); and (3) inactivated (inactivation gate closed). A persistent channel has only two states, activated and deactivated, because it has only one gate. We suppose that individual channel gates open or close independently of one another but as a function of the membrane voltage.

The simplest model of a gating variable is the two state channel. We consider a membrane portion of unit area containing a given type of ionic channel that assume state only C (close) and O (open), The channel can pass from a state to the other according to the following diagram

$$C \underset{\beta}{\overset{\alpha}{\rightleftarrows}} O,$$
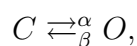
where α and β are the transition rate constant of opening and closing, respectively, and are function of the membrane voltage but not of time. If we denote by $C(t)$ and $O(t)$ the average number of channels that at time t are in the state C and O, respectively, for each time $C(t) + O(t) = T$, where T is the total number of ion channels. Applying the law mass action we obtain

$$\begin{cases} \dfrac{\mathrm{d}O}{\mathrm{d}t} = \alpha\, C - \beta\, O \\ C + O = T. \end{cases}$$

Eliminating C and denoting by $w := \frac{O}{T}$ the gating variable, we have

$$\frac{dw}{dt} = \alpha\,(1 - w) - \beta\,w \ . \tag{2.4}$$

By setting

$$w_\infty = \frac{\alpha}{\alpha + \beta} \tag{2.5}$$

$$\tau_w = \frac{1}{\alpha + \beta}; \tag{2.6}$$

this equation can be rewritten as

$$\frac{dw}{dt} = \frac{w_\infty - w}{\tau_w}. \tag{2.7}$$

2.4   Calcium handling

The intracellular calcium exerts profound influence on a vast variety of cellular processes. It is the central regulator of cardiac contractility, and according to the Ca^{2+} -clock theory (Sec. 2.6) could be important for the pacemaking. The key pathways involved in myocyte Ca^{2+} transport can be summarized as follows. Calcium ions enter the cell through the calcium channel ($I_{Ca,L}$ and $I_{Ca,T}$). This fact induce the release of more calcium ions from the sarcoplasmic reticulum by a process called calcium-induced calcium release (CICR), resulting in an elevation of intracellular calcium. This elevation of intracellular calcium is transient because calcium ions are taken up by the sarcoplasmic reticulum, and are extruded outside the cell by the sodium-calcium exchanger and a calcium pump, or intracellular calcium binds to cytosolic Ca^{2+} *buffers*. Therefore, the amount of free intracellular calcium in the myoplasm is determined by many processes: the calcium that enters and exits the cell through ionic channels, the calcium that leaves the cell through the Na-Ca exchanger, the calcium that is taken up and released from the sarcoplasmic reticulum, and the calcium that is bound to some cytosolic proteins.

Calcium fluxes

Calcium fluxes in the sarcoplasmic reticulum, represented by J, represent changes in ionic concentrations per unit time and have units of mM/s.

Several models describing the uptake and the release of calcium by the sarcoplasmic reticulum (SR) can be found in literature. The SR occupies about 1% and 6% of the cell volume, in sinoatrial and ventricular cell, respectively. It consists of two compartments: the network sarcoplasmic reticulum (NSR), where calcium is uptaken in the SR, and the junctional sarcoplasmic reticulum (JSR), from which calcium is released to the cytoplasm. The NSR occupies about 90% the SR volume, and the JSR the rest.

We can model the fluxes in the SR by formulating the *uptake* (J_{up}) from NSR, the calcium translocation from the NSR to the JSR (J_{tr}) and the release from the JSR (J_{rel}). The uptake is performed by a metabolic pump by a Hill equation

$$J_{up} = P_{up} \frac{[Ca]_i}{[Ca]_i + K_{up}},$$

where P_{up} is the maximum pump rate, $[Ca]_i$ is the intracellular calcium concentration and K_{up} is the half-activation concentration, i.e., the $[Ca]_i$ at which the pump rate is half of its maximum) and n is the order of the biding process.

The flux of calcium ions from the NSR to the JSR can be formulated as

$$J_{tr} = \frac{[Ca]_{nsr} - [Ca]_{jsr}}{\tau_{tr}},$$

where $[Ca]_{nsr}$ and $[Ca]_{jsr}$ are the calcium concentrations in the NSR and JSR, respectively, and τ_{tr} is the time constant of the translocation.

The release of calcium from the JSR is a process that is more complex than the other calcium fluxes discussed so far, because the rate of release from the JSR depends on the concentration of intracellular calcium by the process of CICR. Old models as DiFrancesco and Noble [58] and Luo and Rudy [51] assume that the JSR release calcium into the myoplasm, more recent model, as those proposed by Shannon et al. in [70], assume that there exist a *submembrane* space, also called *junctional cleft*, where calcium is released, before to spread into the cytoplasm. This distinction recognizes the fact that the concentration in the submembrane space, which influences both the NaCa exchange current and the calcium-dependent inactivation of calcium current, is much larger during release than the average bulk concentration inside the myoplasm, due to the proximity of this space to dyadic junctions. The formulation of calcium release in their model is

$$J_{rel} = k_s \cdot O \cdot ([Ca]_{jsr} - [Ca]_{sub}),$$

where $[Ca]_{sub}$ is the concentration of free calcium in the *junctional cleft*, k_s is the maximum rate of calcium release, and O is the probability that the release channel is open.

The JSR releases calcium through ryanodine receptors (RyR), (Fabiato [30]). Ryanodine receptors are so named because of their sensitivity to ryanodine, which decreases the open probability of the channel. One of the earliest model of the ryanodine receptors is due to Stern et al. [74], and shown in Fig. 2.2; this is a four state model with closed states R and RI, inactivated state I and open state O. Transitions between these states are calcium dependent, reflecting binding of calcium to binding sites. A modification of the Stern et al model is used in [70], in which the rate constants of activation and inactivation are assumed to be dependent on the concentration of calcium in the submembrane, through a Michaelis-Menten equation. Other groups have developed RyR models of greater or lesser complexity, However, there is still no consensus as to which of this multitude of models best describes RyR behavior in vivo, we refer to [42] for further details.
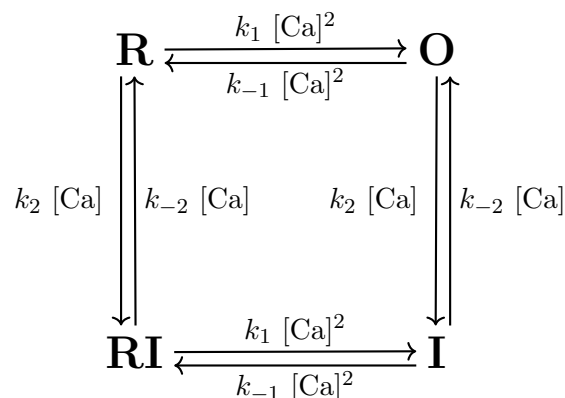
Figure 2.2: Markovian state model of ryanodine receptor.

Calcium buffering

In addition to its role in cardiac excitation, intracellular calcium regulates many intracellular process by binding to cytosolic proteins. For example, troponin is a contractile protein that binds intracellular calcium, and detects a rise in intracellular calcium as a signal to initiate the interactions between other contractile proteins (actin and myosin) that activate the process of muscle contraction. Intracellular calcium also binds to other proteins such as calmodulin. Similarly to troponin, calmodulin responds to a rise of intracellular calcium. Calmodulin is involved in the regulation of metabolic pathways of energy production, muscle contraction, and neurotransmitter release. The fact that calcium binds to cell proteins modulates the amount of free calcium, and, as a result, the cell excitation. The binding of calcium to some proteins has a buffering effect that keeps intracellular calcium concentration at a low level, more than 90% of intracellular calcium binds to a protein.

In its most simplified form, calcium buffering can be modelled using the same formalism used in enzymatic reaction. If the concentration of the buffer is [B] and the concentration of intracellular calcium is $[Ca]_i$, then the binding of the calcium to the buffer can be modelled as a chemical reaction as follows:

$$[Ca]_i + [B]_{\text{free}} \underset{k_{bB}}{\overset{k_{fB}}{\rightleftarrows}} [BCa],$$
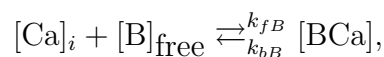
where $[B]_{\text{free}}$ is the concentration of free buffer, $[Ca]_i$ is the concentration of free intracellular calcium and [BCa] is the concentration of buffer bound to calcium. The forward rate constant is $k_{f}B$, and the reverse rate is $k_{b}B$.

2.5   Luo-Rudy I model

In the next two sections we introduce two models of action potential of myocytes ventricle cells and of sinoatrial node cell, respectively.

In 1991, Ching-hsing Luo and Yoram Rudy published a mathematical model of the cardiac action potential in guinea pig ventricular cells, [50], based on the Beeler-reuter model [8]. This was the first of two models, and it has subsequently come to be known as the Luo-Rudy I model (LR1). In this model the ionic current I_{ion} is the sum of six currents

$$I_{ion} = I_{Na} + I_{si} + I_K + I_{K1} + I_{Kp} + I_b, \tag{2.8}$$

two inwards (I_{Na}, I_{si}) and four outwards (I_K, I_{K1}, I_{Kp}, I_b). The first three currents depend on six gating variables and on intracellular calcium concentration, while the last three are time independent. The detailed formulation of the ionic currents are reported in Appendix A. The fast inward sodium current I_{Na} is primarily responsible for the rapid upstroke of the action potential, while the other currents determine the configuration of the plateau and repolarization phases. The slow inward current I_{si}, primarily carried by calcium ions, influences the duration of the action potential. The time-dependent and time-independent outward potassium currents I_K and I_{K1} are instead responsible for the repolarization phase. The plateau potassium current I_p plays a role during the plateau phase of the action potential, restoring the cell to its resting state. Background current I_b is a linear function of the transmembrane potential.

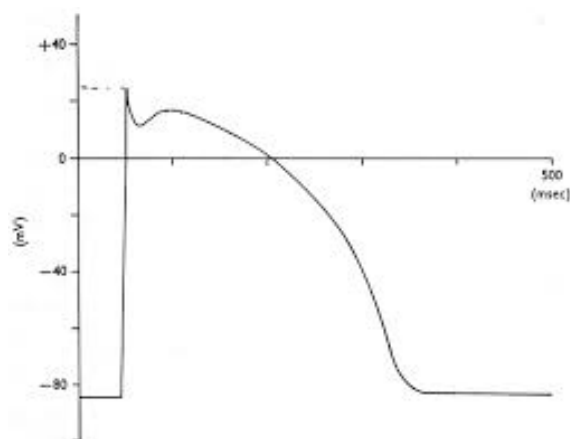In Fig. 2.3 is reported the action potential produced by the LR1 model.

Figure 2.3: An AP waveform generated by the LR1 model.

2.6   An updated sinoatrial action potential model

Over the past half century, there has been an intense and fruitful interaction between experimental and computational investigations of cardiac function. This has led, for example, to more profound understanding of cardiac excitation-contraction coupling: how it works, as well as how it fails. However, many lines of inquiry remain unresolved, among them the initiation of each heartbeat. The sinoatrial node, a cluster of specialized pacemaking cells in the right atrium of the heart, spontaneously generates an electro-chemical wave that spreads through the atria and the cardiac conduction system to the ventricles, initiating the contraction of cardiac muscle essential for pumping blood to the body. Despite the fundamental importance of this primary pacemaker, this process is still not fully understood, and ionic mechanisms underlying cardiac pacemaking function are currently under heated debate.

Since its discovery in 1979 [13], the inward *funny* current (I_f) has held a prominent place in the understanding of this process. In fact, many textbooks and review articles refer to I_f as the *pacemaker current* [4, 5], a term that implies primacy. The properties of I_f make it seem almost ideally suited for pacemaking: it slowly activates at the negative membrane potentials of diastole, and the inward current it supplies can drive a slow depolarization towards the action potential threshold [27]. This mechanism, whereby spontaneous beating results from voltage and time-dependent changes in ionic currents, has been termed a *membrane clock*, or M-clock. However, the hypothesis that the funny current plays a dominant role in pacemaking has not gone unchallenged. In recent years, studies from several groups have suggested that periodic spontaneous release of Ca^{2+} from the sarcoplasmic reticulum plays a critical role in SA nodal pacemaking [45, 44]. According to this hypothesis, local release of SR Ca^{2+} near the cell membrane leads to Ca^{2+} extrusion from the cell via the Na^+Ca^{2+} exchanger (Na-Ca). Because Na-ca is electrogenic, Ca^{2+} removal results in an inward current that contributes to diastolic depolarization. This general mechanism has been called the Ca^{2+}-clock.

Mathematical modelling of SAN cells has a long history, beginning with models developed in the early 1980s, such as the famous DiFrancesco-Noble model, [29]. In subsequent years, ion transport pathways have become more clearly defined, and models have generally increased in complexity to reflect new knowledge about the channels, transporters, and pumps that may contribute to pacemaking. In 2009, Maltsev and Lakatta first developed a model (the ML model, [52]) of a coupled membrane- and Ca^{2+}-clock to address the ionic mechanism of cardiac pacemaking.

They concluded that only a coupled system of membrane- and Ca^{2+} -clocks offers both the robustness and flexibility that are required to maintain normal pacemaking function, and their model predicts that the most important pacemaker current during late DD is the inward I_{NaCa}, instead of I_f. Unfortunately this model, as the previous (e.g. [43]), fails to reproduce a number of experimental data, and more specifically effects of I_f modifications. In order to test the hypothesis that a quantitatively important role of I_f in pacemaking and rate modulation is fully compatible with the recently proposed description of intracellular calcium handling, in collaboration with Dario DiFrancesco (University of Milan) and Stefano Severi and Matteo Fantini (University of Bologna), we developed a SAN AP model, [69], based on available experimental data. We selected the rabbit SAN as a basis for our model, and aimed at using species-specific data whenever possible for improved consistency. The model was constructed based on the mathematical formulation of rigorously selected ionic currents and pump/exchange mechanisms derived from relevant published experimental data. The model was then validated by simulating the action of pharmacological and autonomic agents that modulate SAN rate and comparing numerical reconstructions with experimental results from the literature. Model equations are provided in Appendix B. Moreover, the model code is published in the CellML repository [49], (http://www.cellml.org/).

2.6.1 Methods

The framework of the model and the computational strategy were the same as in work [29]. We adopted the intracellular Ca^{2+} handling formulation of the ML model, since it is the more advanced and tuned. Membrane currents, pumps and exchangers were reformulated based on a critical review of published rabbit experiments, however we only retained mechanisms for which clear experimental evidence is available. Fig. 2.4 shows a schematic diagram of the model. The model follows the classical Hodgkin-Huxley formulation, and consists of ten currents. The differential equation for the membrane potential is

$$\frac{\mathrm{d}v_M}{\mathrm{d}t} = -\frac{I_{tot}}{C_m} \tag{2.9}$$

$$I_{tot} = I_f + I_{Kr} + I_{Ks} + I_{to} + I_{NaK} + I_{NaCa} + I_{Na} + I_{CaL} + I_{CaT} + I_{KACh}, \tag{2.10}$$

where $I_{Ca,L}$ and $I_{Ca,T}$ represent the L-type and T-type Ca^{2+} channel currents, respectively. The rapid and slow components of the delayed rectifier K$^+$ current are denoted as I_{Kr} and I_{Ks} , respectively. The membrane current system also
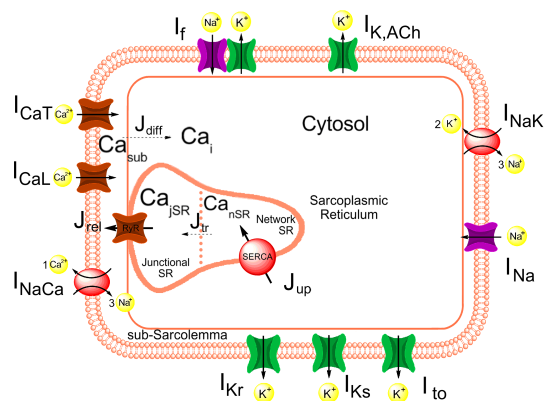
Figure 2.4: Diagram of the SAN cell model.

includes the transient (I_{to}), the hyperpolarization-activated (*funny*) current (I_f), a very small inward Na^+ channel current (I_{Na}), a muscarinic K^+ channel current ($I_{K,ACh}$), Na^+ -K^+ pump current (I_{NaK}), and sodium calcium exchanger current (I_{NaCa}) charging the membrane capacitance (C_m). Model equations for channel gating behaviors are essentially the same as those of the previous Hodgkin-Huxley type models. Hereafter we describe in detail few relevant currents.

Funny current (I_f)

I_f is described as composed of two relatively independent Na^+ and K^+ components, whose contributions to the total conductance at normal Na^+ and K^+ concentrations, are similar. As according to the original description in [28], I_f is also modulated by the extracellular potassium concentration, and we assumed, as in the DiFrancesco-Noble model [29] that this dependence is a first order binding process. For the gating mechanism, we adopted Hodgkin-Huxley second order kinetics as [57]. Our formulation of the steady-state activation curve fits the experimental results of [2] and [4], from DiFrancesco's group, and describes an activation curve positioned around a half-activation potential of -64 mV; notice that previous SAN models and also ML, based on data from [80], assumed a much more negative activation curve (Fig. 2.5A). The time constant curve (τ_f) was formulated on the basis of data from [57] (Fig. 2.5B), here too, our τ_f curve is shifted to more depolarized voltages relative to that of other models.
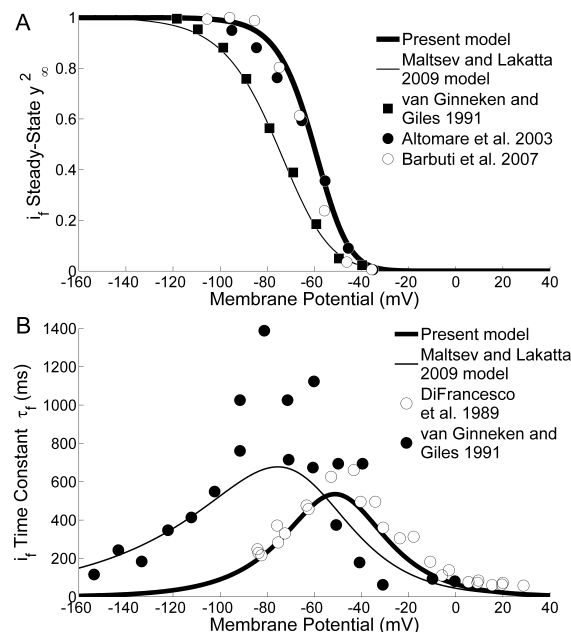
Figure 2.5: A: I_f activation curve. Plotted are the curve used in our model (thick line), based on data from [2] and [4](filled and open circles, respectively) and the ML model curve (thin line), based on data from [80](filled squares). B: If time constant curve. Comparison between our curve (thick line) based on [57](open circles) and ML model curve (dashed line) based on [80] data (filled circles).

L-type and T-type calcium current ($I_{Ca,L}$, $I_{Ca,T}$)

The kinetics of $I_{Ca,L}$ are described with activation (d_L), voltage-dependent inactivation (f_L), and Ca^{2+} -dependent inactivation gating variables. The voltage dependences of the steady-state activation and inactivation curves are shown in Fig.2.6. The formulations of were based on the data from Fermini and Nathan [32]. Actually, also ML models and other models ([43] and [26]) all quoted the same experimental data but with successive adjustments, motivated by the need of improving the fitting on the action potential data, that progressively make their current formulation significantly far from experimental evidences, Fig. 2.6. Expression of the activation time constant was based, as already done for Maltsev, Kurata and Demir models, on the whole cell data of [56] (guinea pig SAN myocytes at 25 °C), because specific data on rabbit SAN are not available. A Q10 factor of 2.3 was applied to scale these data for a temperature of 37°C. In addition, the time constant relationship was shifted to align it more properly with the steady-state activation curve. We formulated the inactivation time constant from data

from [54, 40, 33]. Formulation for the Ca^{2+} -dependent inactivation were adopted from the Kurata model, as already done by the Maltsev model. We adopted the constant-field formulation to describe the conductance property of ICaL, which is known to have small but not negligible components carried by Na^+ and K^+ ions.

As in the case with $I_{Ca,L}$, $I_{Ca,T}$ the steady state activation and inactivation curves are the Boltzmann curves fitting the data of Fermini and Nathan [32], while ML refers to data from [33]. We used this work for the expression of the time constant of inactivation, by fitting the data through a least square procedure. As done for $I_{Ca,L}$, we opted for the constant-field equation for the conductance property, setting the calcium permeability to 0.02 nA/mM., in order to maintain a constant total current during the diastolic depolarization phase.

Figure 2.6: A, $I_{Ca,L}$ activation and deactivation curves. Our activation and deactivation curves (thick lines), based on [32] data (filled and open circles, respectively), are compared with those of the Kurata et al model KHIS (grey line) and ML models (thin line). B, time constant of $I_{Ca,L}$ inactivation. The plot shows our curve (thick line), the curve of the ML model (thin line) and experimental data from [54] (open squares), [33] (open circles) and [40] (filled triangles).

Rapid and slow delayed rectifier (I_{Kr} , I_{Ks})

The expression of these components in SAN cells are species dependent. In rabbit SA node, both currents are present, but I_{Kr} is the predominant component. Although contribution of I_{Ks} to beating rate is small under control condition, it contributes significantly during $\beta-$adrenergic stimulation, [48]. The work of Ono and Ito [59] for rabbit SAN cells at about 33°C reported complete quantitative
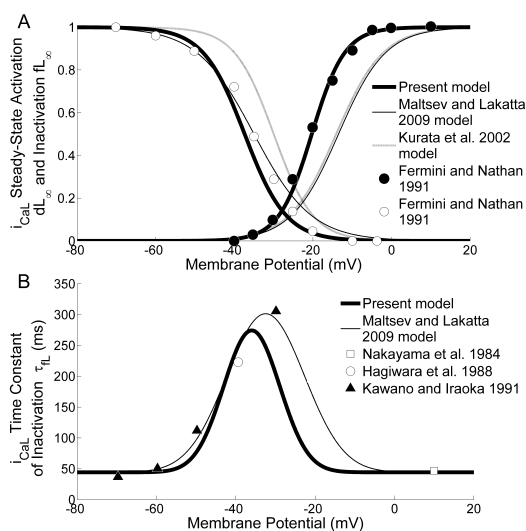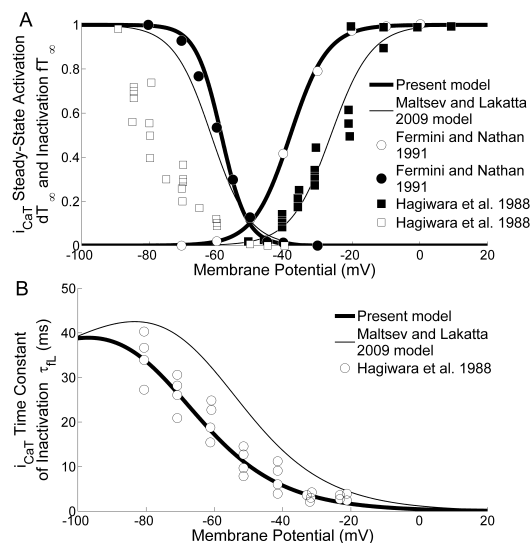
Figure 2.7: A, $I_{Ca,T}$ activation and deactivation curves. Our activation and deactivation curves (thick lines), based on [32] (filled and open circles, respectively), are plotted along with the curves of the ML model (thin lines) and data from [33] (filled and open squares, respectively). B, time constant of $I_{Ca,T}$ inactivation. Compared are our curve (thick line), based on [33] (open circles) and the ML model curve (thin line).

data on the activation of I_{Kr} . According with their study, activation and deactivation is well modeled through two activation variable: a fast activation variable (pa_f) and a slow (pa_s). The general activation variable (pa_s) is a convex linear combination of paf and pas. We adopted the mathematical description of Ono and Ito for the activation and inactivation kinetics of I_{Kr} . In order to improve the overall AP morphology, the steady-state activation variable and time constant of fast activation were slightly modified. Since no detailed experimental data were reported by Ono and Ito on the voltage dependence of the time constant of inactivation, for this variable we used the expression provided by Shibasaki [71], as in the ML model.

The slow activation of I_{Ks} is described by the formulation provided by Zhang model [85], subsequently adopted by Kurata and Maltsev. In this work I_{Ks} was modeled using second order Hodgkin-Huxley kinetics. The steady-state function was from data in Lei and Brown 1996, from rabbit SA node cells at 37°C. There are limited experimental data for the time constant of the voltage-dependent activation of I_{Ks} in rabbit SAN cells. Zhang model used formulation by Heath and Terrar, [35], based on their data from guinea-pig ventricular cells. With respect this approach, we opted for a new formulation of the time constant curve, in order to

reproduce the AP-clamp results from rabbit sinoatrial node cells of [48]. With this aim we adjusted the conductance, g_{ks}, setting its value at 45 nS. Fig. 2.8 shows our time constant curve in compared to that in ML model (i.e. Zhang model) and Heath and Terrar data.
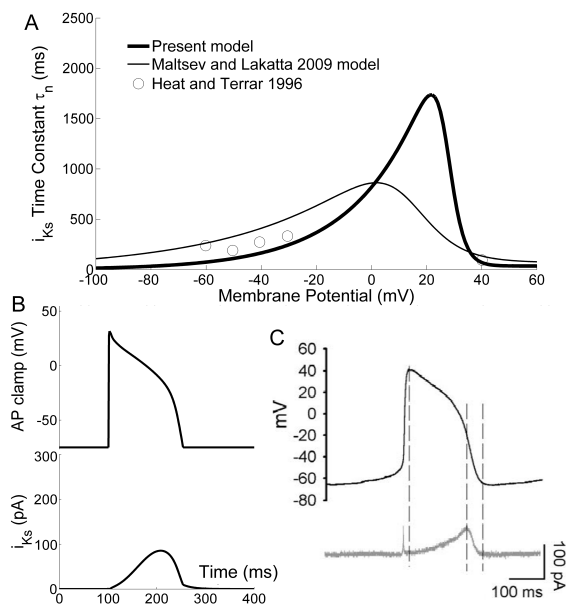
Figure 2.8: A: time constant of activation of I_{Ks} our formulation (thick line) and that of ML model (thin line, also shown experimentaldata from [35] (open circles). B: simulation of AP-clamp, reproducing the results of the experiments of [48] in C)

2.6.2 Validitation

For simulations we used Cellular Open Resource (COR) on a Windows 7 PC with an Intel Core 2 Quad processor. Integration was performed by the CVODE algorithm, using Backward Differentiation Formulae (BDF) together with a Newton iteration.

Action potential features during control

Before validating our model against specific rate modulation agents, we assess the basic features of the action potential. As shown Table 2.1 each of the basic characteristics of our model is within the range of experimental measurements. The AP waveforms generated by the model (Fig. 2.9) mimic closely those recorded

Feature	Model values	Experim. values (mean±SD range)
CL (ms)	352	352±42
MDP (mV)	-58	-56±6
APA (mV)	80	87±6
POP (mV)	22	27±6
APD_{50} (ms)	108	93±12
dV/dt_{max} (mV/ms)	7.1	11.3±6.5

Table 2.1: Simulation data from different models compared with experimental AP characteristics from 12 studies at physiological temperatures (Table 1 in [43]). CL, cycle length; MDP, maximum diastolic potential; APA, action potential amplitude; POP, peak overshoot potential; APD50, AP duration at its half-amplitude; dV/dtmax, maximum rate of rise of membrane potential during AP upstroke.

in rabbit SAN cells in normal Tyrode solution at a Temperature of 34-37°C. In particular our AP is able to reproduce one aspect of membrane potential morphology that is relevant for SAN function, that is the profile of the early diastolic depolarization (DD). It is well known that for rabbit SAN AP the membrane potential increases linearly during the early DD phase, followed by an exponential-like increase during the late DD. The latter is mainly driven by Ca^{2+} fluxes due to the activation of $I_{Ca,L}$ and to Ca^{2+} extrusion by the Na^+ -Ca^{2+} exchanger.
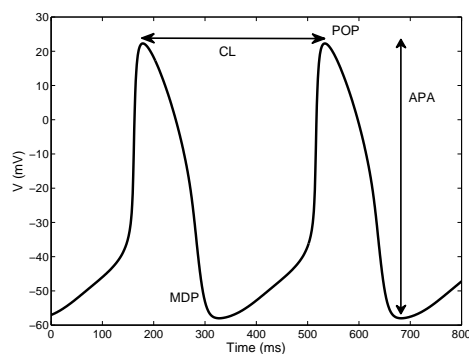
Figure 2.9: Simulation of 800 ms of spontaneous electrical activity in the rabbit SA node.

I_f blockade

A large amount of data shows that the use of drugs at concentration known to produce only partial block of I_f leads to a significant AP rate reduction. Ivabradine is just a medication that reduces the heart rate via specific inhibition of the *funny channel*. The action of Ivabradine is simulated by a partial block of funny channels (66% reduction of I_f conductance, as reported with a 3 μM concentration by Bucchi et al [14]. The assumption of a constant block during pacemaking activity is a good approximation because of the extremely slow block kinetics of ivabradine. The model predicts a reduction of spontaneous rate (Fig.2.10) of 22% in agreement with experimental findings, at the same time, neither the TOP (-42 vs. -41 mV) nor the MDP (-59 vs. -58 mV) is altered by the drug, as also verified experimentally [15].
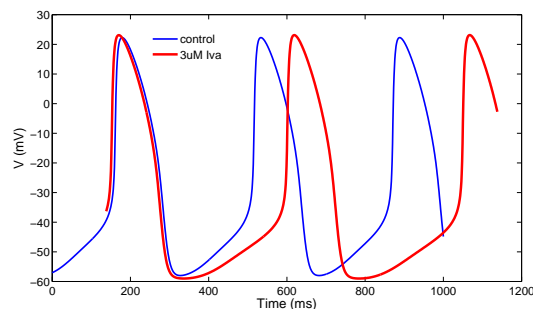
Figure 2.10: Simulation of the action of 3μM Ivabradine on spontaneous activity

Finally we simulate increasing level of I_f current blocks. Our model predict progressive prolongation of the CL, up to complete cessation of pacemaking only when I_f is fully blocked (Fig. 2.11). This observation, indicates that the weight of I_f has been significantly underestimated in previous models. Our results demonstrate that it is possible to reproduce realistic I_f rate modulation properties without dramatically change other model components, in particular without modifying the calcium handling description.

Adrenergic modulation of rate

Isoprenaline-induced rate acceleration, especially at low-to-moderate doses, is attributable mostly to the shortening of DD associated with a faster slope of DD, while action potential duration and shape vary minimally as reported in [15, 27]. The positive chronotropic effects of Iso 1 μ Fig. 2.12 were simulated by shifting
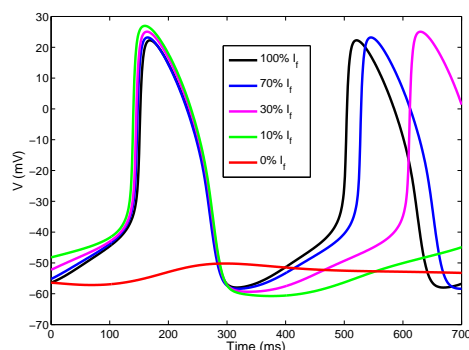
Figure 2.11: Simulation of the effects on action potential of increasing I_f block.

the I_f activation gating variables by 7.5 mV to more positive voltages [84] and by modulating $I_{Ca,L}$, I_{Ks}, I_{NaK} and the Ca^{2+} release uptake rate P_{up}, for more detail see [69]. Specifically, 1μ Iso increases the amplitude of $I_{Ca,L}$ by 75% [82]; this enhancement was reconstructed by shifting the activation curves (Nagykaldi et al. 1999;Ke et al. 2007) to more negative values (-8mV), by decreasing the inverse of slope factor of the activation variable (-31%) and by increasing the maximal conductance (+23%). Similarly, I_{Ks} maximal conductance was increased by 20% and its activation curves were shifted by 14 mV to more negative potentials in order to increase the current amplitude. A 20% increase of the maximal conductance of I_{NaK} was also introduced, according to Zeng and Rudy model. Finally, since the presence of a β-adrenergic agonist affects the SR Ca^{2+} -pump, but no quantitative data are available, we estimated an increase of P_{up} of 25% of its control value. The overall simulated effects of 1μ Iso was a 28.2% rate increase, in good agreement with the reported experimental value of 26.3±5.4% for the same Iso concentration [15]. The rate increase was entirely due to increase in the DD slope, with only minor changes in MDP and TOP.

Ca^{2+} buffering by BAPTA

BAPTA (1,2-bis(o-aminophenoxy)ethane-N,N,N',N'-tetraacetic acid) is a Ca^{2+} chelator, i.e. it is a molecule that binds calcium and cover the ion in a way it is no longer available for cellular metabolism. Ca^{2+} buffering by BAPTA is simulated according to the Kurata model, [43], in both the cytoplasm and subsarcolemmal space, in an attempt to reproduce Himeno et al (2011) experiments, [36]. In this work the authors note that experimental rupturing of the perforated-patch membrane to allow rapid equilibration of the cytosol with 10 mM BAPTA pipette
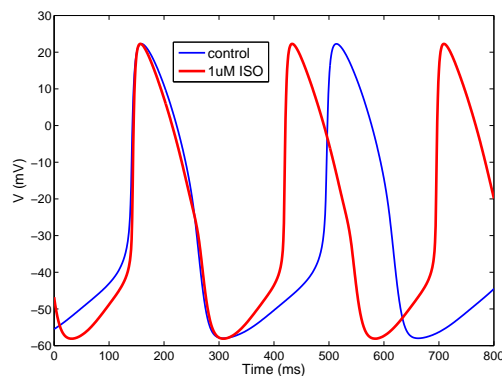
Figure 2.12: Simulation of the action of 1μM Isoprenaline on spontaneous activity

solution, failed to decrease the rate of spontaneous action potential within about 30 s, whereas contraction ceased within about 3 s, in a guinea pig SAN cell. The spontaneous rhythm also remained intact within a few minutes when SR Ca^{2+} dynamics were acutely disrupted using high doses of SR blockers. These experimental results suggested that rapid disruption of normal Ca^{2+} dynamic would not affect the pacemaking activity. Model testing of BAPTA effects show slowing of rate without cessation of beating Fig. 2.13 as reported in [36]; this result could not be reproduced by the ML model. In our simulation the spontaneous cycle length was increased up to 443 ms (-26% rate) and the AP amplitude was also significantly decreased.

(a)

(b)
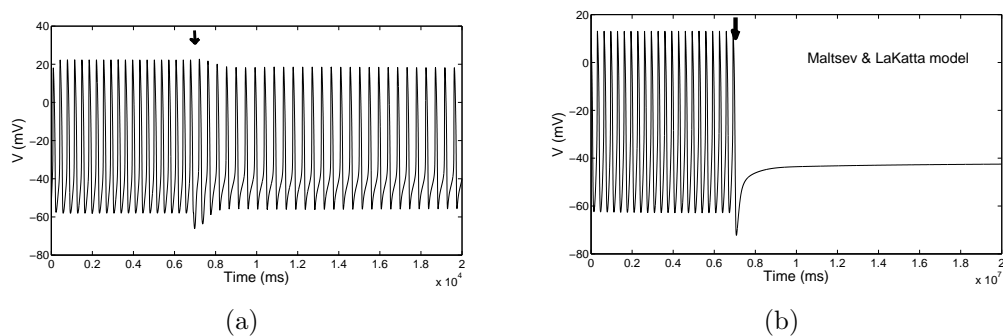
Figure 2.13: a), simulation of the effects of 10 mM BAPTA internal perfusion. b), same simulation in the ML model. Arrows in a) and b) indicate the beginning of the perfusion.

In conclusion, we have developed a novel computational model of physiological cardiac cell pacemaker function, able to reproduce a set of recent and less recent

experimental data relevant to generation and control of pacemaker activity. More specifically, our model reproduce satisfactorily the changes of pacemaking function associated with changes in I_f current and Ca^{2+} handling, as experimentally observed. The lack of sensitivity to I_f block in previous models can therefore be a consequence of incorrect estimation of membrane currents during diastolic depolarization

Chapter 3

Cardiac reaction-diffusion models

Cardiac muscles cells are excitable, responding actively to an electrical stimulus. As described in Chapter 1, myocytes are connected, so that the electrical signal can propagate by depolarization of adjacent cells mainly in the direction along fiber. The depolarization is a very fast process, and it is followed by a slow repolarization that restores the potential difference to the resting. A mathematical model describing the electrical activity in cardiac tissue need to take into account both the anisotropy of the tissue and the behaviour of the membrane potential in each single cell, so that it deals with the macroscopic and microscopic levels. We introduce a continuous approximations of the tissue based on a volume-averaged approach, which must be able to distinguish between the intracellular and extracellular domains. Since it takes into account both the intra-cellular and the extra-cellular domains, this model is called Bidomain, Sec. 3.1. For large scale simulations involving the whole ventricles, computer memory and time requirements become excessive, for this reason less demanding approximation have been developed such as the Monodomain model, introduced in Sec. 3.2, and Eikonal model, see [10, 41] and the recent survey [21].

3.1 The Bidomain model

At a microscopic scale, the cardiac structure is composed of a collection of elongated cardiac cells connected via gap junctions, embedded in the extracellular fluid. The gap junctions form the long fiber structure of the cardiac muscle, whereas the presence of lateral junctions establishes a connection between the elongated fibers. Since the interconnection between cells has resistance comparable

to that of the intracellular volume, we can consider the cardiac tissue as a single isotropic intramural connected domain, Ω_I, separated from the extracellular fluid, Ω_E, by a membrane surface Γ_m.

At a macroscopic level the cardiac tissue can be represented by a continuous model, the Bidomain model. It can be derived from a microscopic model, assuming the tissue as a periodic lattice, using a homogenization technique in a rigorous mathematical framework, as formalized in [62].

Another common derivation, adopted in [73], is based on the volume averaging technique. With this approach, the values of parameters and variables in each point of the domain are obtained by taking the average of the considered quantity in a volume centered in the point considered. The dimension of the region on which to compute the average should be large enough to contain a discrete amount of cells but small with respect to the scale of the considered tissue. Thanks to this averaging procedure, the resulting Bidomain model describes averaged intra- and extracellular potential by a system of reaction-diffusion of partial differential equations (PDEs), conceiving the cardiac tissue as the superimposition of two anisotropic continuous media: the intra- and extracellular domains, coexisting in each point of the tissue and connected by a distributed continuous cell membrane, that is

$$\Omega \equiv \Omega_I \equiv \Omega_E \equiv \Gamma_m \subset \mathbb{R}^3 \quad \text{the physical region occupied by the heart}$$
$$u_I, u_E : \Omega \times (0, T) \longrightarrow \mathbb{R},$$
$$v_M := u_I - u_E : \Omega \times (0, T) \longrightarrow \mathbb{R}.$$

All the quantities obtained by averaging over the extracellular domain will be denoted by the subscript E while those obtained by averaging over the intracellular domain will be denoted by the subscript I.

The anisotropy of the two media is characterized by the conductivity tensor D_I and D_E. These tensors are anisotropic in relation to the direction of the cardiac fibers, that rotates counterclockwise from epicardium to endocardium and to the laminar organization of the heart muscle [47]. Therefore, at any point $\mathbf{x}$, it is possible to identify a triplet of orthonormal principal axes $\{\mathbf{a}_l(\mathbf{x}), \mathbf{a}_t(\mathbf{x})\mathbf{a}_n(\mathbf{x})\}$ with $\mathbf{a}_l(\mathbf{x})$ parallel to the local fiber direction, $\mathbf{a}_t(\mathbf{x})$ and $\mathbf{a}_n(\mathbf{x})$, tangent and orthogonal to the radial laminae, respectively, and both being transversal to the fiber axis, see Fig. 3.1. Let $\sigma_l^{I,E}$, $\sigma_t^{I,E}$ and $\sigma_n^{I,E}$ be the conductivity coefficients measured along the corresponding directions. In general they depend on $\mathbf{x}$, nevertheless we will assume that they are constant; this case refers to homogeneous anisotropy. Since
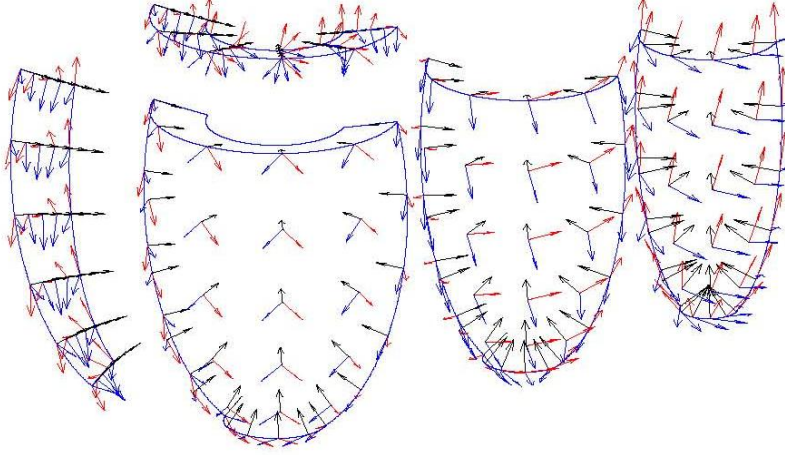
Figure 3.1: $\mathbf{a}_l(\mathbf{x})$ (red), $\mathbf{a}_n(\mathbf{x})$ (blue) and $\mathbf{a}_t(\mathbf{x})$ (black).

it holds

$$\mathbf{a}_l(\mathbf{x})\mathbf{a}_l^T(\mathbf{x}) + \mathbf{a}_t(\mathbf{x})\mathbf{a}_t^T(\mathbf{x}) + \mathbf{a}_n(\mathbf{x})\mathbf{a}_n^T(\mathbf{x}) = I,$$

the orthotropic anisotropic conductivity tensors can be expressed by

$$\begin{aligned}
D_{I,E}(\mathbf{x}) &= \sigma_l^{I,E}\mathbf{a}_l(\mathbf{x})\mathbf{a}_l^T(\mathbf{x}) + \sigma_t^{I,E}\mathbf{a}_t(\mathbf{x})\mathbf{a}_t^T(\mathbf{x}) + \sigma_n^{I,E}\mathbf{a}_n(\mathbf{x})\mathbf{a}_n^T(\mathbf{x}) \qquad (3.1)\\
&= \sigma_l^{I,E}I + (\sigma_t^{I,E} - \sigma_l^{I,E})\mathbf{a}_t(\mathbf{x})\mathbf{a}_t^T(\mathbf{x}) + (\sigma_n^{I,E} - \sigma_l^{I,E})\mathbf{a}_n(\mathbf{x})\mathbf{a}_n^T(\mathbf{x}),
\end{aligned}$$

and they are symmetric, positive definite and continuous tensors $D_{I,E} : \bar{\Omega} \to \text{Mat}_{3\times 3}(\mathbb{R})$.

For axisymmetric anisotropic media $\sigma_n^{I,E} = \sigma_t^{I,E}$ and (3.1) becomes

$$D_{I,E} = \sigma_t^{I,E}I + (\sigma_t^{I,E} - \sigma_l^{I,E})\mathbf{a}_l(\mathbf{x})\mathbf{a}_l^T(\mathbf{x}). \qquad (3.2)$$

The current densities in both spaces are given by Ohm's law under the quasi-static assumption

$$\mathbf{J}^{I,E} = -D_{I,E}\nabla u_{I,E}.$$

In fact the induction effects are negligible, so the current fields can be defined as the gradient of the potentials.

Denoting by J_m the membrane current per unit volume, we have

$$J_m = \chi I_m = c_m\frac{\partial v_M}{\partial t} + i_{ion}(v_M, w), \qquad (3.3)$$

with $c_m = \chi C_m$, $i_{ion} = \chi I_{ion}$, χ represents the ratio of membrane area per unit of tissue volume while I_{ion} is the ionic current of the membrane per unit area, as

appears in (2.3). Finally, let $I_{app}^{I,E} : \Omega \longrightarrow \mathbb{R}$ be extracellular current stimuli per unit of tissue volume.

Imposing the conservation of currents, that is the interchange between the two media must balance the membrane current flow per unit volume, and exploiting the divergence theorem we have

$$\text{div } \mathbf{J}^I = -J_m + I_{app}^I, \qquad \text{div } \mathbf{J}^E = J_m + I_{app}^E. \tag{3.4}$$

The complete formulation of the Bidomain system coupled with the membrane model is finally

$$c_m \frac{\partial v_M}{\partial t} - \text{div}(D_I \nabla u_I) + i_{ion}(v_M, w) = I_{app}^I \quad \text{in } \Omega \times (0, T) \tag{3.5}$$

$$-c_m \frac{\partial v_M}{\partial t} - \text{div}(D_E \nabla u_E) - i_{ion}(v_M, w) = I_{app}^E \quad \text{in } \Omega \times (0, T) \tag{3.6}$$

$$\frac{\partial w}{\partial t} - R(v_M, w) = 0 \quad \text{in } \Omega \times (0, T) \tag{3.7}$$

where the nonlinear function R describes the dynamics of the gating variables. The initial conditions can be expressed as

$$v_M(\mathbf{x}, 0) = u_I(\mathbf{x}, 0) - u_E(\mathbf{x}, 0) = v_0(\mathbf{x}) \quad \text{in } \Omega \tag{3.8}$$

$$w(\mathbf{x}, 0) = w_0(\mathbf{x}) \quad \text{in } \Omega. \tag{3.9}$$

Supposing that the myocardium is insulated from the surrounding tissue, the homogeneous Neumann boundary conditions are assigned

$$\mathbf{n}^T D_{I,E} \nabla u_{I,E} = 0 \quad \text{on } \partial\Omega \times (0, T). \tag{3.10}$$

Adding the two equations (3.4), we have $\text{div } \mathbf{J}^I + \text{div } \mathbf{J}^E = I_{app}^I + I_{app}^E$. Integrating on Ω and applying Neumann boundary conditions, we have the following compatibility condition for system (3.5)-(3.7) to be solvable

$$\int_\Omega (I_{app}^I + I_{app}^E) \mathrm{d}\mathbf{x} = 0. \tag{3.11}$$

The Bidomain system uniquely determines v_M, while the potentials u_I and u_E are defined only up to a same additive time-dependent constant relating to the reference potential. This potential is chosen to be the average extracellular potential in the cardiac volume by imposing

$$\int_\Omega u_E \mathrm{d}\mathbf{x} = 0. \tag{3.12}$$

The Bidomain model can be equivalently rewritten in terms of the transmembrane and extracellular potentials, yielding a system consisting in a parabolic nonlinear reaction-diffusion partial differential equation (PDE) coupled with an elliptic linear PDE.

$$- \operatorname{div}((D_I + D_E)\nabla u_E) - \operatorname{div}(D_I \nabla v_M) = I_{app}^I + I_{app}^E \quad \text{in } \Omega \times (0,T) \quad (3.13)$$

$$c_m \frac{\partial v_M}{\partial t} + \operatorname{div}(D_E \nabla u_E) + i_{ion}(v_M, w) = -I_{app}^E \quad \text{in } \Omega \times (0,T); \quad (3.14)$$

alternatively

$$c_m \frac{\partial v_M}{\partial t} - \operatorname{div}(D_I(\nabla v_M + \nabla u_E)) + i_{ion}(v_M, w) = I_{app}^I \quad \text{in } \Omega \times (0,T) \quad (3.15)$$

$$- \operatorname{div}((D_I + D_E)\nabla u_E) - \operatorname{div}(D_I \nabla v_M) = I_{app}^I + I_{app}^E \quad \text{in } \Omega \times (0,T) \quad (3.16)$$

We will consider formulation (3.15)-(3.16) in the sequel.

3.2 The Monodomain model

In order to avoid the high computational costs of the full Bidomain model, many large scale simulations have been performed using the so-called Monodomain model. This model is a relaxed Bidomain model described by a system of a parabolic and an elliptic equation, but unlike the Bidomain model, the former evolution equation is fully uncoupled from the elliptic one. An anisotropic Monodomain model consists of a parabolic reaction-diffusion equation for v_M, with conductivity tensor $D_M(\mathbf{x})$ and applied current I_{app}^M, coupled with gating and ionic concentrations system of ODEs and an elliptic problem

$$c_m \frac{\partial v_M}{\partial t} - \operatorname{div}(D_M \nabla v_M) + i_{ion}(v_M, w) = I_{app}^M \quad \text{in } \Omega \times (0,T) \quad (3.17)$$

$$\frac{\partial w}{\partial t} - R(v_M, w) = 0 \quad \text{in } \Omega \times (0,T) \quad (3.18)$$

$$- \operatorname{div}((D_I + D_E)\nabla u_E) - \operatorname{div}(D_I \nabla v_M) = I_{app}^I + I_{app}^E \quad \text{in } \Omega \times (0,T). \quad (3.19)$$

$$(3.20)$$

It is known that if the two media have the same anisotropy ratio, that is $\frac{\sigma_l^E}{\sigma_l^I} = \frac{\sigma_t^E}{\sigma_t^I} = \frac{\sigma_n^E}{\sigma_n^I} = \lambda$, so that $D_E = \lambda D_I$ for a constant λ, then the Bidomain system reduces to the Monodomain one with

$$D_M = \frac{\lambda}{1+\lambda} D_I \qquad I_{app}^M = \frac{1}{1+\lambda}(I_{app}^I - \lambda I_{app}^E). \quad (3.21)$$

This is not a physiological case; in the following we introduce a derivation of Mono-domain model not making the a priori equal anisotropy assumption, as developed in [16, 18].

Denoting by $\mathbf{J}^{tot} = \mathbf{J}^I + \mathbf{J}^E$ the total current flowing in the two media and by $D = D_I + D_E$ the conductivity of the bulk medium; since $\mathbf{J}_{tot} = -D_I \nabla u_I - D_E \nabla u_E$, substituting $u_I = v_M + u_E$, we obtain

$$\nabla u_E = -D^{-1}(D_I \nabla v_M + \mathbf{J}_{tot}). \tag{3.22}$$

Therefore the second equation in the Bidomain system (3.6) can be written as

$$-c_m \frac{\partial v_M}{\partial t} - \operatorname{div}(D_E D^{-1} \nabla) - i_{ion}(v_M, w) = I_{app}^E \quad \text{in } \Omega \times (0, T). \tag{3.23}$$

Since the conductivity tensors are given by (3.1), omitting the dependence on $\mathbf{x}$ of the principal axes, it results

$$\begin{aligned}
D_E D^{-1} &= \mu_l \mathbf{a}_l \mathbf{a}_l^T + \mu_t \mathbf{a}_t \mathbf{a}_t^T + \mu_n \mathbf{a}_n \mathbf{a}_n^T \\
&= \mu_l I + (\mu_t - \mu_l) \mathbf{a}_t \mathbf{a}_t^T + (\mu_n - \mu_l) \mathbf{a}_n \mathbf{a}_n^T,
\end{aligned} \tag{3.24}$$

where $\mu_{l,t,n} := \frac{\sigma_{l,t,n}^E}{\sigma_{l,t,n}^E + \sigma_{l,t,n}^I}$. Taking into account that $\operatorname{div} \mathbf{J}_{tot} = I_{app}^I + I_{app}^E$, we obtain

$$\begin{aligned}
\operatorname{div}(D_E D^{-1} \mathbf{J}_{tot}) &= \mu_l \operatorname{div}(\mathbf{J}_{tot}) + (\mu_t - \mu_l) \operatorname{div}(\mathbf{a}_t \mathbf{a}_t^T \mathbf{J}_{tot}) + (\mu_n - \mu_l) \operatorname{div}(\mathbf{a}_n \mathbf{a}_n^T \mathbf{J}_{tot}) \\
&= \mu_l \operatorname{div}(I_{app}^I + I_{app}^E) + (\mu_t - \mu_l) \operatorname{div}(\mathbf{a}_t \mathbf{a}_t^T \mathbf{J}_{tot}) + (\mu_n - \mu_l) \operatorname{div}(\mathbf{a}_n \mathbf{a}_n^T \mathbf{J}_{tot})
\end{aligned} \tag{3.25}$$

From (3.22) it follows that $-D_E D^{-1} D_I \nabla v_M = D_E \nabla u_E + D_E D^{-1} \mathbf{J}_{tot}$, hence we have the flux relationship

$$\mathbf{n}^T D_E D^{-1} D_I \nabla v_M = \mathbf{n}^T D_E D^{-1} \mathbf{J}_{tot} + \mathbf{n}^T D_E \nabla u_E. \tag{3.26}$$

Using the split form (3.24), the first term on the right hand side can be written as

$$\mathbf{n}^T D_E D^{-1} \mathbf{J}_{tot} = \mu_l \mathbf{n}^T \mathbf{J}_{tot} + (\mu_t - \mu_l)(\mathbf{n}^T \mathbf{a}_t)(\mathbf{a}_t^T \mathbf{J}_{tot}) + (\mu_n - \mu_l)(\mathbf{n}^T \mathbf{a}_n)(\mathbf{a}_n^T \mathbf{J}_{tot}). \tag{3.27}$$

The insulating conditions $\mathbf{n}^T \mathbf{J}^{\mathbf{I}} = \mathbf{n}^T \mathbf{J}^{\mathbf{E}} = 0$ imply that the second term in (3.26) is zero and also that $\mathbf{n}^T \mathbf{J}_{tot} = 0$, i.e. $\mathbf{J}_{tot}$ is tangent to $\partial \Omega$, and assuming that the fibers are tangent too, we have $\mathbf{n}^T \mathbf{a}_n(\mathbf{x}) = \mathbf{a}_t^T(\mathbf{x}) \mathbf{J}_{tot} = 0$ for $\mathbf{x} \in \partial \Omega$; substituting these conditions in (3.26) it holds

$$\mathbf{n}^T D_E D^{-1} D_I \nabla v_M = 0 \quad \text{on } \partial \Omega. \tag{3.28}$$

Disregarding the two additional source terms in (3.25) related to the projections of $\mathbf{J}_{tot}$ on the directions across the fibers, i.e. a_t and a_n, it results in $\mathrm{div}(D_E D^{-1} \mathbf{J}_{tot}) \approx \mu_l(I_{app}^I + I_{app}^E)$. Substituting this approximation into (3.23) and considering the boundary condition (3.28), we obtain (3.17) with the conductivity tensor $D_M := D_E D^{-1} D_I$ and $I_{app}^M = \frac{\sigma_l^E I_{app}^I - \sigma_l^I I_{app}^E}{\sigma_l^E + \sigma_l^I}$. We remark that the conductivity coefficients of D_M are the harmonic means of $\sigma_{l,t,n}^{I,E}$.

The Bidomain model is particularly useful when analyzing the mechanisms by which an electric field interacts with cardiac tissue. One such mechanism is fiber curvature. If the direction of the myocardial fibers varies throughout the tissue, then an electric field will cause a transmembrane potential distribution: both depolarization and hyperpolarization (sometimes called a virtual cathode and virtual anode) [20]. This mechanism only operates if the tissue has unequal anisotropy ratios.

3.3   Variational formulations

In this section, we describe the variational formulation of both the Bidomain and Monodomain models, providing some references to their theoretical analysis. Firstly, we assume that the cardiac region Ω is a bounded Lipschitz connected domain in $\mathbb{R}^d$, with $d = 3, 2$, and that the symmetric and continuous conductivity tensors $D_{I,E} : \bar{\Omega} \longrightarrow \mathrm{Mat}_{d \times d}(\mathbb{R})$ satisfy also the following uniform ellipticity and continuity condition

$$\exists\, \alpha_{I,E} > 0: \quad \xi^T D_{I,E}(\mathbf{x})\xi \geq \alpha_{I,E}|\xi|^2 \qquad \forall \xi \in \mathbb{R}^d, \forall \mathbf{x} \in \Omega. \tag{3.29}$$

$$\exists\, C_{I,E} > 0 \quad C_{I,E} = \sup_{\mathbf{x} \in \Omega} \sup_{\xi \in \mathbb{R}^d} \frac{|D_{I,E}(\mathbf{x})\xi|}{|\xi|} \tag{3.30}$$

Denote by V the Sobolev space

$$\widetilde{H} := H^1(\Omega)/\mathbb{R} = \{w \in H^1(\Omega) \,:\, \int_\Omega w = 0\},$$

and $(\varphi, \psi) := \int_\Omega \varphi\psi$ the usual $L^2(\Omega)$ inner product.
We define the following bilinear forms

$$a_{I,E}(\varphi, \psi) \quad := \quad \int_\Omega (\nabla\varphi)^T D_{I,E}(\mathbf{x})\nabla\psi \mathrm{d}\mathbf{x} \quad \forall \varphi,\, \psi \in H^1(\Omega), \tag{3.31}$$

$$a(\varphi, \psi) \quad := \quad \int_\Omega (\nabla\varphi)^T (D_I + D_E)(\mathbf{x})\nabla\psi \mathrm{d}\mathbf{x} \quad \forall \varphi,\, \psi \in H^1(\Omega). \tag{3.32}$$

For the properties of the conductivity tensor product and (3.30), they are obviously symmetric and continuous, in fact

$$
\begin{aligned}
a_{I,E}(\varphi, \psi) &= \int_\Omega (\nabla\varphi)^T D_{I,E}(\mathbf{x})\nabla\psi \mathrm{d}\mathbf{x} \\
&\leq \max\{C_I, C_E\}|\varphi|_1|\psi|_1 \\
&\leq \max\{C_I, C_E\}\|\varphi\|_{H^1(\Omega)}\|\psi\|_{H^1(\Omega)},
\end{aligned}
$$

denoting by $|\cdot|_1$ the $H^1(\Omega)$ seminorm. Moreover we define $\alpha = \min\{\alpha_I, \alpha_E\}$ and c the Poincaré constant, thanks to (3.29) and the Poincaré-Friedrichs inequality for all $\varphi \in V$ holds

$$
\begin{aligned}
a_{I,E}(\varphi, \varphi) &= \int_\Omega (\nabla\varphi)^T D_{I,E}(\mathbf{x})\nabla\varphi \mathrm{d}\mathbf{x} \\
&\geq \alpha|\varphi|_1^2 \geq \min\{\frac{\alpha}{2c}, \frac{\alpha}{2}\}\|\varphi\|_{H^1(\Omega)}^2,
\end{aligned}
$$

if ψ is constant, $a_{I,E}(\varphi, \psi) = 0$ for every $\varphi \in H^1(\Omega)$. Now we are able to formulate the variational problem for the Bidomain system given in (3.13).

Given $v_0 \in L^2(\Omega)$ and $w_0 \in L^2(\Omega)^N$, with N is the number of unknowns in the ODEs system, and $I_{app}^{I,E} \in L^2(\Omega \times (0,T))$ satisfying the compatibility condition: find $u_E \in L^2(0,T;\widetilde{H})$, $v_M \in H^1(0,T;H^1(\Omega))$ and $w \in L^2(0,T;L^2(\Omega)^N)$ such that $\frac{\partial w}{\partial t} \in L^2(0,T;L^2(\Omega)^N)$ so that $\forall t \in (0,T)$

$$
\begin{cases}
c_m\frac{\partial}{\partial t}(v_M, \varphi) + a_I(v_M + u_E, \varphi) + (i_{ion}(v_M, w), \varphi) &= (I_{app}^I, \varphi) \ \forall\varphi \in H^1(\Omega) \\
a_I(v_M, \varphi) + a(u_E, \varphi) &= 0 \quad \forall\varphi \in H^1(\Omega) \\
\frac{\partial}{\partial t}(w, \psi) - (R(v_M, w), \psi) &= 0 \qquad \forall\psi \in L^2(\Omega) \\
(v_M(0), \varphi) &= (v_0, \varphi) \quad \forall\varphi \in H^1(\Omega) \\
(w(0), \psi) &= (w_0, \psi) \ \forall\psi \in L^2(\Omega).
\end{cases}
$$

We remark that the equations $(v_M(0), \varphi) = (v_0, \varphi) \ \forall\varphi \in H^1(\Omega)$ and $(w(0), \psi) = (w_0, \psi) \ \forall\psi \in L^2(\Omega)$ are equivalent to $v_M(\mathbf{x}, 0) = v_0(\mathbf{x})$ and $w(\mathbf{x}0) = w_0(\mathbf{x})$ a.e..

Analogously the variational formulation of the Monodomain model (3.18) reads as follows.

Given $v_0 \in L^2(\Omega)$ and $w_0 \in L^2(\Omega)^N$, with N the number of unknowns in the ODEs system, and $I_{app} \in L^2(\Omega \times (0,T))$ satisfying the compatibility condition: find $v_M \in H^1(0,T;H^1(\Omega))$ and $w \in L^2(0,T;L^2(\Omega)^N)$ such that $\frac{\partial w}{\partial t} \in L^2(0,T;L^2(\Omega)^N)$

so that $\forall t \in (0, T)$

$$
\begin{cases}
c_m \frac{\partial}{\partial t}(v_M, \varphi) + a(v_M, \varphi) + (i_{ion}(v_M, w), \varphi) &= (I_{app}, \varphi) \ \forall \varphi \in H^1(\Omega) \\
\frac{\partial}{\partial t}(w, \psi) - (R(v_M, w), \psi) &= 0 \qquad \forall \psi \in L^2(\Omega) \\
(v_M(0), \varphi) &= (v_0, \varphi) \quad \forall \varphi \in H^1(\Omega) \\
(w(0), \psi) &= (w_0, \psi) \ \forall \psi \in L^2(\Omega).
\end{cases}
$$

Under a suitable choice of the ionic model and regularity assumptions on the domain, Ω at least of class $\mathcal{C}^{1,1}$, on the conductivity coefficients, $D_{I,E}$ Lipschitz in Ω, and on the initial data, it is possible to prove the well-posedness of the Bidomain model. In this respect, the first work was by Colli Franzone and Savaré in 2002 [22], if the Bidomain system is coupled with a membrane model such as the cubic-like FitzHugh-Nagumo [42, Chapter 5], then extended in 2009 by Veneroni [81] to more general and realistic models, taking the form of the Luo-Rudy I model. In the same year, Bourgault et al. [12] verified the existence and uniqueness of a global solution for the coupling of the Bidomain system with FitzHugh-Nagumo, Aliev-Panfilov [1] and MacCulloch [65] models.

Chapter 4

Basics of Isogeometric Analysis

Isogeometric Analysis (IGA) is a method for discretization of partial differential equations, introduced in [39], with the aim of bridging the gap between computer-aided design (CAD) and the finite element method (FEM), determined by the need of generating a computational mesh. In fact, the geometrical representation provided by CAD technology need to be modified in order to obtain geometries compatible with the FEM discretization. IGA is based on a unique geometrical representation under the *isoparametric paradigm*, adopting the same spline or Non-uniform rational B-spline (NURBS) basis function used to design domain geometries in CAD to construct both trial and test spaces in the discrete variational formulation of differential problems.

In this work we consider only NURBS-based IGA, not only because NURBS are a standard tool in CAD but also for their mathematical properties. In particular NURBS can exactly represent some common geometries, e.g. conic sections provide globally smooth basis functions, and offer new refinements possibilities beside $h-$ and $p-$ refinements. However, other computational geometry technologies could be adopted to represent the geometries, recently improvements have been done in the direction of IGA based on *T-splines* [68, 7], a generalization of NURBS.

This chapter is devoted to the introduction of the univariate and multivariate B-spline basis functions and related spaces, the NURBS basis function, function space, and the NURBS geometrical map **F**. We consider the case of geometries that can be modelled as a single *patch*, i.e. a domain topologically representable by a geometrical mapping of a hypercube reference domain.

A more complete presentation can be found in [23].

4.1 B-splines

NURBS are a standard tool for describing and modelling curves and surfaces in CAD. They are built from B-splines and therefore a discussion of B-splines is a natural starting point for their study.

4.1.1 Univariate B-splines

Univariate B-splines are piecewise polynomial curves composed of linear combinations of B-splines basis functions; the coefficients are points in the space referred to as *control points.*

In order to define B-spline basis functions, we introduce the *knot vector*, a set of non-decreasing real numbers

$$\Xi = \{0 = \xi_1, \xi_2, ..., \xi_{n+p+1} = 1\},$$

where p is the order of the B-spline and n is the number of basis functions (and control points) necessary to describe it. A knot vector represents coordinates in the one dimensional parametric space interval $[0,1]$, referred also as a *patch*, while (ξ_i, ξ_{i+1}) is referred as the *knot span*. If knots are equally-spaced in the parametric space, they are said to be uniform. Knot values may be repeated, the number of times a knot is repeated is indicated as the multiplicity of the knot. The multiplicity of knot values important implications for the property of the basis, in particular for the regularity. We assume that Ξ is an open knot vector, i.e., the first and the last $p+1$ knots are repeated.

Given a knot vector B-spline basis functions are defined recursively starting with piecewise constant $(p = 0)$

$$B_i^0(\xi) = \begin{cases} 1 & \text{if} \quad \xi_i \leq \xi < \xi_{i+1} \\ 0 & \text{otherwise} \end{cases} \tag{4.1}$$

$$B_i^p(\xi) = \frac{\xi - \xi_i}{\xi_{i+p} - \xi_i} B_i^{p-1}(\xi) + \frac{\xi_{i+p+1} - \xi}{\xi_{i+p+1} - \xi_{i+1}} B_i^{p-1}(\xi). \tag{4.2}$$

This is known as the Cox-de Boor recursion formula. When there are repeated knots, some of the denominators in (4.2) may be zero. We then adopt the convention that 0/0=0 and $(c/0) \cdot 0 = 0$. Since B_i^p will be identically zero when $\xi_{i+p} = \xi_i$, this means that any term with the denominator equal to zero may be ignored.

Important properties of B-spline basis functions are:

1. They constitute a *partition of unity*, that is for all $\xi \in \widehat{\Omega}$

$$\sum_{i=1}^{n} B_i^p(\xi) = 1. \tag{4.3}$$

2. Each function is non-negative, i.e., $B_i^p(\xi) \geq 0 \ \forall \xi \in [0, 1]$.

3. The general basis function B_i^p has the support in $p + 1$ knot spans

$$\mathrm{supp}(B_i^p) \subseteq [\xi_i, \xi_{i+p+1}]; \tag{4.4}$$

   moreover, at most $p + 1$ basis functions have support in each knot span.

4. If a knot has multiplicity m, with $1 \leq m \leq p + 1$, then the B-spline basis functions have $p - m$ continuous derivatives at that knot. $p - m = -1$ is allowed and stands for a discontinuity.

If a knot is repeated p times, the $\mathcal{C}^0$ basis is interpolatory. In particular basis functions formed from an open knot vector are interpolatory and discontinuous at the end of the parametric domain, and at the corner of the patch, in more than one dimension, defining the patch boundary. A further consequence of the use of open knot vectors in multiple dimensions, is that the boundary of a B-spline object with r parametric dimensions is itself a B-spline object of dimension $r - 1$. An example of quadratic B-spline basis in one dimension, derived from the knot vector $\Xi = \{0, 0, 0, 0.2, 0.4, 0.6, 0.8, 0.8, 1, 1, 1\}$, is shown in Fig. 4.1. Since it is an open knot vector the first and last basis functions are interpolatory, while the continuity at interior knots ξ_i is $\mathcal{C}^1$, except for the repeated knot 0.8 where the continuity is $\mathcal{C}^0$.

The space of splines is denoted by

$$\widehat{\mathcal{S}} \equiv \widehat{\mathcal{S}}(\Xi, p) := \mathrm{span}\{B_i^p, \quad i = 1...n\}. \tag{4.5}$$

4.1.2 Multivariate B-splines

Let $\widehat{\Omega} = (0, 1)^r$ be an open parametric domain referred as a patch. For any α, $1 \leq \alpha \leq d$, we define the following d knot vectors

$$\Xi_\alpha = \{0 = \xi_{1,\alpha}, \xi_{2,\alpha}, ..., \xi_{n_\alpha+p_\alpha+1,\alpha} = 1\};$$
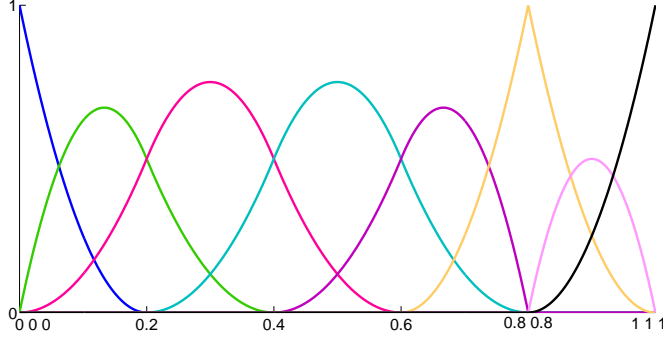
Figure 4.1: Quadratic (p=2) basis function for the open, non-uniform knot vector $\Xi = \{0, 0, 0, 0.2,\ 0.4,\ 0.6,\ 0.8,\ 0.8,\ 1,\ 1,\ 1\}$.

associated with them, there is a mesh $\mathcal{Q}$, that is, a partition of the patch into r-dimensional open knot spans, or elements

$$\mathcal{Q} \equiv \mathcal{Q}(\Xi_1, ..., \Xi_r) := \{Q = \otimes_{\alpha=1}^{r}(\xi_{i_\alpha,\alpha}, \xi_{i_\alpha+1,\alpha}) | Q \neq \emptyset \quad p_\alpha + 1 \leq i_\alpha \leq n_\alpha - 1\}. \tag{4.6}$$

Having set the element size to $h_Q := \mathrm{diam}(Q)$ for all $Q \in \mathcal{Q}$, we define the *mesh size h* as

$$h := \max\{h_Q \,:\, Q \in \mathcal{Q}\}. \tag{4.7}$$

The multivariate B-spline basis functions are defined by tensor product as

$$B_{i_1,...,i_r}^{p_1,...,p_r} := \otimes_{\alpha=1}^{d} B_{i_\alpha,\alpha}^{p_\alpha}. \tag{4.8}$$

Thanks to the tensor product structure, several properties satisfied by the univariate B-spline basis functions still hold for the multivariate case. In particular, the basis functions are piecewise polynomials, pointwise non-negative and constitute a partition of unity. As for their supports, they are the tensor product of the relative univariate supports, being still compact. For what concerns the regularity, in all the elements $Q \in \mathcal{Q}$ the basis functions are $\mathcal{C}^\infty-$continuous, while across each internal $d - 1$ dimensional face it reaches a regularity of the order equals to the maximum order of continuity of the derivatives across this face.

The tensor product spline space is

$$\widehat{\mathcal{S}} \equiv \mathcal{S}(\Xi_1, ..., \Xi_d, p_1, ..., p_r) := \mathrm{span}\{B_{i_1,...,i_r}^{p_1,...,p_r}, \quad i_\alpha = 1...n_\alpha,\ \alpha = 1,.., r\}. \tag{4.9}$$

For the sake of notation, we denote the degree as $\mathbf{p}$, underlying $\mathbf{p} = (p_1, ..., p_r)$, and we introduce the multi-index $\mathbf{i} = (i_1, ..., i_r)$ that belongs to the set

$$\mathcal{I} := \{\mathbf{i} = (i_1, ..., i_r) \,:\, 1 \leq i_\alpha \leq n_\alpha, 1 \leq \alpha leq r\}. \tag{4.10}$$

4.1.3   B-spline geometries

B-spline curves in $\mathbb{R}^d$ are built by taking a linear combination of univariate B-spline basis functions. The vector-valued coefficients of the basis functions are called *control points* and piecewise linear interpolation of these points gives the *control polygon*. These are analogous to nodal coordinates in finite element analysis in the fact they are the coefficients of the basis functions, but the non-interpolatory nature of the basis does not lead to a concrete interpretation of the control point values. Thus, given the univariate basis $\{B_i^p\}_{i=1}^n$ over the parametric domain $\widehat{\Omega}$ and $C_i \in \mathbb{R}^d$ corresponding control points, a piecewise polynomial B-spline curve is given by

$$C : \widehat{\Omega} \to \Omega \subset \mathbb{R}^d, \qquad C(\xi) = \sum_{i=1}^n C_i B_i^p. \tag{4.11}$$

We can identify several properties of the B-spline curve from the definition, others, concerning regularity and locality, follow from the properties of B-spline basis functions.

- B-spline curves of degree p have continuous derivatives of order $p-1$ in case of non-repeated knots or control points, repeating a knot or control point k times decreases the number of continuous derivatives by k;

- *Locality*: due to the compact support of the B-spline basis functions, moving a single control point can affect the geometry of no more than p+1 elements of the curve;

- *Convex hull property*: a B-spline curve is completely contained within the convex hull defined by its control points. For a curve of degree p, we define the convex hull as the union of all of the convex hulls formed by $p + 1$ successive control points.

- *Affine covariance*: an affine transformation of a B-spline curve is obtained by applying the transformation directly to the control points.

- Variation diminishing property: there is no plane having more intersection with the B-spline curve than it has with the control polygon.

By exploiting the tensor product nature of the multivariate B-spline basis functions, it is possible to define geometrical entities in the physical space $\mathbb{R}^d$ of dimension r, with $1 \leq r \leq d$.

Given r knot vectors $\Xi_\alpha = \{0 = \xi_{1,\alpha}, \xi_{2,\alpha}, ..., \xi_{n_\alpha+p_\alpha+1,\alpha} = 1\}$ for $\alpha = 1, ..., r$, we consider the associated multivariate B-spline basis $\{B_{\mathbf{i}}^{\mathbf{p}}\}$ and a set of $\prod n_\alpha$ control points $\{\mathbf{C_i}\}$. A $r-$dimensional B-spline entity in $\mathbb{R}^d$ is defined by the *geometrical map*

$$\mathbf{F} : \widehat{\Omega} \to \Omega \subset \mathbb{R}^d \qquad \mathbf{F}(\xi) = \sum_{\mathbf{i} \in \mathcal{I}} \mathbf{C_i} B_{\mathbf{i}}^{\mathbf{p}}. \tag{4.12}$$

We remark that the locality and regularity properties still hold, as well the affine covariance and the convex hull ones. The elements in the physical domain are obtained from (4.12) as the image of the elements in $\widehat{\Omega}$, so we can define the *physical mesh* in Ω

$$\mathcal{K} := \{K = \mathbf{F}(Q)|\, Q \in \mathcal{Q}\}. \tag{4.13}$$

4.2 Non-Uniform Rational B-Splines

A NURBS in $\mathbb{R}^d$ is the projective transformation of a B-spline in $\mathbb{R}^{d+1}$, it offers great flexibility and precision for handling both analytic and modelled shapes; in fact NURBS are commonly use in CAD. A more complete treatment can be found in a standard textbook such as [31].

4.2.1 NURBS basis functions

Starting from a knot vector $\Xi = \{0 = \xi_1, ..., \xi_{p+n+1} = 1\}$, we associate to the corresponding B-spline basis function $\{B_i^p\}_1^n$ a set of strictly positive real numbers $\{\omega_i\}_1^n$, called *weights*. We then introduce a piecewise polynomial function, called *weighting function*, as

$$\omega : \widehat{\Omega} \to \mathbb{R} \qquad \omega(\xi) := \sum_{i=1}^{n} \omega_i B_i^p. \tag{4.14}$$

The univariate NURBS basis functions $\{R_i\}_{i=1}^n$ are defined as

$$R_i : \widehat{\Omega} \to \mathbb{R} \qquad R_i(\xi) := \frac{\omega_i B_i(\xi)}{\omega(\xi)}. \tag{4.15}$$

Each basis function is a piecewise rational function defined in the parametric domain $\widehat{\Omega}$. It is a convention to refer to the *degree* of the NURBS basis function as to the degree of the associated B-spline basis $\{B_i^p\}_{i=1}^n$.

As the NURBS functions are constructed from the B-spline basis, they inherit most of the B-spline basis functions properties. In fact, at each knot with m

multiplicity they are $\mathcal{C}^{p-m}$ continuous, moreover, if we consider an open knot vector then the first and the last NURBS basis functions are interpolatory at the extrema of the parametric interval. The basis $\{R_i\}_{i=1}^n$ still constitutes a partition of unity; each basis function is everywhere pointwise non-negative and has compact support in $p+1$ knot spans, i.e. $\text{supp}(R_i^p) \subseteq [\xi_i, \xi_{i+p+1}]$, and at most $p+1$ basis functions are non-zero on each knot span.

The univariate NURBS space on the parametric domain $\widehat{\Omega} = [0, 1]$ is denoted as

$$\widehat{\mathcal{N}} \equiv \widehat{\mathcal{N}}(\Xi, p) := \text{span}\{R_i^p, \quad i = 1...n\}. \tag{4.16}$$

Similarly, we can define multivariate NURBS basis functions and related NURBS space. Given an integer r, we consider r a knot vectors Ξ_α, with $\alpha = 1,...,r$, and the associated multivariate B-spline basis $\{B_{\mathbf{i}}^p\}_{\mathbf{i}\in\mathcal{I}}$. Assigned a set of weights $\{\omega_{\mathbf{i}}\}_{\mathbf{i}\in\mathcal{I}}$, we also define the weighting function over the parametric domain $\widehat{\Omega} = [0, 1]^r$ as

$$\omega : \widehat{\Omega} \to \mathbb{R} \qquad \omega := \sum_{\mathbf{i}\in\mathcal{I}} \omega_{\mathbf{i}} B_{\mathbf{i}}, \tag{4.17}$$

which is positive and is smooth on each element, along with its reciprocal. This lead to the definition of the NURBS basis functions $\{R_{\mathbf{i}}\}$

$$R_{\mathbf{i}} : \widehat{\Omega} \to \mathbb{R} \qquad R_{\mathbf{i}}(\xi) := \frac{\omega_{\mathbf{i}} B_{\mathbf{i}}(\xi)}{\omega(xi)}. \tag{4.18}$$

whose properties can be deduced from those of the multivariate B-splines. Finally, the NURBS space over the patch is

$$\widehat{\mathcal{N}} \equiv \mathcal{N}(\Xi_1, ..., \Xi_r, \mathbf{p}) := \text{span}\{R_{\mathbf{i}}, \quad \mathbf{i} \in \mathcal{I}\}. \tag{4.19}$$

4.2.2 NURBS geometries

NURBS entities can be described from both a geometric and an algebraic point of view. From a geometrical perspective, a NURBS geometry in $\mathbb{R}^d$ is obtained by the projective transformation of a B-spline entity in $\mathbb{R}^{d+1}$ onto a hypersuperface in R^d. The resulting object corresponds with the physical domain $\Omega \subset \mathbb{R}^d$.

Given a B-spline curve C^ω, as (4.11), called *projective curve* defined through the univariate B-spline basis $\{B_i^p\}_{i=1}^n$ and the control points $\{\mathbf{C}_i^\omega\}_{i=1}^n \subset \mathbb{R}^{d+1}$ (we assume that the $d+1^{th}$ coordinate of each point is positive), called *projective control points* the projection of C^ω onto the hyperplane $\{(x_1, ..., x_{d+1}) \in \mathbb{R}^{d+1} | x_{d+1} = 1\}$ is a rational function defined as NURBS curve in $\mathbb{R}^d$. We obtain the control points,
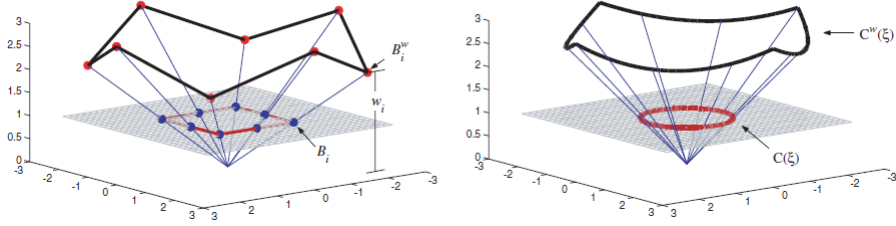
Figure 4.2: Circle in $\mathbb{R}^2$ constructed by projective transformation of piecewise quadratic B-spline in $\mathbb{R}^2$, see [23]. (left) Projective transformation of projective control points yields control points. (right) Projective transformation of B-spline curve yields NURBS curve.

$\{\mathbf{C}_i\}_{i=1}^n$, of the NURBS curve by performing the same transformation to the projective control points

$$(\mathbf{C}_i)_j := \frac{(\mathbf{C}_i^\omega)_j}{\omega_i}, \quad \text{for } j = 1...d, \qquad \text{with} \quad \omega_i := (\mathbf{C}_i^\omega)_{d+1}, \qquad (4.20)$$

where $(\mathbf{C}_i)_j$ is the j-th component of the vector $\mathbf{C}_i$ and ω_i is referred to as the i-th weight. Given the weights, we have the weighting function ω (4.17) and we can compute the NURBS curve $\mathbf{C}$ component-wise by

$$\mathbf{C} : \widehat{\Omega} \to \mathbb{R} \qquad (C(\xi))_j = \frac{(C^\omega(\xi))_j}{\omega(\xi)}, \quad \text{for } j = 1...d. \qquad (4.21)$$

In particular, conic section can be exactly represented by the projective transformation of a piecewise quadratic B-spline, as illustrated in Fig. 4.2, where a circle in $\mathbb{R}^2$ is obtained by the projection of a piecewise quadratic curve in $\mathbb{R}^3$. From Fig. 4.2, we remark that the B-spline curve clearly has four points of only $\mathcal{C}^0$-continuity. This means that the knot values at these locations have multiplicities of two, nevertheless the circle itself has no obvious points of reduced continuity. Frequently, the maximum level of continuity is restricted by the shape of the projective curve rather than the curve itself, see [23].

An algebraic point of view allows to construct NURBS entities and spaces, ignoring the projective geometry, by means a set of control points and NURBS basis functions introduced in Sec. 4.2.1. Given multivariate NURBS basis functions $\{R_{\mathbf{i}}^{\mathbf{p}}\}_{\mathbf{i} \in \mathcal{I}}$ defined in $\widehat{\Omega} = [0, 1]^r$ and a set of control points $\{\mathbf{C}_{\mathbf{i}}\}_{\mathbf{i} \in \mathcal{I}} \subset \mathbb{R}^d$, a r-dimensional NURBS geometry in $\mathbb{R}^d$ is represented by the *geometrical map*

$$\mathbf{F} : \widehat{\Omega} \to \Omega \subset \mathbb{R}^d \qquad \mathbf{F}(\xi) = \sum_{\mathbf{i} \in \mathcal{I}} \mathbf{C}_{\mathbf{i}} R_{\mathbf{i}}^{\mathbf{p}}. \qquad (4.22)$$

The properties of NURBS geometries derive from the ones of the NURBS basis functions. In particular, the regularity and locality properties still hold, as well as the affine covariance, convex hull and variation diminishing properties.

Hereafter we consider the case $r = d$, that is the dimension of the parametric space is the same of the physical domain.

The NURBS geometrical map $\mathbf{F}$ is the parametrization of the physical domain Ω. We assume that $\mathbf{F}$ is invertible with smooth inverse on each element of the physical mesh $K \in \mathcal{K}$, (4.13).

Finally the space $\mathcal{V}$ of NURBS on Ω is defined as the push-forward of the NURBS space $\mathcal{N}$ on the patch,

$$\mathcal{V} := \text{span}\{R_{\mathbf{i}}^{\mathbf{p}} \circ \mathbf{F}^{-1}, \ \mathbf{i} \in \mathcal{I}\}. \tag{4.23}$$

4.3 Refinements

One of the most interesting aspects of B-splines and NURBS spaces is the way the basis may be enriched while leaving the underlying geometry and its parametrization intact. We recall the refinement procedures that can be performed within B-splines and NURBS framework. In particular, two kind of refinement, *knot insertion* (or *h-refinement*) and *degree elevation* (or *p-refinement*), are affine with those used in FEM. However there is a third choice, referred as *k-refinement*, peculiar to the B-spline and NURBS basis. We briefly recall these procedure for univariate B-spline basis. For detailed description, we refer to [23].

Knot insertion

Knot insertion is the analogue of *h*-refinement in finite element method. The main point here is that knots can be inserted without changing a curve geometrically or parametrically. Given a knot vector $\Xi = \{\xi_1, ..., \xi_{n+p+1}\}$, we consider a knot to be inserted in Ξ,
$bar\xi \in [\xi_k, \xi_{k+1})$. By applying the recursive formula (4.2) to the *extended* knot vector $\bar{\bar{\Xi}} = \{\xi_1, ...\xi_k, ..., \bar{\xi}, \xi_{k+1}, ..., \xi_{n+p+1}\}$, a new set of $n + 1$ basis functions is obtained. The new control points $\{\bar{\mathbf{C}}_i\}_{i=1}^{n+1}$ are constructed from linear combination of the original control points $\{\mathbf{C}_i\}_{i=1}^{n}$ by

$$\bar{\mathbf{C}}_i = \alpha_i \mathbf{C}_i + (1 - \alpha_i)\mathbf{C}_{i-1}, \tag{4.24}$$

where

$$
\alpha_i = \begin{cases}
1 & 1 \leq i \leq k - p, \\
\dfrac{\bar{\xi} - \xi_i}{\xi_{i+p} - \xi_i} & k - p + 1 \leq i \leq k, \\
0 & 1 + 1 \leq i \leq n + p + 2.
\end{cases}
\tag{4.25}
$$

Knot values already present in the knot vector may be repeated in this way, thereby increasing their multiplicity, but the continuity of the basis will be reduced. However, continuity of the curve is preserved by choosing the control points as in (4.24) and (4.25).

In practical applications, the geometry of the physical domain Ω is frequently described on a mesh of relatively few elements, while the computation of an approximate solution to the problem is performed on a refined mesh (in order to achieve desired accuracy). Therefore, it is possible to fix the description of the geometry at a coarse mesh, this means that the weighting function ω (4.17) and the geometrical map $\mathbf{F}$ are assigned on coarse spaces, and are the same for every h. When the mesh and the spaces are refined the weights are selected so that w stays fixed in a similar way, the control points are adjusted such that F remains unchanged. Thus the geometry and its parametrization are held fixed in the refinement process. See Fig.4.3 for an illustration of this idea.

Degree elevation

Analogously to p-refinement in FEM, we can elevate the polynomial degree of the basis functions; we refer to this process as degree elevation or p-refinement. As for knot insertion, it is performed in such a manner that both the parametrization and the geometry of the original curve are preserved. Since we want to preserve also the regularity of the basis in the whole domain, it follows that, when performing a degree elevation, the multiplicity of each existing knot has to be increased by one, without inserting any additional knots. The implementation of this kind of refinement is, in general, less straightforward than knot insertion. We refer to [64] for suitable algorithms.

k-refinement

The fact that order elevation and knot insertion procedures do not commute, introduces the possibility of a new refinement strategy, called *k-refinement*, which has not analogue in FEM, see [23]. Let us consider a B-Splines basis of degree p.
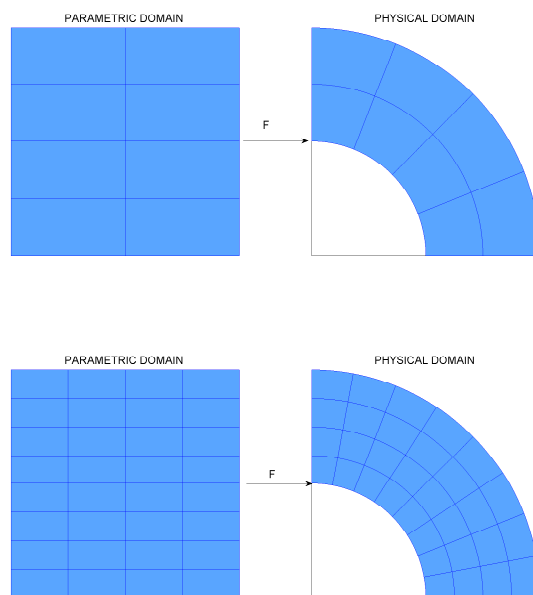
Figure 4.3: $h-$refinement with NURBS.

If a knot insertion is performed, when adding a new knot $\bar{\xi}$, the basis functions in this knot are $\mathcal{C}^{p-1}$-continuous. This regularity in $\bar{\xi}$ is preserved if we subsequently elevate the degree to $q \geq p$ with the multiplicity of each knot, including $\bar{\xi}$, increased accordingly. On the other hand, we can first perform order elevation, until the polynomial degree is q and then insert a new knot value $\bar{\xi}$. In this case the number of non-zero knot spans is still the same as before, but the basis functions are now $\mathcal{C}^{q-1}$-continuous in $\bar{\xi}$, instead of only $\mathcal{C}^{p-1}$-continuous, the regularity attained according to the previous procedure. The latter procedure is referred to as *k-refinement*.

4.4 Approximation properties

In this section we provide some approximation results of B-splines and NURBS, reported in [6], focusing only on the issues necessary for our subsequent analysis of Schwarz preconditioners, see Chapter 6. We firstly need to recall some results concerning the interpolation theory of NURBS. The interpolation result is based on the introduction of a support extension $\widetilde{Q}$ of an element Q in the mesh $\mathcal{Q}$ over the parametric domain, as the union of the supports of basis functions whose

support intersect the element itself. This last induces naturally the definition of a physical support extension of an element K of the physical mesh $\mathcal{K}$, as the image of the support extension of Q through $\mathbf{F}$, i.e. if $K = \mathbf{F}(Q)$ then $\widetilde{K} := \mathbf{F}(\widetilde{Q})$. We consider *shape regular* mesh, i.e., the ratio between the smallest edge of $Q \in \mathcal{Q}$ and its diameter h_Q is bounded, uniformly with respect to Q and h, recall that h is the global mesh size (4.7). This implies that the mesh is locally quasi-uniform the ratio of the sizes of two neighbouring elements is uniformly bounded. Moreover, in order to take into account the regularity across the common $(d-1)$-dimensional face between two adjacent elements Q_1 and Q_2, the [6] the authors define the so called *bent Sobolev spaces* of order $m \in \mathbb{N}$ denoted by $\mathcal{H}^m$

Let denote by $\widehat{\Pi}$ the standard projector on the spline space, introduced in [67, Chapter 12], defined as

$$\widehat{\Pi} v := \sum_{i_1=1,\dots,i_d=1}^{n_1\dots n_d} (\lambda_{i_1\dots i_d} v) B_{i_1\dots i_d} \quad \forall v \in [L^2(0,1)]^d, \tag{4.26}$$

where the $\lambda_{i_1\dots i_d}$ are dual basis functional, that is

$$\lambda_{j_1\dots j_d} B_{i_1\dots i_d} = 1 \qquad \text{if } j_\alpha = i_\alpha \quad \forall 1 \le \alpha \le d$$
$$= 0 \qquad \text{otherwise.}$$

The properties of this operator can be summarized in the following lemmas, proved in [67] and [6], respectively.

Lemma 1. *We have*

$$\widehat{\Pi} s = s \qquad \forall s \in \widehat{\mathcal{S}} \tag{4.27}$$

$$\| \widehat{\Pi} v \|_{L^2(Q)} \le \| v \|_{L^2(\widetilde{Q})} \qquad \forall v \in L^2((0,1)^d \text{ and } \forall Q \in \mathcal{Q}. \tag{4.28}$$

Lemma 2. *Given the operator $\widehat{\Pi}$ defined in (4.26) and $0 \le k \le l \le p+1$; then for all $Q \in \mathcal{Q}$*

$$|v - \widehat{\Pi} v|_{H^k(Q)} \le C h_Q^{l-k} |v|_{\mathcal{H}^l(\widetilde{Q})}, \qquad \forall v \in \mathcal{H}^l(\widetilde{Q} \cap L^2((0,1)^d). \tag{4.29}$$

The following lemma gives estimates for the change of variable from the patch to the physical domain

Lemma 3. *Let m be a non-negative integer, $Q \in \mathcal{Q}$ and $K = \mathbf{F}(Q)$. For all*

$v \in H^m(K)$ *it holds that*

$$|v \circ \mathbf{F}|_{H^m(Q)} \leq C||\det D\mathbf{F}^{-1}||_{L^\infty(K)}^{1/2} \sum_{j=0}^{m} ||D\mathbf{F}||_{L^\infty(Q)}^{j} |v|_{H^j(K)} \tag{4.30}$$

$$|v|_{H^m(K)} \leq C||\det D\mathbf{F}||_{L^\infty(K)}^{1/2} ||D\mathbf{F}||_{L^\infty(Q)}^{-m} \sum_{j=0}^{m} |v \circ \mathbf{F}|_{H^j(Q)} \tag{4.31}$$

$$\tag{4.32}$$

where C is a constant that depends on the weighting function and its reciprocal on $\widetilde{Q}$ and uniformly bounded with respect to the mesh size.

Chapter 5

The discrete Bidomain system

5.1 Spatial discretization

Various spatial discretization techniques have been applied to the cardiac bidomain problem, most notably finite difference methods (FDM) [72], finite volume methods (FVM) [34] and finite element methods (FEM) [17]. In general, FDM are easiest to implement, but the methods do not accommodate complex boundaries as naturally as FEM or FVM do. Both FVM and FEM have been used to model electrical activity in anatomically realistic models of the atria and the ventricles.

The heart is an organ with a complex structure. Obtaining a representation that encompasses the required anatomical and structural details that is also suitable for computational studies can therefore be challenging. Several groups have created detailed geometrical models of the ventricles, which have subsequently been used in finite element computations of cardiac electrophysiology and mechanics. The more detailed models include the contributions from the Auckland group [55, 46, 75]; it has presented models of geometry and fibers orientation for canine and pig ventricles. These models were based on structured grids with cubic Hermite interpolation functions. Geometries represented with Hermite interpolation have $\mathcal{C}^1$ continuity across the interface between adjacent elements because they share nodal variables, including first derivatives. This provides cubic Hermite meshes a smooth representation of shapes with relatively few elements, as desired for the simulation of soft tissue mechanics.

Here we will present an alternative approach, based on isogeometric analysis.

The shape of the left ventricular myocardium can be likened to that of an eggshell with its top cut off: the aortic and mitral valve openings represent the rim (the base) and the wall is thickest at the greatest circumference (the equator)

and thinnest at the bottom (the apex). The use of such a model has been suggested by Streeter and Hanna [78]. Thus, representing the left ventricle as a family of truncated ellipsoid gives a better overall approximation of the geometry. However for small part of ventricle a cartesian slab can also be adopted. In Figure 5.1 these two possible approximations are shown.

(a)
(b)
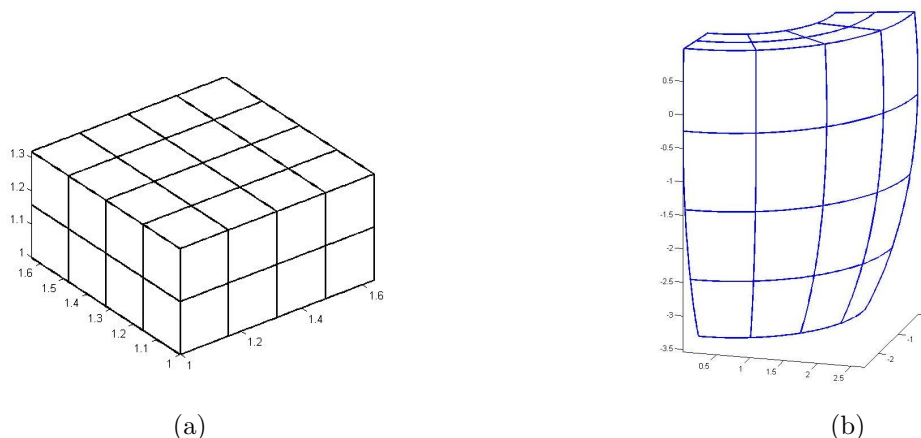
Figure 5.1: a) cartesian slab; b) ellipsoidal domain.

The parametric equations for an ellipsoidal domain are

$$\begin{cases} x = & a(r)\cos(\theta)\cos(\phi) & \phi_{min} \le \phi \le \phi_{max} \\ y = & b(r)\cos(\theta)\sin(\phi) & \theta_{min} \le \theta \le \theta_{max} \\ z = & c(r)\sin(\theta) & 0 \le r \le 1 \end{cases}$$

where $a(r) = a_1 + r(a_2 - a_1)$, $b(r) = b_1 + r(b_2 - b_1)$ and $c(r) = c_1 + r(c_2 - c_1)$, with a_i, b_i, c_i, $i = 1, 2$ given coefficients determining the main axes of the ellipsoid. This representation allow us to control the orientation of the fibers, namely, they rotate intramurally linearly with the depth for a total amount of 120° proceeding, when the point of view is from the epicardial side, counter-clockwise from epicardium to endocardium. More precisely, in a local reference system $\{\mathbf{e}_\phi, \mathbf{e}_\theta, \mathbf{e}_r\}$ at a point $\mathbf{x} \in \Omega$, the fiber direction $\{\mathbf{a}_l$ and the direction normal to the laminae, introduced in Sec. 3.1, are given by

$$\mathbf{a}_l = \mathbf{e}_\phi \cos\alpha(r) + \mathbf{e}_\theta \sin\alpha(r), \qquad \mathbf{a}_n = \mathbf{e}_\phi \sin\alpha(r) - \mathbf{e}_\theta \cos\alpha(r),$$

where α is the rotation angle defined as

$$\alpha(r) = \frac{2}{3}\pi(1 - r) - \frac{\pi}{4}, \qquad 0 \le r \le 1.$$

For a slab of cardiac tissue, described in the usual cartesian coordinate system, the fiber rotation is given by

$$\mathbf{a}_l = \mathbf{e}_x \cos \alpha(r) + \mathbf{e}_y \sin \alpha(r), \quad \mathbf{a}_t = \mathbf{e}_z \quad \mathbf{a}_n = \mathbf{e}_x \sin \alpha(r) - \mathbf{e}_y \cos \alpha(r),$$

with the transmural parameter $r := |z/c|$, denoting by c the thickness of the slab.

We therefore introduce the spline space living in the parametric domain

$$\widehat{V} := \text{span}\{B_{i_1...i_d}^{p_1...p_d}, \ i_\alpha = 1, ..., n_\alpha, 1 \le \alpha \le d\} \tag{5.1}$$

Since the single patch domain Ω is a NURBS region, we need a geometrical map $\mathbf{F} : (0,1)^d \to \Omega$ in order to define the physical space

$$\begin{aligned} V \ &:= \text{span}\{R_{i_1...i_d}^{p_1...p_d} \circ \mathbf{F}^{-1}, i = 1, \dots, i_\alpha = 1, \dots, n_\alpha, 1 \le \alpha \le d\} \\ &= \{\frac{\widehat{v}}{\omega} \circ \mathbf{F}^{-1} \quad \forall \widehat{v} \in \widehat{V}\}. \end{aligned} \tag{5.2}$$

Let us denote by

$$N_h = \dim(\widehat{V}) = \dim(V),$$

the dimension of the spaces, and let $\{\widehat{\varphi}_i\}_{i=1}^{N_h}$ be a basis for $\widehat{V}$. Then due to the assumption on the parametrization $\mathbf{F}$, we can define a basis for V as follows

$$\{\varphi_i = \frac{\widehat{\varphi}_i}{\omega} \circ \mathbf{F}^{-1}\}_{i=1}^{N_h}.$$

Semidiscrete problem for Bidomain and Monodomain are obtained by applying a standard Galerkin procedure. Let $M = [m_{ij}]$, $A = [a_{ij}]$ and $A_{I,E} = [a_{ij}^{I,E}]$ be the symmetric mass and stiffness matrices. All these coefficients are given by values of the integrals over Ω, that are numerically approximated by a suitable quadrature rule. In order to describe this rule, we introduce $\widehat{\mathcal{K}} := \{\widehat{K}_i\}_{i=1}^{N_e}$, a partition of the parametric domain into N_e nonoverlapping subdomains, that we refer to as the *elements*. The assumption on $\mathbf{F}$ ensure that also the closure of Ω can be partitioned into nonoverlapping *elements* $\mathcal{K} = \{K_i = \mathcal{F}(\widehat{K}_i)\}_{i=1}^{N_e}$. We assume that a quadrature rule is defined on every element of $\widehat{\mathcal{K}}$ and it is determined by a set of n_k nodes and by their corresponding weights

$$\{\widehat{\mathbf{x}}_{rs}\}_{s=1}^{n_k} \subset \widehat{\mathcal{K}} \quad \{w_{rs}\}_{s=1}^{n_k} \subset \mathbb{R} \quad s = 1, ..., N_e.$$

Recalling that the integral of a generic function $f \in \mathcal{L}^1(K_r)$ can be written as

$$\int_{K_r} f d\mathbf{x} = \int_{\widehat{K}_r} f(\mathbf{F}(\widehat{\mathbf{x}}))|\det(D\mathbf{F}(\widehat{\mathbf{x}}_{rs}))| d\widehat{\mathbf{x}} \approx \sum_{r=1}^{n_k} w_{rs} f(\mathbf{x}_{rs})|\det(D\mathbf{F}(\widehat{\mathbf{x}}_{rs}))| \tag{5.3}$$

where $D\mathbf{F}$ is the Jacobian matrix of $\mathbf{F}$ and $\mathbf{x}_{rs} := \mathbf{F}(\widehat{\mathbf{x}}_{rs})$ are the images of the quadrature nodes in the physical domain. The coefficients of the mass and stiffness matrices are computed numerically as

$$m_{ij} = \int_\Omega \varphi_i \varphi_j \approx \sum_{r=1}^{N_e} \sum_{s=1}^{n_k} w_{rs} \varphi_i(\mathbf{x}_{rs}) \varphi_j(\mathbf{x}_{rs}) |\det(D\mathbf{F}(\widehat{\mathbf{x}}_{rs}))| \tag{5.4}$$

$$a_{ij} = \int_\Omega (\nabla\varphi_j)^T D_I \nabla\varphi_i \approx \sum_{r=1}^{N_e} \sum_{s=1}^{n_k} w_{rs} (\nabla\varphi_j^T D\nabla\varphi_i)(\mathbf{x}_{rs}) |\det(D\mathbf{F}(\widehat{\mathbf{x}}_{rs}))|, \tag{5.5}$$

$$a_{ij}^{I,E} = \int_\Omega (\nabla\varphi_j)^T D_{I,E} \nabla\varphi_i \approx \sum_{r=1}^{N_e} \sum_{s=1}^{n_k} w_{rs} (\nabla\varphi_j^T D_{I,E} \nabla\varphi_i)(\mathbf{x}_{rs}) |\det(D\mathbf{F}(\widehat{\mathbf{x}}_{rs}))|. \tag{5.6}$$

$i, j = 1 \ldots N_h$.

Let $\mathbf{i}_{ion}$ be the vector of the coefficients of the L^2 projection of i_{ion} into V computed as

$$(\mathbf{i}_{ion})_i := \int_\Omega i_{ion}(v_M, w) \varphi_i \mathrm{d}\mathbf{x} \approx \sum_{r=1}^{N_e} \sum_{s=1}^{n_k} w_{rs} i_{ion}(v_M(\mathbf{x}_{rs}), w(\mathbf{x}_{rs})) \varphi_i(\mathbf{x}_{rs}) |\det(D\mathbf{F}(\widehat{\mathbf{x}}_{rs}))| \tag{5.7}$$

$i = 1, ..., N_h$ and analogously for $\mathbf{I}_{app}^{I,E}, \mathbf{I}_{app}$. Denoting by $\mathbf{v}_M$ and $\mathbf{u}_E$ the vectors of the degree of freedom of the isogeometric approximation of v_M and u_E, respectively, the matrix form of the semidiscrete Bidomain problem reads as follows

$$\begin{cases} c_m M \frac{\partial \mathbf{v}_M^h}{\partial t} + A_I(\mathbf{v}_M + \mathbf{u}_E) + \mathbf{i}_{ion}(\mathbf{v}_M, \mathbf{w}) &= \mathbf{I}_{app}^I \\ A_I \mathbf{v}_M + (A_I + A_E)\mathbf{u}_E &= 0 \end{cases}$$

while for the Monodomain, we obtain

$$c_m M \frac{\partial \mathbf{v}_M^h}{\partial t} + A\mathbf{v}_M + \mathbf{i}_{ion}(\mathbf{v}_M, \mathbf{w}) = \mathbf{I}_{app}$$

For both models, the equations are coupled with semidiscrete approximations of the gating and concentration systems.

5.2 Time discretization

We now describe the time discretization scheme employed for solving Bidomain and Monodomain model coupled with the Luo-Rudy I ionic model. This is performed by a decoupled semi-implicit method as proposed in [3], consisting of the two following steps.

Step 1. Given the transmembrane potential at the previous step v_M^n, we first solve the ODEs system for the gating and ionic concentration variables.

The ODE integration approach is based on the Rush-Larsen method. In 1978 [66] they proposed this new method for solving cardiac cell models numerically based on the HH formalism. This method exploits the fact that many of the equations of the cell model systems can be written as

$$\frac{dy}{dt} = \alpha(v_M)(1-y) - \beta(v_M)y = \frac{y - y_\infty}{\tau_y} \tag{5.8}$$

$$y_\infty = \frac{\alpha}{\alpha + \beta} \tag{5.9}$$

$$\tau_y = \frac{1}{\alpha + \beta} \tag{5.10}$$

where the rate constant functions α and β are nonlinear functions of the membrane potential, while the equation is linear in y. By assuming that the membrane potential is constant over each time step, it is possible to derive an update formula based on the exact solution of scalar linear ODEs:

$$y^{n+1} = y_\infty + (y^n - y_\infty)\exp\left(\frac{-\triangle t_n}{\tau_y}\right). \tag{5.11}$$

Step 2 Once $\mathbf{w}^{n+1}$ is computed, a semi-implicit scheme is applied to the reaction-diffusion part, see [3], by using the implicit Euler method for the diffusion term, while the nonlinear reaction term I_{ion} is treated explicitly.

Summarizing the operator of the full evolution system is split by first solving for the gating and concentration variables, given the transmembrane potential at step n, and then solving for v_M^{n+1} and u_E^{n+1} of the Bidomain system satisfying

$$\frac{c_m}{\Delta t}M(\mathbf{v}_M^{n+1} - \mathbf{v}_M^n) + A_I(\mathbf{v}_M^{n+1} + \mathbf{u}_E^{n+1}) + \mathbf{i}_{ion}(\mathbf{v}_M^n, \mathbf{w}^{n+1}) = \mathbf{I}_{app}^I$$
$$A_I\mathbf{v}_M^{n+1} + (A_I + A_E)\mathbf{u}_E^{n+1} = \mathbf{I}_{app}^I + \mathbf{I}_{app}^E \tag{5.12}$$

while for the Monodomain, we solve only for $\mathbf{v}_M^{n+1}$:

$$\frac{c_m}{\Delta t}M(\mathbf{v}_M^{n+1} - \mathbf{v}_M^n) + A(\mathbf{v}_M^{n+1}) + \mathbf{i}_{ion}(\mathbf{v}_M^n, \mathbf{w}^{n+1}) = \mathbf{I}_{app}. \tag{5.13}$$

An adaptive time step scheme is very useful when simulating a complete heart beat, permitting varying Δt in the different phases of an action potential. In fact during the depolarization it is better to use a very short time step, which could

then increase during the *plateau*, before again decreasing during depolarization. The adaptive time-stepping strategy employed is based on controlling the transmembrane potential variation, checking its value at fixed points of the domain, for instance at the quadrature nodes. Therefore, let $\mathcal{M}$ be the set of these selected points in Ω and $v_{\mathbf{x}}^n$ the value of the isogeometric approximation at n-th time step of the transmembrane potential at $\mathbf{x} \in \mathcal{M}$, i.e., $v_{\mathbf{x}}^n = \sum_{i=1}^{N_h} \mathbf{v}_M^n \varphi_i(\mathbf{x})$. We define $\Delta v := \max\{|v_{\mathbf{x}}^n - v_{\mathbf{x}}^{n+1}|, \mathbf{x} \in \mathcal{M}\}$ and $\Delta v_{min} = 0.005$ mV, $\Delta v_{max} = 0.5$ mV, $\Delta t_{min} = 0.05$ ms and $\Delta t_{max} = 6$ ms

- if $\Delta v < \Delta v_{min},\quad \Delta t_{new} = \frac{v_{max}}{\Delta v}\Delta t_{old}\quad$ if $\Delta t_{new} < \Delta t_{max}$;

- if $\Delta v > \Delta v_{max},\quad \Delta t_{new} = \frac{v_{min}}{\Delta v}\Delta t_{old}\quad$ if $\Delta t_{new} > \Delta t_{min}$.

We remark that this semi-implicit treatment leads to the solution of a linear system at each time step. For Bidomain and Monodomain problem the iteration matrices of the system are respectively

$$A_{bido} := \left(\gamma \begin{bmatrix} M & 0 \\ 0 & 0 \end{bmatrix} + \begin{bmatrix} A_I & A_I \\ A_I & A_I + A_E \end{bmatrix}\right) \tag{5.14}$$

and

$$A_{mono} = \gamma M + A \tag{5.15}$$

with $\gamma := \frac{c_m}{\Delta t}$. We remark that A_{mono} is symmetric positive definite, whereas A_{bido} is a symmetric but positive semidefinite matrix, having a zero eigenvalue associated to the $(\mathbf{0}, \mathbf{1})^T$ eigenvector. Therefore as in the continuous Bidomain model, v_M^{n+1} is uniquely determined by the given initial and boundary conditions, while $\mathbf{u}_E^{n+1}$ is determined only up to the same additive time-dependent constant related to a reference potential. Since we consider bounded domains, we can determine this constant by imposing

$$M\mathbf{u_E}^{n+1} = 0, \tag{5.16}$$

which is the discrete counterpart of (3.12).

5.3 Variational formulation of the stationary Bidomain problem

In order to introduce Schwarz preconditioners in the next chapter for the discrete Bidomain system, we rewrite (5.12) as an elliptic variational problem, see [60, 61].

We first define the following spaces

$$\widetilde{V} \ := \ \{\mathbf{u}_E \in V \ : \ \mathbf{1}^T M \mathbf{u}_E = \int_\Omega \mathbf{u}_E = 0\} \tag{5.17}$$

$$U \ := \ V \times \widetilde{V} = \{\mathbf{u} = (\mathbf{u}_I, \mathbf{u}_E) \ : \ \mathbf{u}_I \in V, \ \mathbf{u}_I \in \widetilde{V}\}. \tag{5.18}$$

We note that the solution of (5.12) is equivalent to the following problem.

Problem 1. Pb1 *Given $f \in L^2(\Omega)$, find $\mathbf{u} = (\mathbf{u}_M, \mathbf{u}_E) \in U$ such that*

$$A_{bido}\mathbf{u} = \begin{pmatrix} F \\ 0 \end{pmatrix}$$

where $F = \{F_k\} = \{\int_\Omega f\varphi_k \, d\mathbf{x}\}$, with $\{\varphi_k\}$ the basis of the space V.

Lemma 4. *The bilinear form $((\,\cdot\,,\,\cdot\,)) : U \times U \to \mathbb{R}$ defined as*

$$((\mathbf{u}, \mathbf{w})) := \int_\Omega \nabla(\mathbf{v}_M + \mathbf{u}_E)\nabla(\mathbf{w}_M + \mathbf{w}_E) + \int_\Omega \nabla\mathbf{u}_E\nabla\mathbf{w}_E + \int_\Omega \mathbf{v}_M\mathbf{w}_M$$

is an inner product on U.

Denoting by $||| \cdot ||| : U \times U \to \mathbb{R}^+$ the norm induced by $((\,\cdot\,,\,\cdot\,))$, i.e.,

$$|||\mathbf{u}|||^2 = \int_\Omega (\nabla(\mathbf{v}_M + \mathbf{u}_E))^2 + \int_\Omega (\nabla\mathbf{u}_E)^2 + \int_\Omega (\mathbf{v}_M)^2,$$

we can easily prove the following lemma.

Lemma 5. *Let $a_{bido}(\,\cdot\,,\,\cdot\,) : U \times U \to \mathbb{R}$ be a symmetric bilinear form defined as*

$$a_{bido}(\mathbf{u}, \mathbf{w}) := \int_\Omega (\nabla(\mathbf{v}_M + \mathbf{u}_E))^T D_I \nabla(\mathbf{w}_M + \mathbf{w}_E) + \int_\Omega (\nabla\mathbf{u}_E)^T D_E \nabla\mathbf{w}_E + \gamma \int_\Omega \mathbf{v}_M\mathbf{w}_M,$$

with γ as defined in section 5.2. Then a_{bido} is continuous and elliptic with respect to the norm $||| \cdot |||$.

Proof. The lemma follows from the uniform ellipticity condition (3.29) and the definition of $||| \cdot |||$. To establish continuity, we have

$$\begin{aligned} a_{bido}(\mathbf{u}, \mathbf{w}) &\leq \max\{C_I, C_E, \gamma\}((\mathbf{u}, \mathbf{w})) \\ &\leq C|||\mathbf{u}||| \, |||\mathbf{w}|||, \end{aligned}$$

while ellipticity follows from

$$\begin{aligned} a_{bido}(\mathbf{u}, \mathbf{u}) &\geq \min\{\alpha_I, \alpha_E, \gamma\}((\mathbf{u}, \mathbf{u})) \\ &\geq \alpha|||\mathbf{u}|||^2. \end{aligned}$$

$\square$

We now define the following elliptic variational problem.

Problem 2. *Pb2 Given $f \in L^2(\Omega)$, find $\mathbf{u} \in U^h$ such that*

$$a_{bido}(\mathbf{u}, \mathbf{w}) = (f, \mathbf{w}_M) \quad \forall \mathbf{w} \in U. \tag{5.19}$$

Finally, we find

Lemma 6. *Pb1 and Pb2 are equivalent.*

Proof. **Pb1⇒Pb2**.
If $\mathbf{u}$ is the solution of **Pb1**, then

$$\begin{cases} \int_\Omega (\nabla \mathbf{v}_M)^T D_I \nabla \phi + \gamma \int_\Omega \mathbf{v}_M \phi + \int_\Omega (\nabla \mathbf{u}_E)^T D_I \nabla \phi = (f, \phi) \quad \forall \phi \in V \\ \int_\Omega (\nabla \mathbf{v}_M)^T D_I \nabla \psi + \int_\Omega (\nabla \mathbf{u}_E)^T D_I \nabla \psi + \int_\Omega (\nabla \mathbf{u}_E)^T D_E \nabla \psi = 0 \quad \forall \psi \in V \end{cases}$$

and $\forall \psi \in \widetilde{V}$; summing these last equations we get (5.19).
Pb1⇐Pb2. If $\mathbf{u}$ is a solution of **Pb2** then $\forall (\mathbf{w}_M, \mathbf{w}_E) \in V \times V$ it holds that

$$\int_\Omega (\nabla(\mathbf{v}_M + \mathbf{u}_E))^T D_I \nabla(\mathbf{w}_M + \mathbf{w}_E) + \int_\Omega (\nabla \mathbf{u}_E)^T D_E \nabla \mathbf{w}_E + \gamma \int_\Omega \mathbf{v}_M \mathbf{w}_M = (f, \mathbf{w}_M).$$
$$\tag{5.20}$$

Choosing $\mathbf{w}_E \equiv 0$, we obtain

$$\int_\Omega (\nabla(\mathbf{v}_M + \mathbf{u}_E))^T D_I \nabla \mathbf{w}_M + \gamma \int_\Omega \mathbf{v}_M \mathbf{w}_M = (f, \mathbf{w}_M) \quad \forall \mathbf{w}_M \in V,$$

whereas if $\mathbf{w}_M \equiv 0$, we have

$$\int_\Omega (\nabla(\mathbf{v}_M + \mathbf{u}_E))^T D_I \nabla \mathbf{w}_E + \int_\Omega (\nabla \mathbf{u}_E)^T D_E \nabla \mathbf{w}_E = 0 \quad \forall \mathbf{w}_E \in \widetilde{V}.$$

The last equality holds for all $\mathbf{w}_E \in V$, since it holds for $\mathbf{w}_E \equiv 1$. $\qquad \square$

Chapter 6

Schwarz preconditioners

6.1 Abstract theory of Schwarz preconditioners

We recall the main results of the abstract convergence theory of Schwarz methods (see [79] and [53]).

Let U be a finite dimensional Hilbert space with the inner product $(\cdot\,,\cdot)$. Given a symmetric elliptic bilinear form

$$a(\,\cdot\,,\,\cdot\,) : U \times U \to \mathbb{R}$$

and $f \in U'$, consider the following problem.
Find $u \in U$ such that
$$a(u,v) = f(v) \quad \forall v \in U.$$

Given a basis for U, this problem is equivalent to solving the linear system

$$Au = f \tag{6.1}$$

where A is the stiffness matrix associated with the bilinear form $a(\,\cdot\,,\,\cdot\,)$. We use the same notation for functions and corresponding vectors of degrees of freedom. Now we consider the subspaces U_m, $m = 0, ..., N$ and the interpolation operators

$$R_m^T : V_m \to V. \tag{6.2}$$

In addition we assume that V admits the following decomposition

$$V = R_0^T V_0 + \sum_{m=1}^{N} R_m^T V_m. \tag{6.3}$$

This decomposition is not necessarily a direct sum of subspaces; V_m, $m = 0, ..., N$ do not need to be subspaces of V and the decomposition of a function needs not be unique.

We introduce local symmetric, positive definite, bilinear forms on each subspaces

$$\widetilde{a}(\,\cdot\,,\,\cdot\,) : V_m \times V_m \to \mathbb{R} \quad m = 0, ..., N, \tag{6.4}$$

and the corresponding local stiffness matrices, $\widetilde{A}_m$, associated with them.
We say that we use *exact local solvers*, if we chose

$$\widetilde{a}(u_m, v_m) = a(R_m^T u_m, R_m^T v_m), \quad u_m, v_m \in V_m. \tag{6.5}$$

Then,

$$\widetilde{A}_m = R_m A R_m^T. \tag{6.6}$$

Schwarz operators are defined by

$$P_m = R_m^T \widetilde{P}_m : V \to R_m^T V_m \subset V, \quad m = 0, ..., N, \tag{6.7}$$

where $\widetilde{P}_m : V \to V_m$ is defined by

$$\widetilde{a}(\widetilde{P}_m u, v_m) = a(u, R_m^T v_m) \quad v_m \in V_m. \tag{6.8}$$

In case of exact solvers, it holds

$$a(P_m u, R_m^T v_m) = a(u, R_m^T v_m) \quad v_m \in V_m.$$

We have the following lemma, see [79, Section 2.2]

Lemma 7. *The P_m can be written as*

$$P_m = R_m^T \widetilde{A}_m^{-1} R_m A \quad 0 \le m \le N. \tag{6.9}$$

It is selfadjoint with respect to the scalar product induced by $a(\,\cdot\,,\,\cdot\,)$ and positive semidefinite. If (6.5) holds, then it is a projection, i.e.,

$$P_m^2 = P_m.$$

Given a set of subspace and local bilinear forms, we can define the additive Schwarz operator as

$$P_{as} := \sum_{m=0}^{N} P_m. \tag{6.10}$$

We note that P_{as} is a preconditioned operator for the original operator A. In fact

$$P_{as} = A_{as}^{-1}A, \quad A_{as}^{-1} = \sum_{m=0}^{N} R_m^T \widetilde{A}_m^{-1} R_m.$$

Therefore, the original system (6.1) can be written as

$$P_{as}u = g_{as}, \tag{6.11}$$

where $g_{as} = A_{as}^{-1}f$. P_{as} is symmetric and, under suitable assumptions, positive definite, and we can then use the conjugate gradient methods for the solution of (6.11). We need bounds for the condition number of P_{as}, in order to analyze its convergence. It is enough to make the following three assumptions.

Assumption 6.1. *(**Stable decomposition**) There exists a constant C_0, such that $u \in V$ admits a decomposition*

$$u = \sum_{m=0}^{N} R_m^T u_m, \quad \{u_m \in V_m, \; 0 \le m \le N\}$$

such that

$$\sum_{m=0}^{N} \widetilde{a}_m(u_m, u_m) \le C_0^2 a(u, u).$$

Thus, we have the following result, see [79, Lemma 2.5].

Lemma 8. *Under Assumption 6.1 it holds*

$$a(P_{as}u, u) \ge C_0^2 a(u, u), \quad u \in V.$$

Therefore P_{as} is invertible.

A stable decomposition provides a positive estimate from below of the smallest eigenvalue of P_{as}, recalling that the condition number of P_{as} can be written as

$$\kappa(P_{as}) = \frac{\lambda_{max}(P_{as})}{\lambda_{min}(P_{as})},$$

where

$$\lambda_{max}(P_{as}) = \sup_{u \in V} \frac{a(P_{as}u, u)}{a(u, u)}, \quad \lambda_{min}(P_{as}) = \inf_{u \in V} \frac{a(P_{as}u, u)}{a(u, u)}.$$

Assumption 6.2. (***Strengthened Cauchy-Schwarz inequalities***) *There exist* $0 \leq \epsilon_{mn} \leq 1$, $1 \leq m, n \leq N$, *such that*

$$|a(R_m^T u_m, R_n^T u_n)| \leq \epsilon_{mn} a(R_m^T u_m, R_m^T u_m)^{1/2} a(R_n^T u_n, R_n^T u_n)^{1/2},$$

for $u_m \in V_m$ *and* $u_n \in V_n$. *Let* $\rho(\mathcal{E})$ *be the spectral radius of* $\mathcal{E} := \{\epsilon_{mn}\}$.

Assumption 6.3. (***Local stability***) *There exists* $\omega > 0$, *such that*

$$a(R_m^T u_m, R_m^T u_m) \leq \omega \widetilde{a}_m(u_m, u_m), \quad u_m \in Im(\widetilde{P}_m) \subset V_m, \quad 0 \leq m \leq N.$$

If exact local solvers are used, $\omega = 1$.
Assumption 4.2, 4.3 provide an upper bound for $\lambda_{max}(P_{as})$, see [79, Lemma2.6] .

Lemma 9. *Under Assumption 6.2 and 6.3, we have*

$$a(P_{as}u, u) \leq \omega(\rho(\mathcal{E}) + 1)a(u, u), \quad u \in V.$$

Therefore P_{as} *is invertible.*

Combining the previous Lemmas, we have

Theorem 6.1.1. *Let Assumptions 6.1, 6.2 and 6.3 be satisfied. Then it holds the following bound for the condition number of the additive Schwarz operator*

$$\kappa(P_{as}) \leq C_0^2 \omega(\rho(\mathcal{E}) + 1).$$

6.2 Isogeometric overlapping Schwarz preconditioners for the Bidomain system

In this section, we construct an isogeometric overlapping additive Schwarz preconditioner for the Bidomain system, using the general framework developed in [9] for elliptic problem, and in [60] [61] for the Bidomain system discretized using the finite elements method.

We first describe the subdomains and subspaces decomposition in one dimension for the B-splines space in parametric space, and then extend them by using tensor products to two and three dimensions and also for NURBS space in the physical space.

As usual, d is the dimension of the physical domain. For any integer α with $1 \leq \alpha \leq d$, we define a decomposition of the reference interval $\widehat{I}$ by selecting from

the open knot vector $\{\xi_{1,\alpha} = 0, ..., \xi_{n_\alpha+p+1,\alpha} = 1\}$ a subset of $N_\alpha + 1$ nonrepeated interface knots $\{\xi_{i_{m_\alpha},\alpha}, m_\alpha = 1, ..., N_\alpha + 1 | \xi_{i_1,\alpha} = 0, \xi_{i_{N_\alpha+1},\alpha} = 1\}$. Thus, the closure of $\widehat{I}$ can be decomposed into N_α interval in the following way

$$\overline{\widehat{I}} = [0,1] = \overline{\bigcup_{m_\alpha=1,..,N_\alpha} \widehat{I}_{m_\alpha,\alpha}} \quad \widehat{I}_{m_\alpha,\alpha} := (\xi_{i_{m_\alpha},\alpha}, \xi_{i_{m_\alpha+1},\alpha}). \tag{6.12}$$

We assume that each $\widehat{I}_{m_\alpha,\alpha}$ has a similar diameter on order H.

For each of the interface knots $\xi_{i_{m_\alpha},\alpha}$ there exists at least one index $s_{m_\alpha,\alpha}$ (strictly increasing in m_α) such that $2 \leq s_{m_\alpha,\alpha} \leq n_\alpha - 1$, and satisfying $s_{m_\alpha,\alpha} < i_{m_\alpha} < s_{m_\alpha,\alpha}+p+1$, so that the support of the support of the basis function $B^p_{s_{m_\alpha,\alpha}}$ intersects both $\widehat{I}_{m_\alpha-1,\alpha}$ and $\widehat{I}_{m_\alpha,\alpha}$.

In order to build an overlapping decomposition of $\widehat{I}$, let $r \in \mathbb{N}$ be an integer counting the basis functions shared by adjacent subdomains. We are able to define N_α subspaces $\{\widehat{V}_{m_\alpha,\alpha}\}_{m_\alpha=1}^{N_\alpha}$ forming an overlapping decomposition of $\widehat{V}$, as

$$\widehat{V}_{m_\alpha\alpha} := \mathrm{span}\{B^p_{j,\alpha}(\xi)|s_{m_\alpha,\alpha} - r \leq j \leq s_{m_\alpha+1,\alpha} + r\} \quad m_\alpha = 1, ..., N_\alpha. \tag{6.13}$$

For $r = 0$ the overlap is minimal, consisting of just one common basis function between the subspaces. With r, we define another parameter

$$\delta := h(2r + 2) \tag{6.14}$$

related to the width of the overlapping region; we will refer to it as the overlap parameter.

Recalling that the support of a general basis function $B^p_{i,\alpha}(\xi)$ consists of the interval $(\xi_{i,\alpha}, \xi_{i+p+1,\alpha})$, we define the extended subdomains $\widehat{I}'_{m_\alpha,\alpha}$ by

$$\widehat{I}'_{m_\alpha,\alpha} := \bigcup_{B^p_{j,\alpha} \in \widehat{V}_{m_\alpha,\alpha}} \mathrm{supp}(B^p_{j,\alpha}) = (\xi_{s_{m_\alpha,\alpha}-r,\alpha}, \xi_{s_{m_\alpha+1,\alpha}+r+p+1,\alpha}). \tag{6.15}$$

In addition, we need to define further extended subdomains $\widehat{I}''_{m_\alpha,\alpha}$

$$\widehat{I}''_{m_\alpha,\alpha} := \bigcup_{\mathrm{supp}(B^p_{j,\alpha}) \cap \widehat{I}'_{m_\alpha,\alpha} \neq \emptyset} \mathrm{supp}(B^p_{j,\alpha}). \tag{6.16}$$

Finally we build the coarse space $\widehat{V}_{0,\alpha}$ from the nonoverlapping decomposition $\{\widehat{I}_{m_\alpha,\alpha}\}_{m_\alpha=1}^{N_\alpha}$. Let

$$\Xi_{0,\alpha} = \{\xi_{1,\alpha}, ..., \xi_{p,\alpha}, \xi_{i_1,\alpha}, \xi_{i_2,\alpha}, ..., \xi_{i_{N_\alpha-1},\alpha}, \xi_{i_{N_\alpha},\alpha}, \xi_{i_{N_\alpha+1},\alpha}, ..., \xi_{i_{N_\alpha+p+1},\alpha}\} \tag{6.17}$$

such that $\xi_{1,\alpha} = \xi_{p,\alpha} = \xi_{i_1,\alpha} = 0$ and $\xi_{i_{N_\alpha+1},\alpha} = \xi_{i_{N_\alpha+2},\alpha} = ... = \xi_{i_{N_\alpha+p+1},\alpha} = 1$, and let $\{\overset{\circ}{B}{}^p_{i,\alpha}\}^{N_{0,\alpha}}_{i=1}$ be the corresponding $N_{0,\alpha}$ basis function

$$\widehat{V}_{0,\alpha} = \text{span}\{\overset{\circ}{B}{}^p_{i,\alpha}, \quad i = 1...N_{0,\alpha}\}. \tag{6.18}$$

In more than one dimension, we proceed by using tensor product; we define subdomains, overlapping subdomains, and extended supports. Let $N := \prod^d_1 N_\alpha$, for $m = 1, ..., N$

$$\widehat{\Omega}_m \equiv \widehat{\Omega}_{m_1,...,m_d} := \otimes^d_{\alpha=1} \widehat{I}_{m_\alpha} \qquad \widehat{\Omega}'_m \equiv \widehat{\Omega}'_{m_1,...,m_d} := \otimes^d_{\alpha=1} \widehat{I}'_{m_\alpha} \tag{6.19}$$

$$\widehat{\Omega}''_m \equiv \widehat{\Omega}''_{m_1,...,m_d} := \otimes^d_{\alpha=1} \widehat{I}''_{m_\alpha} \qquad m_\alpha = 1, ..., N_\alpha, \quad \alpha = 1, .., d. \tag{6.20}$$

The local and the coarse subspaces are then
$\widehat{U}_m := \widehat{V}_m \times \widehat{V}_m$ with

$$\widehat{V}_m \equiv \widehat{V}_{m_1,...,m_d} := \text{span}\{B^p_{i_1,...,i_d}, \ s_{m_\alpha} - r \leq i_\alpha \leq s_{m_\alpha+1} + r, \ \alpha = 1, ..., N_\alpha\}; \tag{6.21}$$

$\widehat{U}_0 = \widehat{V}_0 \times \widetilde{\widehat{V}}_0$ with

$$\widehat{V}_0 := \text{span}\{\overset{\circ}{B}{}^p_{i_1,...,i_d}, \quad i_\alpha = 1...N_{0,\alpha}, \ \alpha = 1, ..., N_\alpha\} \text{ and } \widetilde{\widehat{V}}_0 := \widehat{V}_0 \cap \widetilde{\widehat{V}}. \tag{6.22}$$

The subdomains in the physical space are defined as the image of the subdomains in the parameter space under the mapping $\mathbf{F}$,

$$\Omega_m = \mathbf{F}(\widehat{\Omega}_m), \quad \Omega'_m = \mathbf{F}(\widehat{\Omega}'_m) \quad \Omega''_m = \mathbf{F}(\widehat{\Omega}''_m) \tag{6.23}$$

The decomposition of the NURBS space V and therefore of U in the physical domain is trivial:
$U_m := V_m \times V_m$ with

$$V_m \equiv V_{m_1,...,m_d} := \text{span}\{R^p_{i_1,...,i_d} \circ \mathbf{F}^{-1}, \ s_{m_\alpha} - r \leq i_\alpha \leq s_{m_\alpha+1} + r, \ \alpha = 1, ..., N_\alpha\};$$
$$\tag{6.24}$$

$\widehat{U}_0 = \widehat{V}_0 \times \widetilde{\widehat{V}}_0$ with

$$V_0 := \text{span}\{\overset{\circ}{R}{}^p_{i_1,...,i_d} \circ \mathbf{F}^{-1}, \quad i_\alpha = 1...N_{0,\alpha}, \ \alpha = 1, ..., N_\alpha\} \quad \text{and} \quad \widetilde{V}_0 := V_0 \cap \widetilde{V}.$$
$$\tag{6.25}$$

We are now able to construct a two-level overlapping Additive Schwarz method for problem (5.12).

We remark that $U_0 \subset U$, whereas U_m is not a subset of U, $m = 1, ..., N$. We therefore define the interpolation operators $\mathbf{I}_m : U_m \to U$ by

$$\text{given } u = (v_M, \ u_E) \in U_m, \quad \mathbf{I}_m u = (\mathbf{I}_{m,M} u, \mathbf{I}_{m,E} u) := (v_M, u_E - \frac{1}{|\Omega|} \int_\Omega u_E),$$
(6.26)

whereas $\mathbf{I}_0 : U_0 \to U$ is simply the embedding operator. We define the local projectors operators for $m = 0, ..., N$

$$\widetilde{\mathbf{T}}_m : U \to U_m$$

by

$$a_{bido}(\widetilde{\mathbf{T}}_m u, v) = a_{bido}(u, \mathbf{I}_m v) \quad \forall v \in U_m.$$

Defining $\mathbf{T}_m = \mathbf{I}_m \widetilde{\mathbf{T}}_m$, the 2-level Overlapping Additive Schwarz operator is then

$$\mathbf{T}_{OAS} := T_0 + \sum_{m=1}^{N} \mathbf{T}_m.$$
(6.27)

6.3 A convergence rate analysis

In the following section, we extend the results for IGA overlapping additive Schwarz preconditioner to a bound for condition number of the operator $\mathbf{T}_{OAS}$.

We first make the following two assumptions on the mesh and subdivision.

- the parametric domain in each extended subdomain $\widehat{\Omega}''_m$ is uniform, i.e., there exist a real number $h = h(\widehat{\Omega}''_m)$ such that all elements in $\widehat{\Omega}''_m$ have a diameter which is on the order of h, i.e., bounded from above and below by Ch for constant C which is the same for all the subdomains ;

- the overlap index r is bounded from above by a fixed constant.

We will adopt the following notation: given two real numbers a and b we write $a \lesssim b$ when $a \leq Cb$ for a generic positive constant C independent of the knot vectors.

Interpolation operators

For any integer α, $1 \leq \alpha \leq d$, given any function $v \in \widehat{V}$, we define its restriction to the univariate spline space of degree p generated by the open knot vector Ξ_α

$$v_\alpha(\eta_\alpha) := v(\eta) \qquad \forall \eta \equiv (\eta_1, ..., \eta_d) \in \widehat{\Omega}$$
(6.28)

v_α can be represented as a linear combination of $\{B_{i,\alpha}\}_{i=1}^n$, in particular, there exist $\{c_{i_\alpha,\alpha}\}_{i_\alpha=1}^{n_\alpha}$ such that

$$v_\alpha = \sum_{i_\alpha=1}^{n_\alpha} c_{i_\alpha,\alpha} B_{i_\alpha,\alpha}^p \tag{6.29}$$

We define the operators $\widehat{\Pi}^{m_\alpha,\alpha} : \widehat{V} \to \widehat{V} \ m_\alpha = 1, ..., N_\alpha$ as follows

$$\widehat{\Pi}^{m_\alpha,\alpha} v := \sum_{i_\alpha=s_{m_\alpha,\alpha}-r}^{s_{m_\alpha+1,\alpha}+r} d_{i_\alpha,\alpha} c_{i_\alpha,\alpha} B_{i_\alpha,\alpha}^p \tag{6.30}$$

where

$$d_{i_\alpha,\alpha} = \begin{cases} \frac{r-s_{m_\alpha,\alpha}+1+i_\alpha}{2r+2} & \text{if} \quad s_{m_\alpha,\alpha}-r \leq i_\alpha \leq s_{m_\alpha,\alpha}+r \\ 1 & \text{if} \quad s_{m_\alpha,\alpha}-r+1 \leq i_\alpha \leq s_{m_\alpha+1,\alpha}-r-1 \\ \frac{s_{m_\alpha+1,\alpha}+r+1-i_\alpha}{2r+2} & i_\alpha \geq s_{m_\alpha+1,\alpha}-r \end{cases} \tag{6.31}$$

We remark that we are assuming that the overlap index r is not too large, i.e.,

$$s_{m_\alpha,\alpha} + r + 1 \leq s_{m_\alpha+1,\alpha} - r - 1. \tag{6.32}$$

It easy to check that we have

$$v = \sum_{m_\alpha=1}^{N_\alpha} \widehat{\Pi}^{m_\alpha,\alpha} v. \tag{6.33}$$

We are now able to build the interpolation operator by $\widehat{\Pi}^m : \widehat{V} \to \widehat{V}_m$

$$\widehat{\Pi}^m v = \widehat{\Pi}^{m_1,1} \circ ... \circ \widehat{\Pi}^{m_d,d} v. \tag{6.34}$$

Now we give a technical result useful in the following, see ([9, Theorem 4.1])

Lemma 10. *For all $v \in \widehat{V}$, it holds that*

$$\|\widehat{\Pi}^m v\|_{L^2(\widehat{\Omega}'_m)} \leq C \|v\|_{L^2(\widehat{\Omega}''_m)}. \tag{6.35}$$

The following result holds.

Theorem 6.3.1. *The condition number of the 2-level additive Schwarz preconditioned isogeometric operator $\mathbf{T}_{OAS}$ (6.27) is bounded by*

$$\kappa_2(\mathbf{T}_{OAS}) \leq C \left(1 + \frac{H}{\delta} \right),$$

where $\delta := h(2r+2)$ is the overlap parameter and C is a constant independent of h, H, N and δ but not of p and k.

Proof. The proof follows by using the general abstract theory [79, Chapter 2].

1. Since we use exact solvers, the local stability assumption holds true with $\omega = 1$.

2. By using a standard coloring argument the strengthened Cauchy-Schwarz inequality holds, with a constant bounded from above by the number of colors.

3. We are left with proving a stable decomposition for our subspace decomposition.

We start by presenting a stable splitting for the case of splines in the parametric domain.

Let $\widehat{\Pi}^0$ the standard quasi-interpolant into the space $\widehat{V}_0$.

Given $\widehat{u} = (\widehat{v}_M, \widehat{u}_E) \in \widehat{U}$, we define

$$\widehat{u}_0 = (\widehat{v}_{0,M}, \widehat{u}_{0,E}) := (\widehat{\Pi}^0 \widehat{v}_M, \widehat{\Pi}^0 \widehat{u}_E) \in \widehat{U}_0 \tag{6.36}$$

$$\widehat{u}_m = (\widehat{v}_{m,M}, \widehat{u}_{m,E}) := (\widehat{\Pi}^m(\widehat{v}_M - \widehat{v}_{0,M}), \widehat{\Pi}^m(\widehat{u}_E - \widehat{u}_{0,E})). \tag{6.37}$$

It easy to check that we have the splitting

$$\widehat{u} = \sum_{m=0}^{N} \mathbf{I}_m \widehat{u}_m. \tag{6.38}$$

We have to show that there exists a constant C such that for very $\widehat{u} \in \widehat{U}$ (6.38) satisfies

$$\sum_{m=0}^{N} |||\widehat{u}_m|||^2 \leq C^2 |||\widehat{u}|||^2 \tag{6.39}$$

where $||| \cdot |||$ is the norm defined in Sec. 5.3.

We can bound each scalar component as in the proof of scalar elliptic problems (see [9])

$$\sum_{m=0}^{N} |\widehat{v}_{m,M}|^2_{H^1(\widehat{\Omega})} \lesssim \left(1 + \frac{H}{\delta}\right) |\widehat{v}_M|^2_{H^1(\widehat{\Omega})} \tag{6.40}$$

$$\sum_{m=0}^{N} |\widehat{u}_{m,E}|^2_{H^1(\widehat{\Omega})} \lesssim \left(1 + \frac{H}{\delta}\right) |\widehat{u}_E|^2_{H^1(\widehat{\Omega})}. \tag{6.41}$$

Thus, using Young's inequality and the bounds (6.40) and (6.41), it holds that

$$\sum_{m=0}^{N} |\widehat{v}_{m,M} + \widehat{u}_{m,E}|^2_{H^1(\widehat{\Omega})} \lesssim \sum_{m=0}^{N} |\widehat{v}_{m,M}|^2_{H^1(\widehat{\Omega})} + \sum_{m=0}^{N} |\widehat{u}_{m,E}|^2_{H^1(\widehat{\Omega})} \tag{6.42}$$

$$\lesssim \left(1 + \frac{H}{\delta}\right) (|\widehat{v}_M|^2_{H^1(\widehat{\Omega})} + |\widehat{u}_E|^2_{H^1(\widehat{\Omega})}) \tag{6.43}$$

$$\lesssim \left(1 + \frac{H}{\delta}\right) (|\widehat{v}_M + \widehat{u}_E|^2_{H^1(\widehat{\Omega})} + |\widehat{u}_E|^2_{H^1(\widehat{\Omega})}). \tag{6.44}$$

It now remains to estimate the L^2-norm of $\widehat{v}_{m,M}$. Since $\widehat{v}_{m,M} \in \widehat{V}_m$ for all $m = 1, ..., N$ its support is contained in $\widehat{\Omega}'_m$. Then applying Lemma 10 and the stability of the quasi-interpolant $\widehat{\Pi}^0$ (4.28), we obtain

$$||\widehat{v}_{m,M}||^2_{L^2(\widehat{\Omega})} = ||\widehat{v}_{m,M}||^2_{L^2(\widehat{\Omega}'_m)} \tag{6.45}$$

$$\lesssim ||\widehat{v}_M - \widehat{v}_{0,M}||^2_{L^2(\widehat{\Omega}''_m)} \tag{6.46}$$

$$\lesssim ||\widehat{v}_M||^2_{L^2(\widehat{\Omega}''_m)}. \tag{6.47}$$

Since the last bound hold for all m, including $m = 0$, and each point of the extended subdomains $\widehat{\Omega}''_m$ is covered by a uniformly bounded number of subdomains, by a standard coloring argument gives the inequality

$$\sum_{m=0}^{N} ||\widehat{v}_{m,M}||^2_{L^2(\widehat{\Omega})} \lesssim ||\widehat{v}_M||^2_{L^2(\widehat{\Omega})}. \tag{6.48}$$

Adding (6.48) and the bounds (6.44) and (6.41), we have

$$\sum_{m=0}^{N} |||\widehat{u}_m|||^2 \lesssim \left(1 + \frac{H}{\delta}\right) |||\widehat{u}|||. \tag{6.49}$$

Finally we present the stable splitting for the NURBS in the physical domain. By definition of the space V we have

$$V = \left\{ \frac{\widehat{v}}{\omega} \circ \mathbf{F}^{-1}; \quad \widehat{v} \in \widehat{V} \right\}$$

where ω is the weight function. Let u be any function in V, then there exists $\widehat{u}$ such that $u = (\widehat{u}/\omega) \circ \mathbf{F}^{-1}$. Introducing the functions in V_m by

$$v_{m,M} = \frac{\widehat{v}_{m,M}}{\omega} \circ \mathbf{F}^{-1} \quad u_{m,E} = \frac{\widehat{u}_{m,E}}{\omega} \circ \mathbf{F}^{-1} \quad \forall m = 0, .., N, \tag{6.50}$$

we obtain the splitting $u = \sum_{m=0}^{N} \mathbf{I}_m u_m$ from (6.38).

Applying a standard change of variables (4.32) from Ω to $\widehat{\Omega}$, (6.47) and (6.40) and finally mapping back into Ω, tanks to (4.31), we obtain

$$\sum_{m=0}^{N} |v_{m,M}|_{H^1(\Omega)}^2 \quad \lesssim \quad \sum_{m=0}^{N} \|\widehat{v}_{m,M}\|_{H^1(\widehat{\Omega})}^2 \tag{6.51}$$

$$\lesssim \quad \left(1 + \frac{H}{\delta}\right) |\widehat{v}_M|_{H^1(\widehat{\Omega})}^2 + \|\widehat{v}_M\|_{L^2(\widehat{\Omega})}^2 \tag{6.52}$$

$$\lesssim \quad \left(1 + \frac{H}{\delta}\right) \left(|v_M|_{H^1(\Omega)}^2 + \|\widehat{v}_M\|_{L^2(\Omega)}^2\right). \tag{6.53}$$

Analogously for the second component of u_m

$$\sum_{m=0}^{N} |u_{m,E}|_{H^1(\Omega)}^2 \quad \lesssim \quad \sum_{m=0}^{N} \|\widehat{u}_{m,E}\|_{H^1(\widehat{\Omega})}^2 \tag{6.54}$$

$$\lesssim \quad \left(1 + \frac{H}{\delta}\right) |\widehat{v}_M|_{H^1(\widehat{\Omega})}^2 + \|\widehat{u}_M\|_{L^2(\widehat{\Omega})}^2 \tag{6.55}$$

$$\lesssim \quad \left(1 + \frac{H}{\delta}\right) |u_E|_{H^1(\Omega)}^2 \tag{6.56}$$

where in (6.56) we can apply Poincaré's inequality, since u_E has zero mean value. Finally applying the triangle and Young's inequalities, it holds

$$\sum_{m=0}^{N} |v_{m,M} + u_{m,E}|_{H^1(\Omega)}^2 \quad \leq \quad \sum_{m=0}^{N} (|v_{m,M}|_{H^1(\Omega)} + |u_{m,E}|_{H^1(\Omega)})^2 \tag{6.57}$$

$$\lesssim \quad \sum_{m=0}^{N} |v_{m,M}|_{H^1(\Omega)}^2 + \sum_{m=0}^{N} |u_{m,E}|_{H^1(\Omega)}^2 \tag{6.58}$$

$$\lesssim \quad \left(1 + \frac{H}{\delta}\right) \left(|v_M|_{H^1(\Omega)}^2 + \|v_M\|_{L^2(\Omega)}^2 + |u_{m,E}|_{H^1(\Omega)}^2\right) \tag{6.59}$$

$$\lesssim \quad \left(1 + \frac{H}{\delta}\right) \left(|v_M + u_E|_{H^1(\Omega)}^2 + \|v_M\|_{L^2(\Omega)}^2 + |u_{m,E}|_{H^1(\Omega)}^2\right).$$

We obtain a stable decomposition

$$\sum_{m=0}^{N} \left(|v_{m,M} + u_{m,E}|_{H^1(\Omega)}^2 + |u_{m,E}|_{H^1(\Omega)}^2 + \|v_{m,M}\|_{L^2(\Omega)}^2\right)$$

$$\lesssim \left(1 + \frac{H}{\delta}\right) (|v_M + u_E|_{H^1(\Omega)}^2 + |u_E|_{H^1(\Omega)}^2 + \|v_M\|_{L^2(\Omega)}^2). \tag{6.60}$$

$\square$

Chapter 7

Numerical Results

The numerical results presented hereafter concern the 3D Monodomain and Bidomain models on portion of truncated ellipsoids, representing a simplified ventricular geometry, or on a cartesian slab, representing a cardiac wedge. The geometry is combined with an analytical representation of the cardiac fiber architecture as detailed in Chapter 5. The ionic model considered in this implementation is the LuoRudy Phase I ionic model [50], with its original parameters, while the main parameters of the cardiac tissue model are reported in Table 7.1. The numerical simulations are carried out using our MATLAB code that employs the IMEX time discretization and IGA space discretization described in Chapter 5; our IGA code is based on the library GeoPDEs [25]. The details of the implementation of the Bidomain preconditioning strategy are as follows: at each time step, we solve the Bidomain or Monodomain discrete system with the PCG iterative method with stopping criterion based on the control of the 2-norm of the current residual, normalized with respect to the 2-norm of the initial residual and with tolerance set to 10^{-6}. As initial guess we use the solution from the previous time step; other choices of initial guesses for the Bidomain model were investigated in [83]. The PCG iterations are accelerated with the Overlapping Additive Schwarz (OAS) preconditioners described in Chapter 6, with overlap index r specified in each test.

The computations are carried out on a workstation equipped with a 2.2 GHz AMD Dual-Core Opteron processor and 8 GB RAM. To the best of our knowledge, these are the first isogeometric simulations of cardiac reaction-diffusion models on 2D and 3D domains.

	$\chi = 10^3$ cm^{-1}, $C_m = 10^{-3}$mF/cm^2
Monodomain parameters	$\sigma_l^m = 1.2 \cdot 10^{-3}\Omega^{-1}$ cm^{-1}, $\sigma_t^m = 2.5562 \cdot 10^{-3}\Omega^{-1}$ cm^{-1}
Bidomain parameters	$\sigma_l^E = 2 \cdot 10^{-3}\Omega^{-1}$ cm^{-1}, $\sigma_l^I = 3 \cdot 10^{-3}\Omega^{-1}$ cm^{-1} $\sigma_t^E = 1.3514 \cdot 10^{-3}\Omega^{-1}$ cm^{-1}, $\sigma_t^I = 3.1525 \cdot 10^{-4}\Omega^{-1}$ cm^{-1} $\sigma_n^E = \sigma_t^E/2$, $\sigma_n^I = \sigma_t^I/10$
Initial value	$\mathbf{u}_I^0 = 84$ mV, $\mathbf{u}_E^0 = 0$ mV $\mathbf{v}_M^0 = 84$ mV

Table 7.1: Parameters calibration for the numerical tests.

7.1 A complete heartbeat with the Monodomain–LR1 model

We start our simulations with the Monodomain model, coupled with LR1 membrane model, and simulate a complete heartbeat on a large portion of a half truncated ellipsoid described by the parametric equations

$$
\begin{cases}
x = a(r)\cos(\theta)\cos(\phi) & \phi_{min} \leq \phi \leq \phi_{max} \\
y = b(r)\cos(\theta)\sin(\phi) & \theta_{min} \leq \theta \leq \theta_{max} \\
z = c(r)\sin(\theta) & 0 \leq r \leq 1,
\end{cases}
$$

where $a_1 = b_1 = 1.5$, $a_2 = b_2 = 2.7$ and $c_1 = 4.4$ $c_2 = 5$ all in cm, $\phi_{min} = 0$, $\phi_{max} = 2\pi$, $\theta_{min} = -\frac{3}{8}\pi$, $\theta_{max} = \frac{\pi}{8}$. The fibers rotate counterclockwise from epicardium to endocardium for a total amount of 120°. The axially symmetric coefficients of the 3D conductivity tensor are reported in Table 7.1. The external stimulus of $250\frac{mA}{cm^3}$ lasting 0.5 ms is applied in a small volume located at the center of the first quarter of the ventricle. In the IGA discretization, we use NURBS of polynomial degree three with $\mathcal{C}^2$ continuity, even if, in order to obtain our ellipsoidal domain, the knots located at $\phi = \frac{\pi}{2}$ have multiplicity two. For this reason, we cannot solve the linear system with a minimal overlap and we choose to apply the 1-level OAS preconditioner with overlap $r = 1$. The fine mesh is $24 \times 16 \times 4$ while the number of subdomains is $24 = 6 \times 4 \times 1$. It is well known that the Monodomain system is quite better conditioned than the Bidomain system. However, the conditioning of both systems worsen on deformed domains and using an overlapping preconditioner can improve the performance considerably. The number of PCG iterations per time step and the condition number of the preconditioned operator are reported in Table 7.2, which compares the variation of the condition
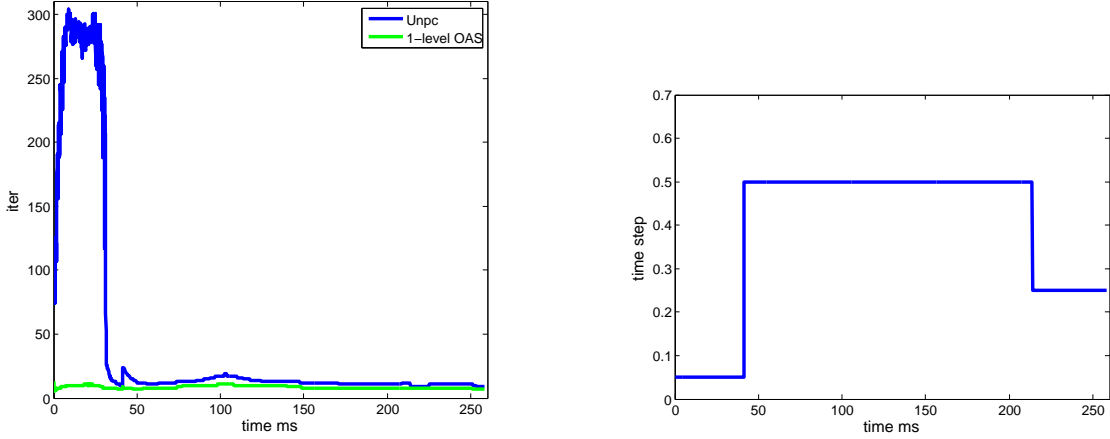
Figure 7.1: Time course of PCG iteration counts (left) and time step size (right) during a complete heartbeat: comparison between unpreconditioned CG (left) and 1-level OAS PCG (right) by solving the Monodomain-LR1 model with a fine mesh $24 \times 16 \times 4$ and $6 \times 4 \times 1$ subdomains.

number during a complete heartbeat (300 ms) by using 1-level OAS PCG and unpreconditioned CG. This variation is strictly related to the time step size (Δt), that changes according to the adaptive strategy described in Chapter 5, as shown in Fig. 7.1, and follows the different phases of the ventricular action potential. We remark that the depolarization phase is computationally the most intense; nevertheless 1-level OAS keeps the condition numbers quite uniform for the whole duration of the cycle, see Table 7.2.

In Fig. 7.2, we show some isochrones of the activation and repolarization time on our half ventricle. The activation time is defined at each quadrature point **x** as

Phase	Unpc.		1-level OAS	
	it.	κ_2	it.	$\kappa_2 = \lambda_{max}/\lambda_{min}$
phase 0	206	$5.6e3$	9	$\kappa_2 = 4.29/0.77$
phase 1-2	13	24.1	8	$\kappa_2 = 4.29/0.76$
phase 3	10	18.66	7	$\kappa_2 = 4.29/0.77$

Table 7.2: Complete heartbeat simulation of the Monodomain-LR1 model. Comparison between unpreconditioned CG and 1-level OAS PCG with respect to average number of PCG iterations per time step, condition number (κ_2) and extreme eigenvalues ($\lambda_{max}, \lambda_{min}$).

	Unpc.		1-level OAS		2-level OAS	
N	it.	k_2	it.	$k_2 = \lambda_{max}/\lambda_{min}$	it.	$k_2 = \lambda_{max}/\lambda_{min}$
$2 \times 2 \times 1$	175	$4.98e3$	21	$65 = 4.0/6.09e-2$	12	11.07=4.74/4.12e-1
$3 \times 3 \times 2$	185	$4.44e3$	44	$331 = 8.0/2.41e-2$	22	32.13=8.60/2.72e-1
$4 \times 4 \times 3$	206	$6.32e3$	61	$627 = 8.0/1.27e-2$	23	31.90=8.63/2.73e-1
$5 \times 5 \times 4$	247	$8.89e3$	78	$1020 = 8.0/7.8e-3$	23	32.09=8.64/2.69e-1
$6 \times 6 \times 5$	297	$1.2e4$	94	$1507 = 8.0/5.3e-3$	23	31.60=8.64/2.27e-1

Table 7.3: Bidomain-LR1 OAS preconditioners on a 3D ellipsoidal domain. Scalability test: condition number (κ_2), values of the extreme eigenvalues ($\lambda_{max}, \lambda_{min}$) and iteration counts (it.) as a function of the number of subdomains N, for fixed $H/h = 4$, $p = 3$, $k = 2$ and $r = 0$. Unpreconditioned CG (left), 1-level OAS (middle) and 2-level OAS (right) preconditioners.

the unique time instant t_a during the upstroke phase of the action potential such that $v_M(\mathbf{x}, t_a) = -50$mV; similarly, the repolarization time is the unique time instant t_r after the upstroke such that $v_M(\mathbf{x}, t_a) = -65$mV.

7.2   Bidomain–LR1 model: scalability test

We now consider the Bidomain model described in Sec. 3.1 and perform 30 time steps of 0.05 ms each, solving iteratively the discrete Bidomain system at each time step by unpreconditioned CG and the 1-level and 2-level OAS PCG. We consider the 3D NURBS domain shown in Fig.7.3, decomposed into an increasing number of subdomains (from $2 \times 2 \times 1$ to $6 \times 6 \times 5$). We choose the IGA fine and subdomain mesh sizes such that their ratio is kept fixed at $\frac{H}{h} = 4$, and we fix $p = 3$, $k = 2$ and the minimal overlap $r = 0$. Table 7.3 shows that, as expected, unpreconditioned CG and 1-level OAS preconditioner (without a coarse problem) have condition numbers growing with N, while the 2-level OAS preconditioner is essentially scalable. Additional results, for $p = 3, 2$ and $k = p - 1$, are plotted in Fig.7.4; they confirm that the 2-level preconditioner is optimal, and that κ_2 grows linearly with an increasing ratio $\frac{H}{h}$.

We now consider the same NURBS domain of Fig 7.3, and increase the overlap index r for the 2-level OAS preconditioner. The results reported in Table 7.4 confirm that the condition number and the iteration counts improve with increasing r, except in case of generous overlap, $r = p$, because the excessive overlap size between subdomains increases considerably the maximal eigenvalue λ_{max} (as
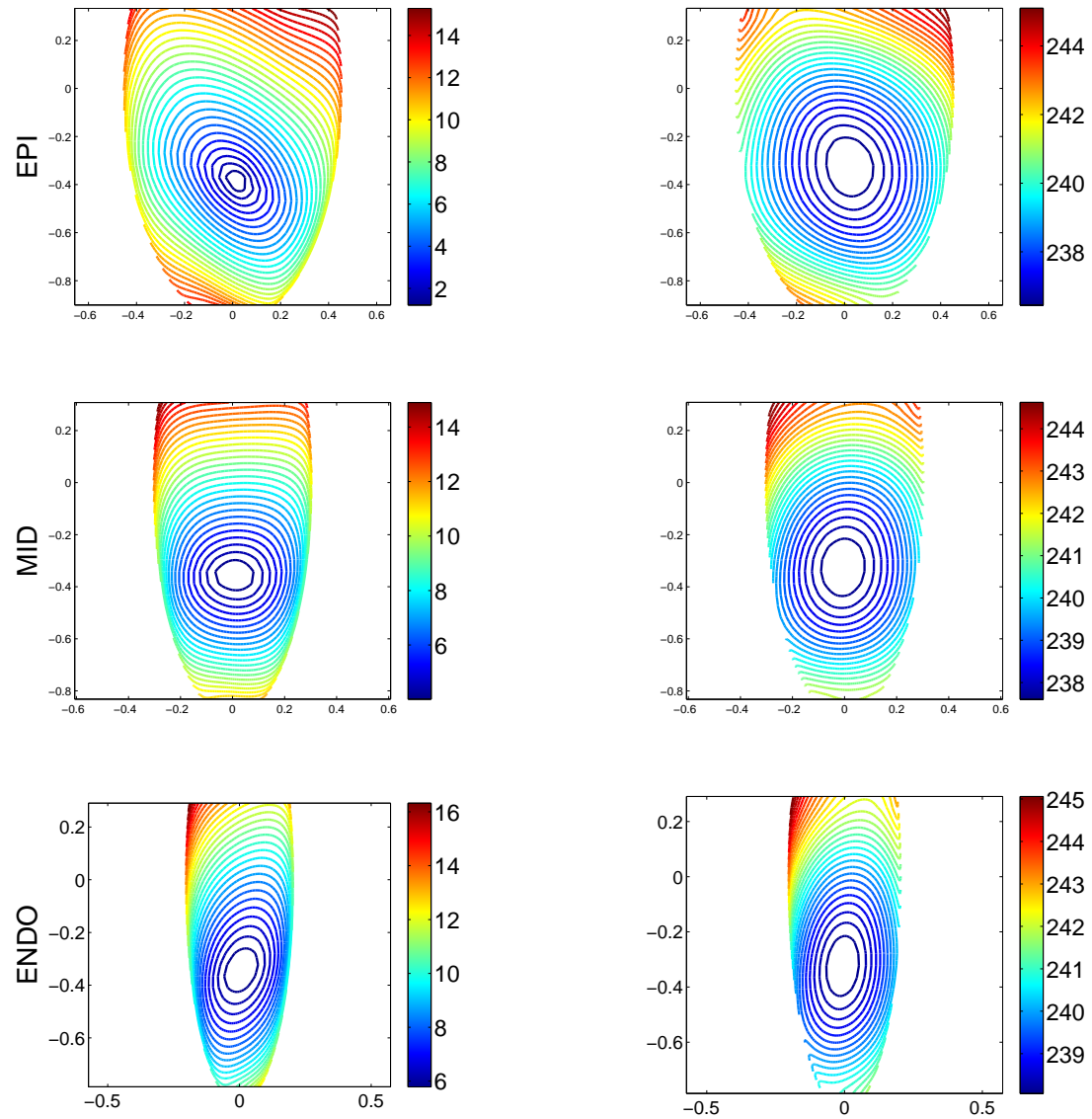
Figure 7.2: Epicardial view (upper panels), midwall view (center) and endocardial view (lower panels) of the activation (left column) and repolarization (right column) time contourplot, computed by solving the Monodomain-LR1 model with 1-level OAS PCG with a fine mesh $24 \times 16 \times 4$ and $6 \times 4 \times 1$ subdomains. The colorbar denotes the range of values displayed on the surface.
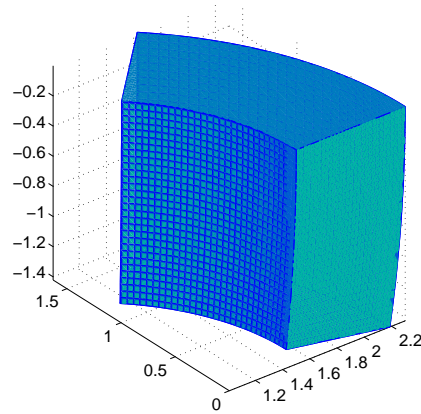
Figure 7.3: NURBS domain for scalability tests, given in ellipsoidal coordinates with parameters a1=b1=1.5 a2=b2=2.3 c1=4.2 c2=4,6 all in cm and $\phi_{min} = 0$, $\phi_{max} = \frac{\pi}{4}$, $\theta_{min} = -\frac{\pi}{10}$, $\theta_{max} = 0$.

Figure 7.4: Optimality of 2-level OAS preconditioner for the Bidomain-LR1 model: plot of the condition number as a function of $\frac{H}{h}$, for $p = 2, 3$ and $k = p - 1$.

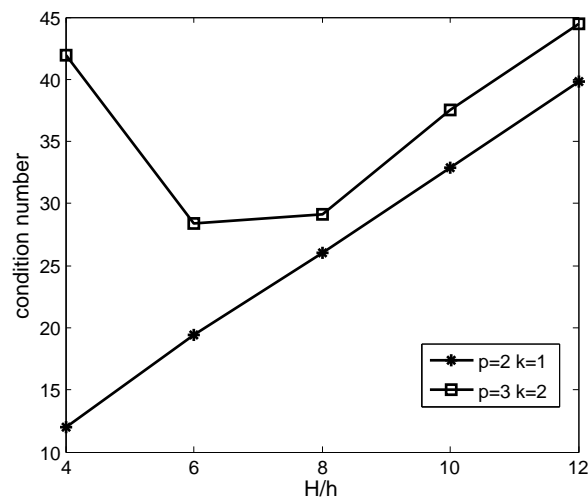| N | 2-level OAS | | | | | |
| | it. | $\kappa_2 = \lambda_{max}/\lambda_{min}$ | it. | $\kappa_2 = \lambda_{max}/\lambda_{min}$ | it. | $\kappa_2 = \lambda_{max}/\lambda_{min}$ |
	\multicolumn{2}{c}{r=0}	\multicolumn{2}{c}{r=1}	\multicolumn{2}{c}{r=p}	
$2 \times 2 \times 1$	16	11.07=4.74/4.28e-1	13	11.69=4.99/4.27e-1	10	6.23=4.99/8.0e-1
$3 \times 3 \times 2$	29	32.83=8.59/2.2.62e-1	21	14.07=9.99/7.1e-1	22	18.74=18.74/1.00
$4 \times 4 \times 3$	30	33.79=8.61/2.54e-1	22	15.88=10.37/6.53e-1	22	19.63=19.89/1.01
$5 \times 5 \times 4$	32	33.91=8.61/2.54e-1	30	16.96=10.43/6.4e-1	29	30.07= 31.28/1.04

Table 7.4: Bidomain-LR1 OAS preconditioner on a 3D ellipsoidal domain. Scalability test: condition number (κ_2), extreme eigenvalues ($\lambda_{max}, \lambda_{min}$) and iteration counts (it.) as a function of the number of subdomains N for fixed $H/h = 4$ and 2-level OAS preconditioners with different overlap index $r = 0, 1, p$.

predicted by the coloring argument in the abstract Schwarz theory upper bound).

Table 7.5 illustrates another test performed by increasing the number of sub-domains from $N = 4$ to $N = 144$, in order to form increasing ellipsoidal domains Ω (depicted above the table), while the fine mesh is chosen so as to keep the ratio $\frac{H}{h} = 4$ fixed. For these tests we choose a random right hand side and a zero initial guess. The numerical results confirm the scalability of the 2-level OAS precon-ditioner and the non-scalability of both 1-level OAS and unpreconditioned CG.

In Table 7.6, we study the performance of 2-level OAS for increasing polynomial degree p from 2 up to 7 in the IGA Bidomain-LR1 discretization with $1/h = 32$, $N \times N = 2 \times 2$, using both minimal and generous overlap. 2-level OAS with generous overlap ($r = p$) performs much better than with minimal overlap since its condition numbers and iteration counts seem to be bounded by a constant independent of the polynomial degree p.

7.3 Discontinuous conductivity coefficients

We now investigate the robustness of the OAS preconditioner with respect to jumps discontinuities of the conductivity coefficients. Similar Bidomain tests were carried out for the BBDC methods in [83] and for AMG preconditioners in [63]. We consider a quarter of truncated ellipsoid decomposed into $6 \times 6 \times 2$ subdomains, and we vary the magnitude of the Bidomain conductivity coefficients $\sigma_{t,l,n}^{I,E}$ by seven
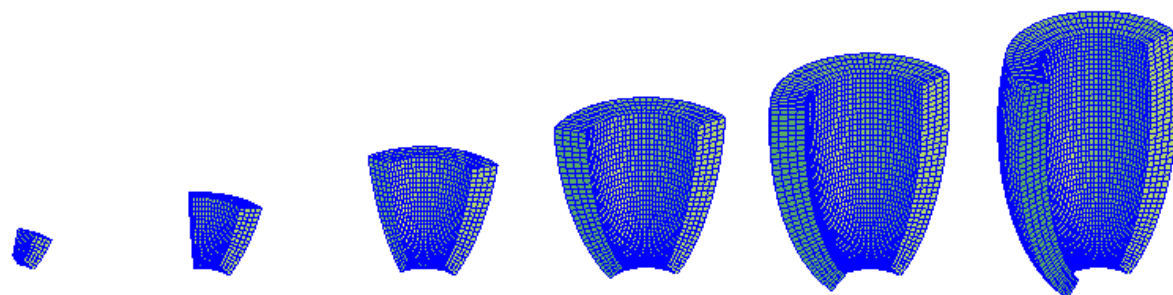
N	Unpc.		1-level OAS		2-level OAS	
	it.	k_2	it.	$\kappa_2 = \lambda_{max}/\lambda_{min}$	it.	$\kappa_2 = \lambda_{max}/\lambda_{min}$
$2 \times 2 \times 1$	765	$2.85e4$	14	$10.34 = 4.0/3.87e-1$	11	5.72=4.98/8.71e-1
$4 \times 4 \times 1$	1236	$4.92e4$	27	$58.61 = 4.82/8.23e-2$	10	6.62=5.05/7.62e-1
$6 \times 6 \times 1$	1539	$7.30e4$	35	$1.42e2 = 4.88/3.44e-2$	9	6.27=5.04/8.04e-1
$8 \times 8 \times 1$	1949	$1.01e5$	47	$2.66e2 = 4.86/1.83e-2$	8	5.53=4.95/8.95e-1
$10 \times 10 \times 1$	2180	$1.14e5$	55	$4.52e2 = 8.0/1.08e-2$	8	5.50=4.95/9.01e-1
$12 \times 12 \times 1$	2307	$1.25e5$	63	$6.67e2 = 4.87/7.30e-3$	8	5.50=4.95/9.01e-1

Table 7.5: Bidomain-LR1 OAS scalability tests on increasing ellipsoidal domains: condition numbers (κ_2), extreme eigenvalues ($\lambda_{max}, \lambda_{min}$) and iteration counts (it.) as a function of the number of subdomains N for fixed $H/h = 4$, $p = 3$, $k = 2$ and minimal overlap $r = 0$. Unpreconditioned CG (left), 1-level (middle) and 2-level (right) OAS preconditioners.

	2-level OAS			
	r=0		r=p	
p	it.	$k_2 = \lambda_{max}/\lambda_{min}$	it.	$k_2 = \lambda_{max}/\lambda_{min}$
2	9	3.8=4.04/1.06	9	3.833=4.28/1.12
3	12	8.61=4.09/0.47	10	4.55=4.69/1.03
5	14	25.25=4.20/1.66e-1	12	4.94=4.97/1.01
7	19	112.26=4.36/3.8e-2	12	4.82=4.99/1.03

Table 7.6: Bidomain-LR1 OAS preconditioner in 2D parametric domain: condition numbers (κ_2), extreme eigenvalues ($\lambda_{max}, \lambda_{min}$) and iteration counts (it.) as a function of the spline polynomial degree p, for minimal and maximal overlap. Fixed $1/h = 32$, $N \times N = 2 \times 2$.
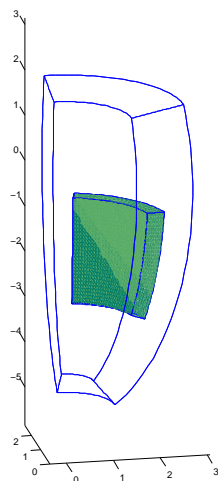
Figure 7.5: Ellipsoidal domain for the discontinuous conductivity coefficients in the Bidomain-LR1 model: in the green region the conductivity coefficients are multiplied by a factor $\rho = 10^i$, $i = -5, -4, \ldots, 1, 2$

order of magnitude (from 10^{-5} to 10^2) only in a central layer, corresponding to a central part of the midwall, as shown in Fig. 7.5.

Table 7.7 reports the condition number, extreme eigenvalues and iteration count for unpreconditioned CG and 2-level OAS. The results show that the condition number is independent of the coefficient jumps, even if these jumps are located inside the subdomains. Since the conductivity coefficients in the definition of the tensor are of the order of 10^{-3}, a multiplication for $\rho < 10^{-3}$ simulates a region of no conduction, as depicted in Fig. 7.6, reporting the activation times for a Bidomain-LR1 2D simulation on a slab $[0, 1]^2$ with a stimulus delivered at the center of the domain, and with a region of discontinuous conductivity coefficients located at $[0.25, 0.45] \times [0.25, 0.75]$.

	unpc		2-level OAS	
ρ	it.	k_2	it.	$\kappa_2 = \lambda_{max}/\lambda_{min}$
10^{-5}	668	$1.6e5$	20	$35.11 = 8.56/0.24$
10^{-4}	659	$1.52e5$	20	$35.12 = 8.56/0.24$
10^{-3}	519	$0.56e5$	20	$35.11 = 8.56/0.24$
10^{-2}	613	$1.08e5$	20	$35.10 = 8.56/0.24$
10^{-1}	466	$0.40e5$	20	$34.70 = 8.46/0.24$
1	420	$0.29e5$	20	$35.09 = 8.61/0.24$
10^1	382	$0.24e5$	20	$32.70 = 8.63/0.26$
10^2	395	$0.25e5$	20.	$25.66 = 8.65/0.34$

Table 7.7: 2-level OAS and unpreconditioned CG iteration counts and condition numbers in presence of jump discontinuities of magnitude ρ in the Bidomain conductivity coefficients. IGA discretization with $N = 6 \times 6 \times 2$ subdomains and $\frac{H}{h} = 4$, $p = 3$, $k = 2$.
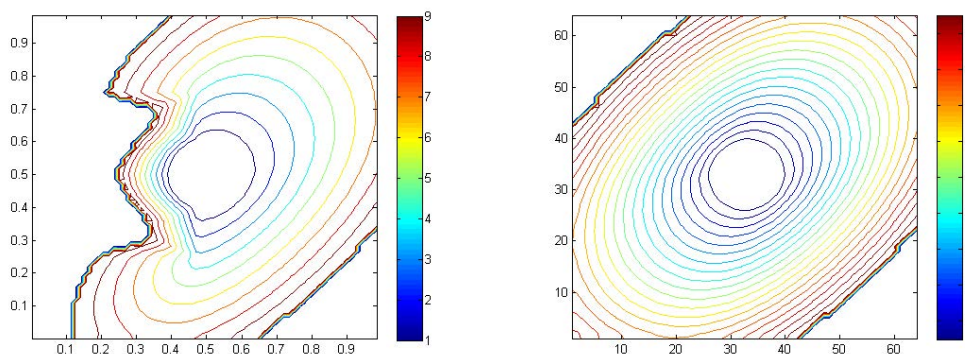

Figure 7.6: Activation time isochrones for a Bidomain - LR1 test with a central region of discontinuous conductivity coefficients with $\rho = 10^{-3}$ (left panel) and without discontinuities (right panel).

7.3.1 Transmural ischemia

We solve the Bidomain-LR1 model with 2-level OAS preconditioner, on the ellipsoidal domain in Fig. 7.3, with a transmura ischemic region of dimensions located at the center.

Ischemia is a restriction in bloody supply to tissue. The three main pathophysiological conditions of myocardial ischaemia are elevated extracellular potassium, acidosis and anoxia, whose effects on membrane potential are elevation of resting potential and reduction of upstroke velocity and action potential duration (APD). We can distinguish three stages of ischemia: moderate, corresponding to the first 5-7 minutes, with an elevation of extracellular potassium $[K^+]_o$ to about 10 mM; early severe, after 10-12 minutes, with a second increase of $[K^+]_o$; and severe, characterized by the occurrence of gap junction uncoupling and irreversible cell damage.

We simulate an excitation process starting by applying a stimulus of 200 $\mu A/cm^3$ for 0.5 ms on a small area at the center of the epicardium. As proposed in [19], the ischemic condition is modelled by increasing the extracellular concentration of potassium in the LR1 model from 5.4 mM (control) to 10.5 mM (moderate) to 20 mM (severe) and reducing the conductivity coefficients in the ischemic region as indicated in Table 7.8 (see [38]), hence the conductivity coefficients present discontinuities on the boundaries of the ischemic region.

Normal tissue	
$\sigma_l^I = 3 \cdot 10^{-3} \Omega^{-1} cm^{-1}$	$\sigma_l^E = 2 \cdot 10^{-3} \Omega^{-1} cm^{-1}$
$\sigma_t^I = 3.1525 \cdot 10^{-4} \Omega^{-1} cm^{-1}$	$\sigma_t^E = 1.3514 \cdot 10^{-3} \Omega^{-1} cm^{-1}$
$\sigma_n^I = 3.1525 \cdot 10^{-5} \Omega^{-1} cm^{-1}$	$\sigma_n^E = 6.757 \cdot 10^{-4} \Omega^{-1} cm^{-1}$
Ischemic tissue	
$\sigma_l^I = 3 \cdot 10^{-4} \Omega^{-1} cm^{-1}$	$\sigma_l^E = 1 \cdot 10^{-3} \Omega^{-1} cm^{-1}$
$\sigma_t^I = 6.305 \cdot 10^{-6} \Omega^{-1} cm^{-1}$	$\sigma_t^E = 3.3785 \cdot 10^{-4} \Omega^{-1} cm^{-1}$
$\sigma_n^I = 6.305 \cdot 10^{-7} \Omega^{-1} cm^{-1}$	$\sigma_n^E = 1.6892 \cdot 10^{-4} \Omega^{-1} cm^{-1}$

Table 7.8: Conductivity coefficients used in the numerical simulation of transmural ischemia.

Accoording to the previous test, the condition number is independent of coefficients jumps, as reported in Table 7.9 .

Fig. 7.7 and Fig. 7.8 report the isochrones of activation, repolarizatione and APD= $t_r - t_a$ on epicardium, midwall and endocardium in normal condition and

	it.	2-level OAS $\kappa_2 = \lambda_{max}/\lambda_{min}$
Control	23	$31.44 = 8.64/0.27$
Moderate	23	$31.10 = 8.64/0.28$
Severe	23	$33.58 = 8.64/0.25$

Table 7.9: 2-level OAS iteration counts and condition numbers in case of control and ischemia (moderate and severe). IGA discretization with $N = 6 \times 6 \times 5$ subdomains and $\frac{H}{h} = 4$, $p = 3$, $k = 2$.

in case of a severe ischemia. We can observe the effects on the spread of excitation and repolarization of an ischemia. On epicardial plane isochrones of activation are elliptical with the major axis along the fiber direction, becoming rounded proceeding on the ischemic section. Repolarization starts first at the center of the ischemic area, and the APD distribution show a minimum in the region repolarized first.
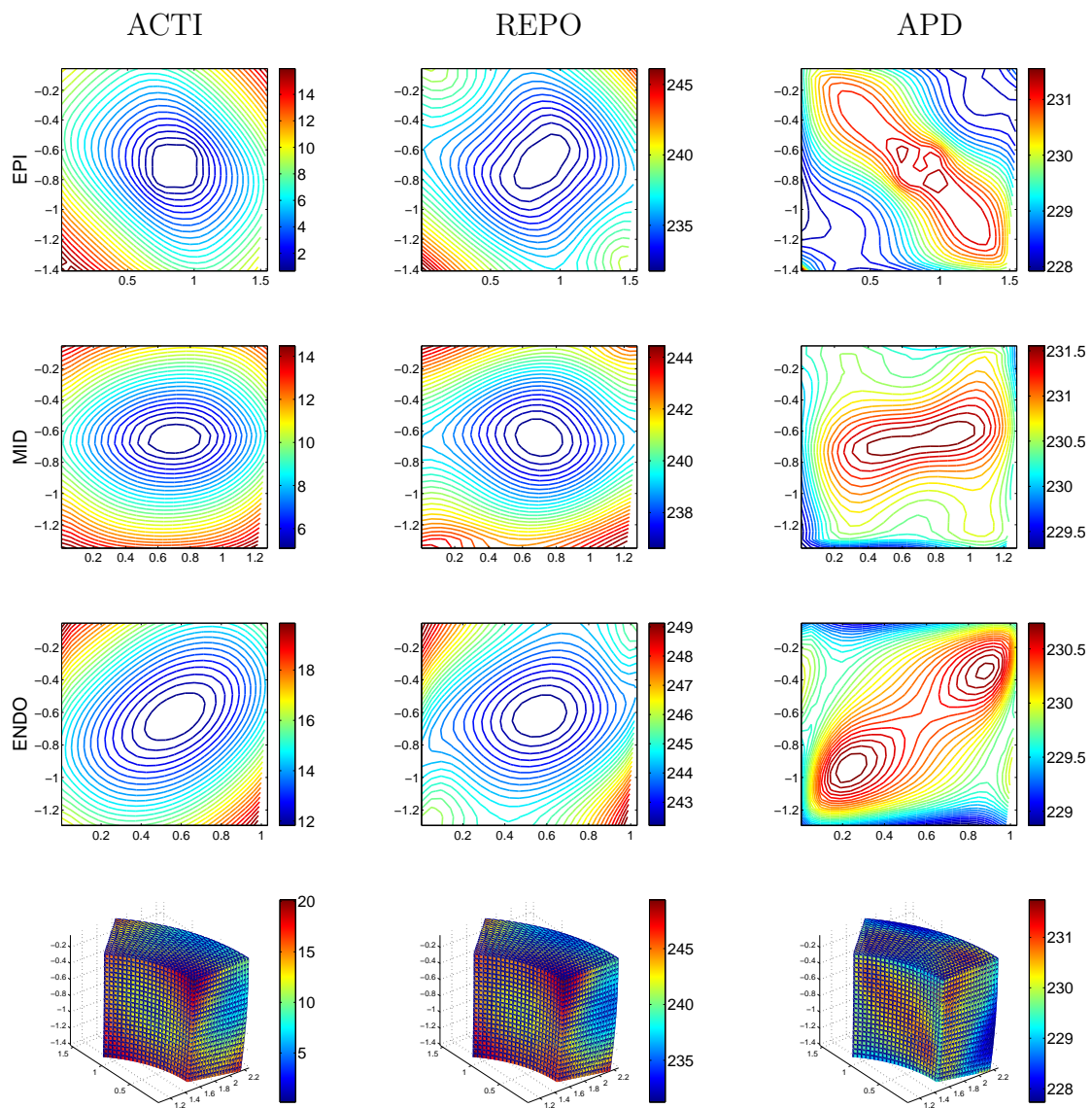
Figure 7.7: Epicardial view (first row) midwall view (second row) and endocardial view (third row) and 3d view of the activation (left column) repolarization (center) and APD (rigth column) isochrones in presence of severe ischemia, computed by solving the Bidomain-LR1 model with 2-level OAS PCG with a fine mesh $24 \times 24 \times 20$ and $6 \times 6 \times 5$ subdomains, $p = 3$, $k = 2$. The colorbar denotes the range of values displayed on the surface.

Figure 7.8: Epicardial view (first row) midwall view (second row) and endocardial view (third row) and 3d view of the activation (left column) repolarization (center) and APD (rigth column) isochrones in presence of severe ischemia, computed by solving the Bidomain-LR1 model with 2-level OAS PCG with a fine mesh $24 \times 24 \times 20$ and $6 \times 6 \times 5$ subdomains, $p = 3$, $k = 2$. The colorbar denotes the range of values displayed on the surface.
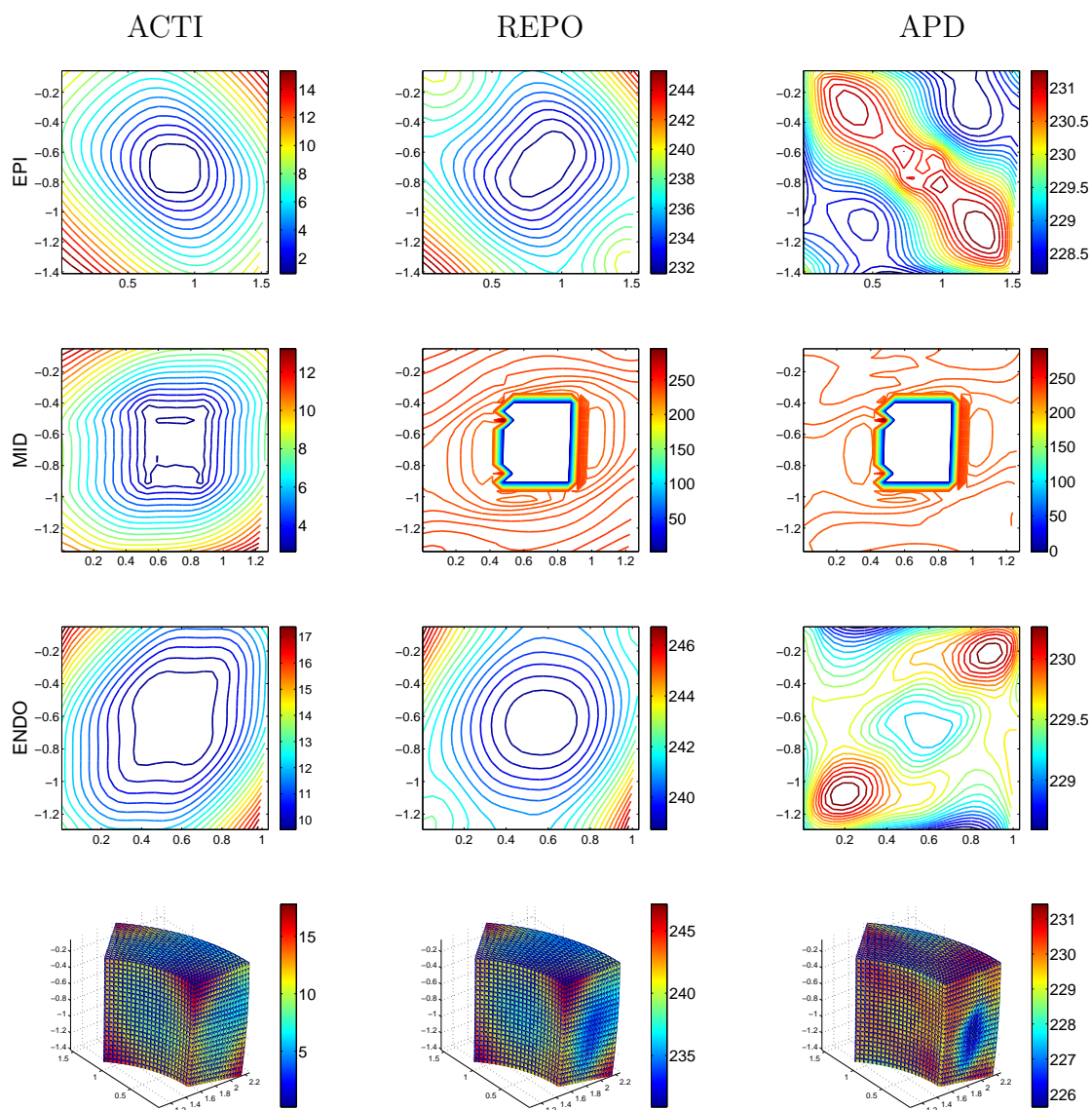
7.4 Conclusions

We have developed 2-level overlapping additive Schwarz preconditioners for the Bidomain system discretized by NURBS-based IGA. In Chapter 6, we have proved that the resulting solvers are scalable and have an optimal convergence rate depending linearly on the ratio $\frac{H}{\delta}$, between the subdomain and the overlap sizes. The results of three dimensional numerical tests have confirmed our convergence rate bound analysis. The simulations have shown that the good convergence properties hold for discontinuous conductivity coefficients, which could be present in some pathological phenomena involving for example ischemic regions inside the cardiac tissue.

The promising results that we have obtained encourage future developments such as:

- extension of $h-$version analysis of the convergence rate bound to $p-$analysis;

- extending the 2-level additive algorithms and IGA analysis to 2-level multiplicative and hybrid versions;

- the construction and analysis of non-overlapping domain decomposition IGA solvers, in particular BDDC and FETI-DP preconditioners, for the Bidomain system;

- the study of coarse solvers based not only on $h-coarsening$ but also on $p-coarsening$, i.e. employing a polynomial degree p lower than the degree of the NURBS approximation space;

- the parallel implementation of the solvers studied in the this thesis using parallel machines with distributed memory (possibly including the latest accelerators based on GPU and Phi processors);

- the use of *multipatch* NURBS geometries, allowing us to represent for example an idealized biventricular heart as in Fig. 7.9 and to investigate the spread of excitation in a more realistic and complete cardiac geometry.
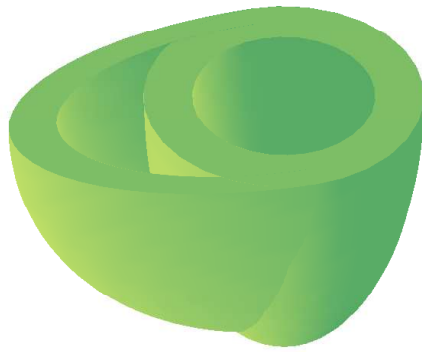
Figure 7.9: Idealized biventricular geometry obtained from ellipsoidal patches.

Appendix A

Luo-Rudy I ventricular model

Luo-Rudy model equations:

Fast Na^+ current (I_{Na})

$$I_{Na} = g_{Na}m^3 \ h \ j \ (v - E_{Na})$$

where $g_{Na} = 23$ mS/cm^2, $E_{Na} = 54.4$ mV, and the gating variables m, h, j satisfy ordinary differential equations (2.4) with coefficients

$$\alpha_m = 0.32 \ \frac{47.13 + v}{1 - \exp(-47.13 - v)}, \qquad \beta_m = 0.08 \exp\left(\frac{-v}{11}\right),$$

$$\alpha_h = \begin{cases} 0 & v \geq -40 \\ 0.135 \exp(0.079 \ v) + 3.1 \cdot 10^5 \exp(0.35 \ v) & v < -40, \end{cases}$$

$$\beta_h = \begin{cases} 0.13 \left(1 + \exp\left(\frac{10.66 + v}{-11.1}\right)\right) & v \geq -40 \\ 3.56 \exp(0.079 \ v) + 3.1 \cdot 10^5 \exp(0.35 \ v) & v < -40, \end{cases}$$

$$\alpha_j = \begin{cases} 0 & v \geq -40 \\ -1.2714 \cdot 10^5 \exp(0.244 \ v) - 3.474 \cdot 10^5 \exp(-0.04391 \ v) & v < -40, \end{cases}$$

$$\beta_j = \begin{cases} 0.3\dfrac{\exp(-2.535 \cdot 10^{-7}v)}{1 + \exp(-0.1(32 + v))} & v \geq -40 \\ 0.1212\dfrac{\exp(-0.01052 \ v)}{1 + \exp(-0.1378(40.14 + v))} & v < -40. \end{cases}$$

Slow inward current (I_{si})

$$I_{si} = g_{si}d\,f\,(v - E_{si}),$$

where $g_{si} = 0.09mS/cm^2$, $E_{si} = 7.7 - 13.0287\log([Ca]_i)$, $[Ca]_i$ is the intracellular calcium concentration satisfying the ordinary differential equation

$$\frac{\mathrm{d}\,[Ca]_i}{\mathrm{d}t} = 0.07\left(10^{-4} - [Ca]_i\right) - 10^{-4}I_{si},$$

and d, f are gating variables satisfying (2.4) with coefficients

$$\alpha_d = 0.095\frac{\exp\left(-0.01\,(v - 5)\right)}{1 + \exp\left(-0.072\,(v - 5)\right)}, \qquad \beta_d = 0.07\frac{\exp\left(-0.017\,(v + 44)\right)}{1 + \exp\left(0.05\,(v + 44)\right)}$$

$$\alpha_f = 0.012\frac{\exp\left(-0.008\,(v + 28)\right)}{1 + \exp\left(0.15\,(v + 28)\right)}, \qquad \beta_f = 0.0065\frac{\exp\left(-0.02\,(v + 30)\right)}{1 + \exp\left(-0.04\,(v + 20)\right)}.$$

Time-dependent K^+ current (I_K)

$$I_K = g_K X X_i\,(v - E_K),$$

where $g_K = 0.282$ mS/cm^2, $E_K = -77$ mV, X is a gating variable satisfying (2.4) with coefficients

$$\alpha_X = 0.0005\frac{\exp\left(0.083\,(v + 50)\right)}{1 + \exp\left(0.057\,(v + 50)\right)}, \qquad \beta_X = 0.0013\frac{\exp\left(-0.06\,(v + 20)\right)}{1 + \exp\left(-0.04\,(v + 20)\right)},$$

and X_i is an additional variable given by

$$X_i = \begin{cases} 2.837\dfrac{\exp\left(0.04\,(v + 77)\right) - 1}{(v + 77)\exp\left(0.04\,(v + 35)\right)} & v > -100 \\ 1 & v \le -100. \end{cases}$$

Time-independent K^+ current (I_{K1})

$$I_{K1} = g_{K1}K1_\infty\,(v - E_{K1}),$$

where

$$g_{K1} = 0.6047\sqrt{\frac{[K]_0}{5.4}}, \qquad v_{K1} = v_{Na}\frac{\log\left(\dfrac{[K]_0}{[K]_i}\right)}{\log\left(\dfrac{[Na]_0}{[Na]_i}\right)},$$

with the constant ion concentrations $[K]_0 = 5.4, [K]_i = 145, [Na]_0 = 140, [Na]_i = 18$ (all in mM), and

$$K1_\infty = \frac{\alpha_{K1}}{\alpha_{K1} + \beta_{K1}},$$

where

$$\alpha_{K1} = \frac{1.02}{1 + \exp\left(0.2385\left(v - v_{K1} - 59.215\right)\right)},$$

$$\beta_{K1} = \frac{0.49124\exp\left(0.08032\left(v - v_{K1} + 5.476\right)\right) + \exp\left(0.06175\left(v - v_{K1} + 594.31\right)\right)}{1 + \exp\left(-0.5143\left(v - v_{K1} + 4.753\right)\right)}$$

Plateau K^+ current $\left(I_{Kp}\right)$

$$I_{Kp} = g_{Kp}\,K_p\left(v - E_{Kp}\right),$$

where $g_{Kp} = 0.0183$ mS/cm^2, $E_{Kp} = E_{K1}$ and

$$K_p = \frac{1}{1 + \exp\left(\left(7.488 - v\right)/5.98\right)}$$

Background current I_b

$$I_b = g_b\left(v - E_b\right),$$

where $g_b = 0.03921$ mS/cm^2 and $E_b = -59.87$ mV.

Appendix B

Severi et al. 2012 sinoatrial model

Membrane potential

$$\frac{\mathrm{d}V}{\mathrm{d}t} = -\frac{I_{tot}}{C}$$

$$I_{tot} = I_f + I_{Kr} + I_{Ks} + I_{to} + I_{NaK} + I_{NaCa} + I_{Na} + I_{CaL} + I_{CaT} + I_{KACh}$$

Ion Currents

x_∞ : Steady-state curve for a gating variable x

τ_x : Time constant for a gating variable x

α_x and β_x : Opening and closing rates for channel gating

Hyperpolarization-activated, "funny" current (I_f)

$$I_f = (I_{fNa} + I_{fK})$$

$$I_{fNa} = \frac{y^2 \cdot Ko}{Ko + Km_f} \cdot g_{fNa} \cdot (V - E_{Na}) \qquad I_{fK} = \frac{y^2 \cdot Ko}{Ko + Km_f} \cdot g_{fK} \cdot (V - E_K)$$

with $g_{fNa} = g_{fK} = 0.03\,\mu\text{S}$, $Km_f = 45$ mM, and y is the gating variable of activation satisfying (2.7) with coefficients

$$y_\infty = \frac{1}{1 + e^{\frac{V + 52.5}{9}}}$$

$$\tau_y = \frac{0.7}{0.0708 \cdot e^{\frac{-(V+5)}{20.28}} + 10.6 \cdot e^{\frac{V}{18}}}.$$

L-type Ca^{2+} current (I_{CaL})

$$I_{CaL} = (I_{siCa} + I_{siK} + I_{siNa})$$

$$I_{siCa} = \frac{2 \cdot P_{CaL} \cdot V}{\frac{RT}{F} \cdot \left(1 - e^{\frac{-2 \cdot V}{RT/F}}\right)} \cdot \left(Ca_{sub} - Ca_o \cdot e^{\frac{-2 \cdot V}{RT/F}}\right) \cdot dL \cdot fL \cdot fCa$$

$$I_{siK} = \frac{0.000365 \cdot P_{CaL} \cdot V}{\frac{RT}{F} \cdot \left(1 - e^{\frac{-V}{RT/F}}\right)} \cdot \left(Ki - Ko \cdot e^{\frac{-V}{RT/F}}\right) \cdot dL \cdot fL \cdot fCa$$

$$I_{siNa} = \frac{0.0000185 \cdot P_{CaL} \cdot V}{\frac{RT}{F} \cdot \left(1 - e^{\frac{-V}{RT/F}}\right)} \cdot \left(Na_i - Na_o \cdot e^{\frac{-V}{RT/F}}\right) \cdot dL \cdot fL \cdot fCa$$

with $P_{CaL} = 0.2$ nA/mM whereas dL, fL and fCa are the gating variables of activation, inactivation and inactivation calcium-dependent, respectively, satisfying (2.7) with coefficients

$$dL_\infty = \frac{1}{1 + e^{\frac{-(V+20.3)}{4.2}}} \qquad \tau_{dL} = \frac{0.001}{\alpha_{dL} + \beta_{dL}}$$

$$\alpha_{dL} = \frac{-0.02839 \cdot (V + 41.8)}{e^{\frac{-(V+41.8)}{2.5}} - 1} - \frac{0.0849 \cdot (V + 6.8)}{e^{\frac{-(V+6.8)}{4.8}} - 1}$$

$$\beta_{dL} = \frac{0.01143 \cdot (V + 1.8)}{e^{\frac{V+1.8}{2.5}} - 1}$$

$$fL_\infty = \frac{1}{1 + e^{\frac{V + 37.4}{5.3}}} \qquad \tau_{fL} = 0.001 \cdot \left(44.3 + 230 \cdot e^{-\left(\frac{V + 36}{10}\right)^2} \right)$$

$$fCa_\infty = \frac{Km_{fCa}}{Km_{fCa} + Ca_{sub}} \qquad \tau_{fCa} = \frac{0.001 \cdot fCa_\infty}{\alpha_{fCa}}$$

T-type Ca^{2+} current (I_{CaT})

$$I_{CaT} = \frac{2 \cdot P_{CaT} \cdot V}{\frac{RT}{F} \cdot \left(1 - e^{\frac{-2 \cdot V}{\frac{RT}{F}}} \right)} \cdot \left(Ca_{sub} - Ca_o \cdot e^{\frac{-2 \cdot V}{\frac{RT}{F}}} \right) \cdot dT \cdot fT$$

with $P_{CaT} = 0.2$ nA/mM whereas dT, fT are the gating variables of activation and inactivation, respectively, satisfying (2.7) with coefficients

$$dT_\infty = \frac{1}{1 + e^{\frac{-(V + 38.3)}{5.5}}}$$

$$\tau_{dT} = \frac{0.001}{1.068 \cdot e^{\frac{V + 38.3}{30}} + 1.068 \cdot e^{\frac{-(V + 38.3)}{30}}}$$

$$fT_\infty = \frac{1}{1 + e^{\frac{V + 58.7}{3.8}}}$$

$$\tau_{fT} = \frac{1}{16.67 \cdot e^{\frac{-(V + 75)}{83.3}} + 16.67 \cdot e^{\frac{V + 75}{15.38}}}$$

Rapidly activating delayed rectifier K^+ current (I_{Kr})

$$I_{Kr} = g_{Kr} \cdot (V - E_K) \cdot (0.9 \cdot paF + 0.1 \cdot paS) \cdot pi$$

with $g_{Kr} = 0.00021637\ \mu\mathrm{S}$, where paF and paS are the gating variables of fast and slow inactivation, respectively, while pi is the inactivation variable. All the gating variables satisfy (2.7) with coefficients

$$pa_\infty = \cfrac{1}{1 + e^{\frac{-(V+14.8)}{8.5}}}$$

$$\tau_{paF} = \cfrac{1}{30 \cdot e^{\frac{V}{10}} + e^{\frac{-V}{12}}} \qquad \tau_{paS} = \cfrac{0.84655}{4.2 \cdot e^{\frac{V}{17}} + 0.15 \cdot e^{\frac{-V}{21.6}}}$$

$$\frac{\mathrm{d}paS}{\mathrm{d}t} = \frac{pa_\infty - paS}{\tau_{paS}}$$

$$\dot{pi}_\infty = \cfrac{1}{1 + e^{\frac{V+28.6}{17.1}}} \qquad \tau_{pi} = \cfrac{1}{100 \cdot e^{\frac{-V}{54.645}} + 656 \cdot e^{\frac{V}{106.157}}}$$

Slowly activating delayed rectifier K^+ current (I_{Ks})

$$I_{Ks} = g_{Ks} \cdot (V - E_K) \cdot n^2$$

with $g_{Ks} = 0.001657\ \mu\mathrm{S}$ and n is a gating variable of activation satisfying (2.7) with coefficients

$$n_\infty = \cfrac{\cfrac{14}{1 + e^{\frac{-(V-40)}{9}}}}{\cfrac{14}{1 + e^{\frac{-(V-40)}{9}}} + 1 \cdot e^{\frac{-V}{45}}}$$

$$\tau_n = \cfrac{1}{\cfrac{28}{1 + e^{\frac{-(V-40)}{3}}} + e^{\frac{-(V-5)}{25}}}$$

Ach-activated K^+ current (I_{KACh})

$$
I_{KACh} = \begin{cases} g_{KACh} \cdot (V - E_K) \cdot \left(1 + e^{\frac{V + 20}{20}} \right) \cdot a, & \text{if } ACh > 0 \\ 0, & \text{otherwise} \end{cases}
$$

with $g_{KACh} = 0.00864 \, \mu S$ and a is a gating variable satisfying (2.4) with coefficients

$$
a_\infty = \frac{\alpha_a}{\alpha_a + \beta_a}
$$

$$
\alpha_a = \frac{3.5988 - 0.0256}{1 + \frac{0.0000012155}{(1 \cdot ACh)^{1.6951}}} + 0.0256
$$

$$
\beta_a = 10 \cdot e^{0.0133 \cdot (V + 40)}
$$

$$
\tau_a = \frac{1}{\alpha_a + \beta_a}
$$

Transient outward K^+ current (I_{to})

$$
I_{to} = g_{to} \cdot (V - E_K) \cdot q \cdot r
$$

with $g_{to} = 0.002 \, \mu S$ and q and r are the gating variables of activation and inactivation, respectivey satisfying (2.7) with coefficients

$$
q_\infty = \frac{1}{1 + e^{\frac{V + 49}{13}}}
$$

$$
\tau_q = 0.001 \cdot 0.6 \left(\frac{65.17}{0.57 \cdot e^{-0.08 \cdot (V + 44)} + 0.065 \cdot e^{0.1 \cdot (V + 45.93)}} + 10.1 \right)
$$

$$
r_\infty = \frac{1}{1 + e^{\frac{-(V - 19.3)}{15}}}
$$

$$
\tau_r = 0.001 \cdot 0.66 \cdot 1.4 \cdot \left(\frac{15.59}{1.037 \cdot e^{0.09 \cdot (V + 30.61)} + 0.369 \cdot e^{-0.12 \cdot (V + 23.84)}} + 2.98 \right)
$$

Na^+ **current** (I_{Na})

$$I_{Na} = g_{Na} \cdot m^3 \cdot h \cdot (V - E_{mh})$$

with $g_{Na} = 0.0125$ μS and m and h are gating variables satisfying (2.4) with coefficients

$$E_{mh} = \frac{RT}{F} \cdot \ln \frac{Na_o + 0.12 \cdot Ko}{Na_i + 0.12 \cdot Ki}$$

$$E0_m = V + 41$$

$$\delta_m = 1 \cdot 10^{-5} \text{ mV}$$

$$\frac{\mathrm{d}m}{\mathrm{d}t} = \alpha_m \cdot (1 - m) - \beta_m \cdot m$$

$$\alpha_m = \begin{cases} 2000, \text{ if } |E0_m| < \delta_m \\ \dfrac{200 \cdot E0_m}{1 - e^{-0.1 \cdot E0_m}}, \text{ otherwise} \end{cases}$$

$$\beta_m = 8000 \cdot e^{-0.056 \cdot (V+66)}$$

$$\frac{\mathrm{d}h}{\mathrm{d}t} = \alpha_h \cdot (1 - h) - \beta_h \cdot h$$

$$\alpha_h = 20 \cdot e^{-0.125 \cdot (V+75)}$$

$$\beta_h = \frac{2,000}{320 \cdot e^{-0.1 \cdot (V+75)} + 1}$$

$Na^+ - K^+$ **pump current** (I_{NaK})

$$I_{NaK} = I_{NaK_{max}} \cdot \left(1 + \left(\frac{Km_{Kp}}{Ko} \right)^{1.2} \right)^{-1} \cdot \left(1 + \left(\frac{Km_{Nap}}{Na_i} \right)^{1.3} \right)^{-1} \cdot \left(1 + e^{\frac{-(V - E_{Na} + 110)}{20}} \right)^{-1}$$

$Na^+ - Ca^{2+}$ **exchanger current** (I_{NaCa})

$$I_{NaCa} = \frac{K_{NaCa} \cdot (x2 + \cdot k21 - x1 \cdot k12)}{x1 + x2 + x3 + x4}$$

$$x1 = k41 \cdot k34 \cdot (k23 + k21) + k21 \cdot k32 \cdot (k43 + k41)$$

$$x2 = k32 \cdot k43 \cdot (k14 + k12) + k41 \cdot k12 \cdot (k34 + k32)$$

$$x3 = k14 \cdot k43 \cdot (k23 + k21) + k12 \cdot k23 \cdot (k43 + k41)$$

$$x4 = k23 \cdot k34 \cdot (k14 + k12) + k14 \cdot k21 \cdot (k34 + k32)$$

$$k43 = \frac{Na_i}{K3ni + Na_i}$$

$$k12 = \frac{\frac{Ca_{sub}}{Kci} \cdot e^{\frac{-Qci \cdot V}{\frac{RT}{F}}}}{di}$$

$$k14 = \frac{\frac{\frac{Na_i}{K1ni} \cdot Na_i}{K2ni} \cdot \left(1 + \frac{Na_i}{K3ni}\right) \cdot e^{\frac{Qn \cdot V}{2 \cdot \frac{RT}{F}}}}{di}$$

$$k41 = e^{\frac{-Qn \cdot V}{2 \cdot \frac{RT}{F}}}$$

$$di = 1 + \frac{Ca_{sub}}{Kci} \cdot \left(1 + e^{\frac{-Qci \cdot V}{\frac{RT}{F}}} + \frac{Na_i}{Kcni}\right) + \frac{Na_i}{K1ni} \cdot \left(1 + \frac{Na_i}{K2ni} \cdot \left(1 + \frac{Na_i}{K3ni}\right)\right)$$

$$k34 = \frac{Na_o}{K3no + Na_o}$$

$$k21 = \frac{\frac{Ca_o}{Kco} \cdot e^{\frac{Qco \cdot V}{\frac{RT}{F}}}}{do}$$

$$k_{23} = \frac{\frac{\frac{Na_o}{K1no} \cdot Na_o}{K2no} \cdot \left(1 + \frac{Na_o}{K3no}\right) \cdot e^{\frac{-Qn \cdot V}{2 \cdot \frac{RT}{F}}}}{do}$$

$$k32 = e^{\frac{Qn \cdot V}{2 \cdot \frac{RT}{F}}}$$

$$do = 1 + \frac{Ca_o}{Kco} \cdot \left(1 + e^{\frac{Qco \cdot V}{\frac{RT}{F}}}\right) + \frac{Na_o}{K1no} \cdot \left(1 + \frac{Na_o}{K2no} \cdot \left(1 + \frac{Na_o}{K3no}\right)\right)$$

Ca^{2+} release flux (J_{rel}) from SR via RyRs

$$J_{rel} = ks \cdot O \cdot (Ca_{jsr} - Ca - sub)$$

$$kCaSR = MaxSR - \frac{MaxSR - MinSr}{1 + \left(\frac{EC50_{SR}}{Ca_{jsr}}\right)^{HSR}}$$

$$koSRCa = \frac{koCa}{kCaSr}$$

$$kiSRCa = kiCa \cdot kCaSR$$

$$\frac{dR}{dt} = kim \cdot RI - kiSRCa \cdot Ca_{sub} \cdot R - \left(koSRCa \cdot Ca_{sub}^2 \cdot R - kom \cdot O\right)$$

$$\frac{dO}{dt} = koSRCa \cdot Ca_{sub}^2 \cdot R - kom \cdot O - (kiSRCa \cdot Ca_{sub} \cdot O - kim \cdot I)$$

$$\frac{dI}{dt} = kiSRCa \cdot Ca_{sub} \cdot O - kim \cdot I \left(kom \cdot I - koSRCa \cdot Ca_{sub}^2 \cdot RI\right)$$

$$\frac{dRI}{dt} = kom \cdot I - koSRCa \cdot Ca_{sub}^2 \cdot RI - (kim \cdot RI - kiSRCa \cdot Ca_{sub} \cdot R)$$

Intracellular Ca^{2+} fluxes

J_{diff}: Ca^{2+} diffusion flux from submembrane space to myoplasm;
J_{tr}: Ca^{2+} transfer flux from the network to junctional SR;
J_{up}: Ca^{2+} uptake by the SR.

$$J_{diff} = \frac{Ca_{sub} - Cai}{\tau_{dif_{Ca}}}$$

$$J_{tr} = \frac{Ca_{nsr} - Ca_{jsr}}{\tau_{tr}}$$

$$J_{up} = \frac{P_{up}}{1 + \frac{K_{up}}{Cai}}$$

Ca^{2+} buffering

f_{CMi}: Fractional occupancy of calmodulin by Ca^{2+} in myoplasm
f_{CMs}: Fractional occupancy of calmodulin by Ca^{2+} in subspace
f_{CQ}: Fractional occupancy of calsequestrin by Ca^{2+}
f_{TC}: Fractional occupancy of the troponin-Ca^{2+} site by Ca^{2+}
f_{TCM}: Fractional occupancy of the troponin-Mg^{2+} site by Ca^{2+}
f_{TMM}: Fractional occupancy of the troponin-Mg^{2+} site by Mg^{2+}

$$\frac{\mathrm{d}fCMi}{\mathrm{d}t} = \delta_{fCMi}$$

$$\delta_{fCMi} = kf_{CM} \cdot Cai \cdot (1 - fCMi) - kb_{CM} \cdot fCMi$$

$$\frac{\mathrm{d}fCMs}{\mathrm{d}t} = \delta_{fCMs}$$

$$\delta_{fCMs} = kf_{CM} \cdot Ca_{sub} \cdot (1 - fCMs) - kb_{CM} \cdot fCMs$$

$$\frac{\mathrm{d}fCQ}{\mathrm{d}t} = \delta_{fCQ}$$

$$\delta_{fCQ} = kf_{CQ} \cdot Ca_{jsr} \cdot (1 - fCQ) - kb_{CQ} \cdot fCQ$$

$$\frac{\mathrm{d}fTC}{\mathrm{d}t} = \delta_{fTC}$$

$$\delta_{fTC} = kf_{TC} \cdot cai \cdot (1 - fTC) - kb_{TC} \cdot fTC$$

$$\frac{\mathrm{d}fTMC}{\mathrm{d}t} = \delta_{fTMC}$$

$$\delta_{fTMC} = kf_{TMC} \cdot Cai \cdot (1 - (fTMC + fTMM)) - kb_{TMC} \cdot fTMC$$

$$\frac{\mathrm{d}fTMM}{\mathrm{d}t} = \delta_{fTMM}$$

$$\delta_{fTMM} = kf_{TMM} \cdot Mgi \cdot (1 - (fTMC + fTMM)) - kb_{TMM} \cdot fTMM$$

Dynamics of Ca^{2+} concentrations in cell compartements

$$\frac{\mathrm{d}Cai}{\mathrm{d}t} = \left(\frac{J_{diff} \cdot V_{sub} - J_{up} \cdot V_{nsr}}{V_i} - (CM_{tot} \cdot \delta_{fCMi} + TC_{tot} \cdot \delta_{fTC} + TMC_{tot} \cdot \delta_{fTMC}) \right)$$

$$\frac{\mathrm{d}Ca_{sub}}{\mathrm{d}t} = \left(\frac{J_{rel} \cdot V_{jsr}}{V_{sub}} - \left(\frac{I_{SiCa} + I_{CaT} - 2 \cdot I_{NaCa}}{2 \cdot F \cdot V_{sub}} + J_{Ca_{dif}} + CM_{tot} \cdot \delta_{fCMs} \right) \right)$$

$$\frac{\mathrm{d}Ca_{nsr}}{\mathrm{d}t} = J_{up} - \frac{J_{tr} \cdot V_{jsr}}{V_{nsr}}$$

$$\frac{\mathrm{d}Ca_{jsr}}{\mathrm{d}t} = J_{tr} - (J_{rel} + CQ_{tot} \cdot \delta_{fCQ})$$

Dynamics of intracellular Na^+ concentration

$$\frac{\mathrm{d}Na_i}{\mathrm{d}t} = -\frac{I_{Na} + I_{fNa} + I_{siNa} + 3 \cdot I_{NaK} + 3 \cdot I_{NaCa}}{(V_i + V_{sub}) \cdot F}$$

Bibliography

[1] R. R. Aliev and A. V. Panfilov. A simple two-variable model of cardiac excitation. *Chaos, Solitons & Fractals*, 7(3):293–301, 1996.

[2] C. Altomare, B. Terragni, C. Brioschi, R. Milanesi, C. Pagliuca, C. Viscomi, A. Moroni, M. Baruscotti, and D. DiFrancesco. Heteromeric hcn1–hcn4 channels: a comparison with native pacemaker channels from the rabbit sinoatrial node. *The Journal of physiology*, 549(2):347–359, 2003.

[3] U. M. Ascher, S. J. Ruuth, and B. T. Wetton. Implicit-explicit methods for time-dependent partial differential equations. *SIAM Journal on Numerical Analysis*, 32(3):797–823, 1995.

[4] A. Barbuti, M. Baruscotti, and D. DiFrancesco. The pacemaker current: from basics to the clinics. *Journal of cardiovascular electrophysiology*, 18(3):342–347, 2007.

[5] M. Baruscotti, A. Barbuti, and A. Bucchi. The cardiac pacemaker current. *Journal of molecular and cellular cardiology*, 48(1):55–64, 2010.

[6] Y. Bazilevs, L. Beirao da Veiga, J. Cottrell, T. Hughes, and G. Sangalli. Isogeometric analysis: approximation, stability and error estimates for h-refined meshes. *Mathematical Models and Methods in Applied Sciences*, 16(07):1031–1090, 2006.

[7] Y. Bazilevs, V. M. Calo, J. A. Cottrell, J. A. Evans, T. Hughes, S. Lipton, M. Scott, and T. Sederberg. Isogeometric analysis using t-splines. *Computer Methods in Applied Mechanics and Engineering*, 199(5):229–263, 2010.

[8] G. W. Beeler and H. Reuter. Reconstruction of the action potential of ventricular myocardial fibres. *The Journal of physiology*, 268(1):177–210, 1977.

[9] L. Beirão da Veiga, D. Cho, L. F. Pavarino, and S. Scacchi. Overlapping Schwarz methods for isogeometric analysis. *SIAM J. Numer. Anal.*, 50(3):1394–1416, 2012.

[10] G. Bellettini, P. Colli Franzone, and M. Paolini. Convergence of front propagation for anisotropic bistable reaction–diffusion equations. *Asymptotic Analysis*, 15(3):325–358, 1997.

[11] R. M. Berne, M. N. Levy, and R. M. Berne. *Principles of physiology.* Mosby, 1990.

[12] Y. Bourgault, Y. Coudière, and C. Pierre. Existence and uniqueness of the solution for the bidomain model used in cardiac electrophysiology. *Nonlinear analysis: Real world applications*, 10(1):458–482, 2009.

[13] H. Brown, D. DiFrancesco, and S. Noble. How does adrenaline accelerate the heart? 1979.

[14] A. Bucchi, M. Baruscotti, and D. DiFrancesco. Current-dependent block of rabbit sino-atrial node if channels by ivabradine. *The Journal of general physiology*, 120(1):1–13, 2002.

[15] A. Bucchi, M. Baruscotti, R. B. Robinson, and D. DiFrancesco. Modulation of rate by autonomic agonists in san cells involves changes in diastolic depolarization and the pacemaker current. *Journal of molecular and cellular cardiology*, 43(1):39–48, 2007.

[16] J. C. Clements, J. Nenonen, P. Li, and B. M. Horáček. Activation dynamics in anisotropic cardiac tissue via decoupling. *Annals of biomedical engineering*, 32(7):984–990, 2004.

[17] P. Colli Franzone, L. Guerri, M. Pennacchio, and B. Taccardi. Spread of excitation in 3-d models of the anisotropic cardiac tissue. ii. effects of fiber architecture and ventricular geometry. *Mathematical Biosciences*, 147(2):131–171, 1998.

[18] P. Colli Franzone, L. Pavarino, and B. Taccardi. Simulating patterns of excitation, repolarization and action potential duration with cardiac bidomain and monodomain models. *Mathematical biosciences*, 197(1):35–66, 2005.

[19] P. Colli Franzone, L. F. Pavarino, and S. Scacchi. Dynamical effects of myocardial ischemia in anisotropic cardiac models in three dimensions. *Mathematical Models and Methods in Applied Sciences*, 17(12):1965–2008, 2007.

[20] P. Colli Franzone, L. F. Pavarino, and S. Scacchi. Anode make and break excitation mechanisms and strength-interval curves: bidomain simulations in 3d rotational anisotropy. In *Functional Imaging and Modeling of the Heart*, pages 1–10. Springer, 2011.

[21] P. Colli Franzone, L. F. Pavarino, and S. Scacchi. Mathematical and numerical methods for reaction-diffusion models in electrocardiology. In *Modeling of Physiological Flows*, pages 107–141. Springer, 2012.

[22] P. Colli Franzone and G. Savaré. Degenerate evolution systems modeling the cardiac electric field at micro-and macroscopic level. In *Evolution equations, semigroups and functional analysis*, pages 49–78. Springer, 2002.

[23] J. A. Cottrell, T. J. Hughes, and Y. Bazilevs. *Isogeometric analysis: toward integration of CAD and FEA*. Wiley, 2009.

[24] H. J. Curtis and K. S. Cole. Transverse electric impedance of the squid giant axon. *The Journal of general physiology*, 21(6):757–765, 1938.

[25] C. De Falco, A. Reali, and R. Vázquez. Geopdes: A research tool for isogeometric analysis of pdes. *Advances in Engineering Software*, 42(12):1020–1034, 2011.

[26] S. Demir, J. Clark, C. Murphey, and W. Giles. A mathematical model of a rabbit sinoatrial node cell. *American Journal of Physiology-Cell Physiology*, 266(3):C832–C852, 1994.

[27] D. DiFrancesco. The role of the funny current in pacemaker activity. *Circulation research*, 106(3):434–446, 2010.

[28] D. DiFrancesco and D. Noble. Implications of the re-interpretation of ik2 for the modelling of the electrical activity of pacemaker tissues in the heart. In *Cardiac rate and rhythm*, pages 93–128. Springer, 1982.

[29] D. DiFrancesco and D. Noble. A model of cardiac electrical activity incorporating ionic pumps and concentration changes. *Philosophical Transactions of the Royal Society of London. B, Biological Sciences*, 307(1133):353–398, 1985.

[30] A. Fabiato. Calcium-induced release of calcium from the cardiac sarcoplasmic reticulum. *American Journal of Physiology-Cell Physiology*, 245(1):C1–C14, 1983.

[31] G. E. Farin. *Curves and surfaces for CAGD: a practical guide.* Morgan Kaufmann, 2002.

[32] B. Fermini and R. D. Nathan. Removal of sialic acid alters both t-and l-type calcium currents in cardiac myocytes. *American Journal of Physiology-Heart and Circulatory Physiology*, 260(3):H735–H743, 1991.

[33] N. Hagiwara, H. Irisawa, and M. Kameyama. Contribution of two types of calcium currents to the pacemaker potentials of rabbit sino-atrial node cells. *The Journal of Physiology*, 395(1):233–253, 1988.

[34] D. M. Harrild and C. S. Henriquez. A finite volume model of cardiac propagation. *Annals of biomedical engineering*, 25(2):315–334, 1997.

[35] B. Heath and D. Terrar. Separation of the components of the delayed rectifier potassium current using selective blockers of ikr and iks in guinea-pig isolated ventricular myocytes. *Experimental physiology*, 81(4):587–603, 1996.

[36] Y. Himeno, F. Toyoda, H. Satoh, A. Amano, C. Y. Cha, H. Matsuura, and A. Noma. Minor contribution of cytosolic ca2+ transients to the pacemaker rhythm in guinea pig sinoatrial node cells. *American Journal of Physiology-Heart and Circulatory Physiology*, 300(1):H251–H261, 2011.

[37] A. L. Hodgkin and A. F. Huxley. A quantitative description of membrane current and its application to conduction and excitation in nerve. *The Journal of physiology*, 117(4):500, 1952.

[38] B. Hopenfeld, J. G. Stinstra, and R. S. Macleod. Mechanism for st depression associated with contiguous subendocardial ischemia. *Journal of cardiovascular electrophysiology*, 15(10):1200–1206, 2004.

[39] T. J. Hughes, J. A. Cottrell, and Y. Bazilevs. Isogeometric analysis: Cad, finite elements, nurbs, exact geometry and mesh refinement. *Computer methods in applied mechanics and engineering*, 194(39):4135–4195, 2005.

[40] S. Kawano and M. Hiraoka. Transient outward currents and action potential alterations in rabbit ventricular myocytes. *Journal of molecular and cellular cardiology*, 23(6):681–693, 1991.

[41] J. P. Keener. An eikonal-curvature equation for action potential propagation in myocardium. *Journal of mathematical biology*, 29(7):629–651, 1991.

[42] J. P. Keener and J. Sneyd. *Mathematical physiology*, volume 8. Springer, 1998.

[43] Y. Kurata, I. Hisatome, S. Imanishi, and T. Shibamoto. Dynamical description of sinoatrial node pacemaking: improved mathematical model for primary pacemaker cell. *American Journal of Physiology-Heart and Circulatory Physiology*, 283(5):H2074–H2101, 2002.

[44] E. G. Lakatta. A paradigm shift for the hearts pacemaker. *Heart rhythm: the official journal of the Heart Rhythm Society*, 7(4):559, 2010.

[45] E. G. Lakatta, V. A. Maltsev, and T. M. Vinogradova. A coupled system of intracellular ca2+ clocks and surface membrane voltage clocks controls the timekeeping mechanism of the hearts pacemaker. *Circulation research*, 106(4):659–673, 2010.

[46] I. LeGrice, P. Hunter, and B. Smaill. Laminar structure of the heart: a mathematical model. *American Journal of Physiology-Heart and Circulatory Physiology*, 272(5):H2466–H2476, 1997.

[47] I. J. LeGrice, B. Smaill, L. Chai, S. Edgar, J. Gavin, and P. J. Hunter. Laminar structure of the heart: ventricular myocyte arrangement and connective tissue architecture in the dog. *American Journal of Physiology-Heart and Circulatory Physiology*, 269(2):H571–H582, 1995.

[48] M. Lei, P. J. Cooper, P. Camelliti, and P. Kohl. Role of the 293b-sensitive, slowly activating delayed rectifier potassium current, iks, in pacemaker activity of rabbit isolated sino-atrial node cells. *Cardiovascular research*, 53(1):68–79, 2002.

[49] C. M. Lloyd, J. R. Lawson, P. J. Hunter, and P. F. Nielsen. The cellml model repository. *Bioinformatics*, 24(18):2122–2123, 2008.

[50] C. Luo and Y. Rudy. A model of the ventricular cardiac action potential. depolarization, repolarization, and their interaction. *Circulation research*, 68(6):1501–1526, 1991.

[51] C. Luo and Y. Rudy. A dynamic model of the cardiac ventricular action potential. i. simulations of ionic currents and concentration changes. *Circulation research*, 74(6):1071–1096, 1994.

[52] V. A. Maltsev and E. G. Lakatta. Synergism of coupled subsarcolemmal ca2+ clocks and sarcolemmal voltage clocks confers robust and flexible pacemaker function in a novel pacemaker cell model. *American Journal of Physiology-Heart and Circulatory Physiology*, 296(3):H594, 2009.

[53] T. P. Mathew. *Domain decomposition methods for the numerical solution of partial differential equations*, volume 61. Springer, 2008.

[54] T. Nakayama, Y. Kurachi, A. Noma, and H. Irisawa. Action potential and membrane currents of single pacemaker cells of the rabbit heart. *Pflügers Archiv*, 402(3):248–257, 1984.

[55] P. Nielsen, I. Le Grice, B. Smaill, and P. Hunter. Mathematical model of geometry and fibrous structure of the heart. *American Journal of Physiology-Heart and Circulatory Physiology*, 260(4):H1365–H1378, 1991.

[56] B. Nilius. Possible functional significance of a novel type of cardiac ca channel. *Biomedica biochimica acta*, 45(8):K37–45, 1985.

[57] D. Noble, D. DiFrancesco, and J. Denyer. Ionic mechanisms in normal and abnormal cardiac pacemaker activity. *Neuronal and cellular oscillators*, pages 59–85, 1989.

[58] D. Noble and S. Noble. A model of sino-atrial node electrical activity based on a modification of the difrancesco–noble (1984) equations. *Proceedings of the Royal Society of London. Series B, Biological Sciences*, pages 295–304, 1984.

[59] K. Ono and H. Ito. Role of rapidly activating delayed rectifier k+ current in sinoatrial node pacemaker activity. *American Journal of Physiology-Heart and Circulatory Physiology*, 269(2):H453–H462, 1995.

[60] L. F. Pavarino and S. Scacchi. Multilevel additive Schwarz preconditioners for the bidomain reaction-diffusion system. *SIAM J. Sci. Comput.*, 31(1):420–445, 2008.

[61] L. F. Pavarino and S. Scacchi. Parallel multilevel Schwarz and block precon-ditioners for the Bidomain parabolic-parabolic and parabolic-elliptic formu-lations. *SIAM J. Sci. Comput.*, 33(4):1897–1919, 2011.

[62] M. Pennacchio, G. Savaré, and P. Colli Franzone. Multiscale modeling for the bioelectric activity of the heart. *SIAM Journal on Mathematical Analysis*, 37(4):1333–1370, 2005.

[63] M. Pennacchio and V. Simoncini. Algebraic multigrid preconditioners for the bidomain reaction–diffusion system. *Applied numerical mathematics*, 59(12):3033–3050, 2009.

[64] L. Piegl and W. Tiller. The nurbs book. 1997. *Monographs in Visual Com-munication*, 1997.

[65] J. M. Rogers and A. D. McCulloch. A collocation-galerkin finite element model of cardiac action potential propagation. *Biomedical Engineering, IEEE Transactions on*, 41(8):743–757, 1994.

[66] S. Rush and H. Larsen. A practical algorithm for solving dynamic membrane equations. *Biomedical Engineering, IEEE Transactions on*, (4):389–392, 1978.

[67] L. L. Schumaker. *Spline functions: basic theory*. Cambridge University Press, 1981.

[68] T. W. Sederberg, J. Zheng, A. Bakenov, and A. Nasri. T-splines and t-nurccs. In *ACM transactions on graphics (TOG)*, volume 22, pages 477–484. ACM, 2003.

[69] S. Severi, M. Fantini, L. A. Charawi, and D. DiFrancesco. An updated com-putational model of rabbit sinoatrial action potential to investigate the mech-anisms of heart rate modulation. *The Journal of Physiology*, 590(18):4483–4499, 2012.

[70] T. R. Shannon, F. Wang, J. Puglisi, C. Weber, and D. M. Bers. A mathe-matical treatment of integrated ca dynamics within the ventricular myocyte. *Biophysical journal*, 87(5):3351–3371, 2004.

[71] T. Shibasaki. Conductance and kinetics of delayed rectifier potassium chan-nels in nodal cells of the rabbit heart. *The Journal of Physiology*, 387(1):227–250, 1987.

[72] K. Skouibine, N. Trayanova, and P. Moore. Success and failure of the defibrillation shock. *Journal of Cardiovascular Electrophysiology*, 11(7):785–796, 2000.

[73] N. Smith, D. Nickerson, E. Crampin, and P. Hunter. Multiscale computational modelling of the heart. *Acta Numerica*, 13(1):371–431, 2004.

[74] M. D. Stern, L. Song, H. Cheng, J. S. Sham, H. T. Yang, K. R. Boheler, and E. Ríos. Local control models of cardiac excitation–contraction coupling a possible role for allosteric interactions between ryanodine receptors. *The Journal of general physiology*, 113(3):469–489, 1999.

[75] C. Stevens and P. Hunter. Sarcomere length changes in a 3d mathematical model of the pig ventricles. *Progress in biophysics and molecular biology*, 82(1):229–241, 2003.

[76] D. Streeter. Gross morphology and fiber geometry of the heart. *Handbook of physiology*, pages 61–112, 1979.

[77] D. Streeter and D. Bassett. An engineering analysis of myocardial fiber orientation in pig's left ventricle in systole. *The Anatomical Record*, 155(4):503–511, 1966.

[78] D. Streeter and W. Hanna. Engineering mechanics for successive states in canine left ventricular myocardium i. cavity and wall geometry. *Circulation Research*, 33(6):639–655, 1973.

[79] A. Toselli and O. Widlund. *Domain decomposition methods—algorithms and theory*, volume 34 of *Springer Series in Computational Mathematics*. Springer-Verlag, Berlin, 2005.

[80] A. Van Ginneken and W. Giles. Voltage clamp measurements of the hyperpolarization-activated inward current i (f) in single cells from rabbit sino-atrial node. *The Journal of physiology*, 434(1):57–83, 1991.

[81] M. Veneroni. Reaction–diffusion systems for the macroscopic bidomain model of the cardiac electric field. *Nonlinear Analysis: Real World Applications*, 10(2):849–868, 2009.

[82] T. M. Vinogradova, K. Y. Bogdanov, and E. G. Lakatta. β-adrenergic stimulation modulates ryanodine receptor ca2+ release during diastolic depolarization to accelerate pacemaker activity in rabbit sinoatrial nodal cells. *Circulation research*, 90(1):73–79, 2002.

[83] S. Zampini. *Non-overlapping domain decomposition methods for cardiac reaction diffusion models and applications*. PhD thesis, Università degli Studi di Milano, 2010.

[84] A. Zaza, R. Robinson, and D. DiFrancesco. Basal responses of the l-type ca2+ and hyperpolarization-activated currents to autonomic agonists in the rabbit sino-atrial node. *The Journal of physiology*, 491(Pt 2):347–355, 1996.

[85] H. Zhang, A. Holden, I. Kodama, H. Honjo, M. Lei, T. Varghese, and M. Boyett. Mathematical models of action potentials in the periphery and center of the rabbit sinoatrial node. *American Journal of Physiology-Heart and Circulatory Physiology*, 279(1):H397–H421, 2000.